Silicon Micromechanics for Applications in Fiber Optic Communication

Dissertation

submitted to the Faculty of Sciences of the University of Neuchâtel

to obtain the degree of Doctor of Science

by

Cornel Roman Marxer

ing. EPFL en microtechnique

Institute of Microtechnology
University of Neuchâtel
Rue Jaquet-Droz 1
2000 Neuchâtel
Switzerland

You may say to yourself, "My power and the strength
of my hands have produced this weelth for me."
But remember the Lord your God, for it is he
who gives you the ability to produce wealth.
Dt 8,17-18

Meinen Eltern und Grosseltern
in Dankbarkeit gewidmet

IMPRIMATUR POUR LA THÈSE

Silicon Micromechanics for Applicatione in Fibar Optic Communication

de M. Cornel Roman MARXER

UNIVERSITÉ DE NEUCHÂTEL

FACULTÉ DES SCIENCES

La Faculté des sciences de l'Université de Neuchâtel sur le rapport des membres du jury,

MM. N. de Rooij (directeur de thèse),
H.P. Herzig, P. Vettiger (IBM-Rüschlikon),
M. Ilegems (IMO-EPFL) et P. Vogel (Ascom, Berne)

autorise l'impression de la présente thèse.

Neuchâtel, le 30 juin 1997

Le doyen:

R. Dändliker

Summary

Micromachined silicon structures for applications in fiber optic communication are subject of the present thesis. The precision requirements of single mode fibers are well matched to the structure size of micromechanics and the related high precision photolithographical techniques.

A first family of devices studied in this thesis are developed for the alignment and attachment of fibers. Actually the possibility of a self aligned assembly of fibers is an essential condition for large scale production of photonic devices. Normal to the chip surface a wet anisotropic etched backside hole can align a fiber within +/- 5 µm with respect to topside structures. For the surface parallel alignment we have developed a new groove type based on reactive plasma etching instead of the conventional wet anisotropic etching. They allow for an alignment at the precision of the fiber. Processing variations are cancelled out by integrated clamping springs.

A second area of interest are reflective modulators for data communication. Based on silicon micromechanics various principles can be used to modulate the light coupling into a fiber: shutters, torsional mirrors and modulators based on interferenca. Because they promise the highest speed we focused our work on interference light modulators. A maximum modulation rate over 2 MBit/s, with an extinction ration of 10 dB could be achieved. Typical operation voltages are a +/- 5 V modulation signal superimposed on a 80 V bias.

Optical fiber switches are the third area of interest of the present thesis. We have invented and patented a micromechanical 2x2 optical switch. The development resulted in a switch with following characteristics: Typical losses with single mode fibers at a wavelength of 1.3 µm are below 1 dB (21 %) in the bar state and below 2.5 dB (45 %) in the cross state. The switching speed is 0.2 ms which is 50 times faster than a conventional mechanical switch.

In view of their long term operation we investigated into the reliability and long term stability of the reflective modulator and the fiber optic switch. It was found that an operation over millions of cycles doesn't lead to any noticeable change as long as the air humidity is low. A high air humidity in combination with a high electric field leads to corrosion fatigue and rupture of the mechanical suspensions.

Table of Contents

List of Notations

Symbol	Description	Unit
θ	incidence angle	[°]
δ	optical phase change	[°]
Δ	distance	[m]
ε	electrical permittivity	[C/Vm]
Γ	coupling loss	
η	admittance	[1/Ohm]
η_I	admittance of incident medium	[1/Ohm]
η_0	admittance of substrate	[1/Ohm]
λ	wavelength	[m]
μ	viscosity	[kg/ms]
ρ	density	[kg/m^3]
σ	stress	[Pa]
σ	surface roughness	[m]
d_i	thickness of layer i	[m]
d	diameter	[m]
E	Young modulus	[Pa]
f	frequency	[s^{-1}]
g	gap distance	[m]
g_0	initial air gap	[m]
h	height	[m]
I	area moment of inertia	[m^4]
k	spring constant	[N/m]
$k_{x,y,z}$	spring constant in x,y direction	[N/m]
k_{single}	spring constant of a single beam in a meander	[N/m]
l,L	length	[m]
M_j	optical characteristic matrix of layer j	
n_j	index of refraction of layer j	
Q	quality factor	
r_0	radial offset	[N/m]
$R_{1,2}$	reflectivity of mirror 1,2	
R	mechanical resistance	[N/ms]

S	surface area	[m^2]
t	thickness	[m]
T_c	critical temperature	[°C]
T	transmissivity	
V	voltage	[V]
V_p	pull-in voltage	[V]
V_{dryair}	release voltage in dry air	
$V_{humidair}$	release voltage in humid air	
w	mode field radius	[m]
w	width	[m]
x, y	displacement in x, y direction	[m]
z_0	longitudinal offset	[m]
Y	correction factor in brittle fracture theory	

Abbreviations

AFM	atomic force microscope
APL	ansys programming language
CSEM	Swiss Center for Electronics and Microtechnology Inc.
CVD	chemical vapor deposition
DMD	digital micromirror device
DRIE	deep reactive ion etching
FEM	finite element modelling
FTTH	fiber to the home
GLV	grating light valve
IC	integrated circuit
ICP	ion coupled plasma
IPA	isopropanol alcohol
LIGA	Lithographie, Galvanik, Abformung
MEMS	micro-electro-mechanical systems
MTTF	mean time to failure
SAM	self-assembled monolayer
SEM	scanning electron microscope
SOI	silicon-on-insulator
TM	transverse magnetic
TE	transverse electric
WDM	wavelength division multiplexing

Chapter One

Introduction

1.1. Micromachining

In the last decade research in micromachining technology experienced considerable growth. Many industrial countries have launched important research programs in this area[1]. Although the term "machining" is somewhat related to mechanical engineering, these programs include topics from many different engineering disciplines[2]: sensors for chemical and physical signals, pumps, motors, electronics, optical devices such as modulators and switches.

Such a large range of devices is united by a common fabrication technology. Instead of conventional machine turning or milling, the driving idea in micromachining is the use of photolithography and subsequent etching and deposition steps. A typical sequence is schematically shown in Figure 1.1. In this example two thin films of silicon dioxide and polysilicon were deposited on a silicon substrate. Their thickness is typically within the range of one micron. To structure these layers, a photosensitive resin is deposited. Using a mask, i.e. a glass plate with the desired pattern drawn on it, the areas where the polysilicon is to be removed are exposed to ultraviolet light. In the exposed areas the resin is dissolved in a developer. In a subsequent etching step the polysilicon is structured in an etching bath. The polysilicon is only removed in the areas that are not protected by the photoresist. As a particular feature these processing steps are not carried out on one device only

but on a whole wafer which can hold hundreds or even thousands of identical structures. Therefore this batch processing technology is of particular interest for high volume production. It has to be noted that the fabrication needs a considerable infrastructure, which cannot be afforded if only a small numbers of wafers are processed.

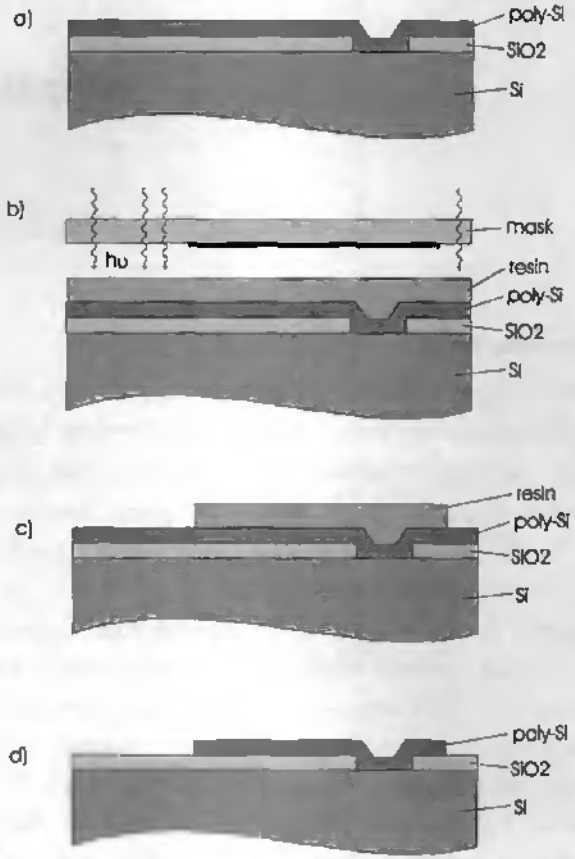

Figure 1.1: Schematic process of photolithography, which is the basic fabrication step in micromachining. a) silicon substrate with silicon dioxide and polysilicon thin film. b) Deposition of photosensitive resin and exposure. c) Development of resin. d) etching and stripping of resin.

This technology has determined the tremendous success of the integrated circuit industry and many believe that the same approach will lead to an enormous rise in the sensor, optics and actuator industry. In fact silicon based sensors for pressure and acceleration are already well introduced into the market. Because these sensors are produced in large quantities with relative ease they can now be found in high volume applications like consumer electronics for altimeters for example and automotive for airbags. But unlike the integrated circuit *(IC)* industry, where the same sequence of processing steps is applied to fabricate various electronic circuits, micromachining technology is application specific. For fluidic components other processing steps are applied than for accelerometers.

In addition to the processing technology adapted from the *IC* industry many new fabrication technologies are currently developed in micromachining. Bulk[3] and surface[4] micromachining are the two approaches best known. On the wafer level technologies like wafer bonding[5,6] thick film photolithography[7], electroplating[8], deep reactive ion etching[9] are applied to build more complex devices. In order to form microsystems, conventionally machined parts and micromachined devices are assembled into a common package often together with electronic circuits. Packaging can't be done on wafer scale anymore but individual chips and parts have to be joined. Most common integration technologies are gluing[10], soldering and flip-chip bonding[11]. The packaging technology is even more application dependent than micromachining. It has to establish not only an electrical connection to the "macroworld", but depending on the application also a fluidic, a mechanical, an optical or chemicalone. A low cost sensor/actuator chip can become a high cost sensor/actuator system in an appropriate package. Together with the calibration and the testing the packaging is often the most expensive part of the fabrication. All these technologies from micromachining to the final packaging are generally designed with MEMS technologies, which stands for Micro-Electro-Mechanical-Systems.

1.2. Optical Micro-Electro-Mechanical-Systems (Optical MEMS)

In the past years the MEMS field has developed into different application specific specialities. One of these topics are optical MEMS[12]. Unlike other actuators such as motors and pumps, optical devices are well suited for miniaturisation. First no power

output is needed for modulation or redirection of light. Therefore the performance, i.e. for example the speed, of an optical component increases with miniaturisation, whereas the output torque of a motor decreases[13]. A further advantage is that the beam diameter, especially of guided optics, matches well with the scale of micromechanics. And finally the connection to the outside word doesn't disturb the actuator function. I.e. a light beam doesn't alter the mechanical behaviour of a system.

In the past 20 years a large research effort has been directed towards the micromachining technology and the more and more also for optical applications. Very early, already at the end of the 60'ies, micromechanical light modulators[14],[15] were fabricated using the silicon micromachining technology. Since then a wide range of micro-opto-mechanical components fabricated by micromachining have been developed.

In silicon light generation is not yet practical. Therefora only passive devices can be fabricated by silicon micromachining. These devices can modify optical signals by mechanical movements. A wide variety of such passive optical devices based on conventional mechanics exits: active filters, spectrometers, modulators, switches, scanners, choppers, shutters and dynamic focusing mirrors. For most of these microfabricated demonstrators were presented in literature. Below we will give a short overview of this previous work on optical MEMS.

One particular family of devices uses the Fabry-Perot principle to build wavelength filters for spectroscopic[16] or *WDM* (wavelength division multiplexing) applications[17]. Because of their planar structure Fabry-Perot cavities are well suited for microfabrication. Fabry-Perot filters were also integrated on lasers and photodiodes to build wavelength tuneable lasers[18],[19] and wavelength tuneable photodiodes[20],[21]. To tune rib emitting laser diodes the mirror can't be integrated in a planar technology, because it has to be surface normal. *Uenishi* et al. used an external vertical micromirror which can be moved laterally[22],[23]. Here the Fabry-Perot cavity is formed between the laser end face and the external mirror, which was fabricated by electroplating into a thick photoresist mold.

Another family of devices comprises light modulators for intensity modulation or spatial modulation of light. Using various fabrication techniques, torsion mirrors[24],[25],[26] and shutters[24] were demonstrated for incoherent light, whereas the

Fabry-Perot principle[27],[28] and mechanical active diffractive gratings[29] were proposed for coherent light modulation.

Micromachining allows to fabricate a large amount of modulators in parallel. This is exploited to build matrixes of modulators for display applications[30],[31]. A schematic view of the most advanced micromirror development is shown in Figure 1.2.

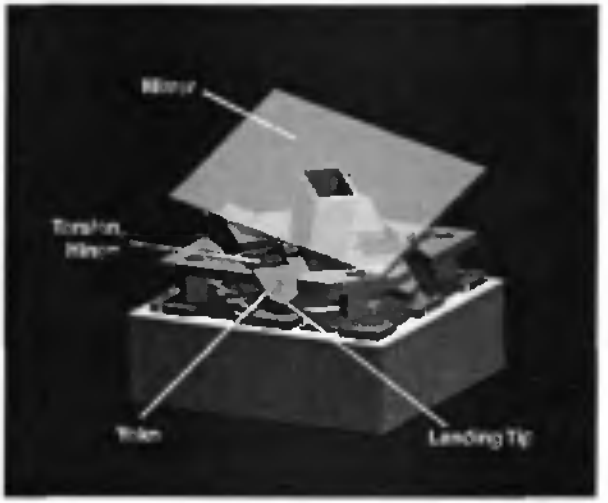

Figure 1.2: The Digital-MicromIrror-Display (DMD) from Texas Instruments is based on a torsional aluminium mirror.

Scanners are another application of micromachined torsion mirrors. There are two basic types of scanners: either galvanometric[32] with a steady state deflection or resonant[33] with dynamic scanning. Potential applications of micromechanical scanners were proposed in laser printers, in bar code readers[34] or in fiber optic switches[35].

For spectroscopic applications a tuneable infrared filter was fabricated using the LIGA technique[36],[37]. The filter is based on a mechanically deformable grating structure. *Kwa* et al. have integrated a fixed grating with a photodiode array to build a spectrometer for the visible wavelength range[38].

Silicon micromachining has also been successfully applied to fabricate adaptive optical components. *Vodin* et al. have fabricated a flexible, focusing mirror[39]. The focal length of the mirror can be adapted with electrostatic actuation. Similar devices were proposed in Reference[40],[41].

Above devices demonstrated the possibilities of the *MEMS* approach, but only a few devices were developed further towards commercialisation. A major concern when facing a potential commercialisation is the insufficient performance of the device and the impossibility to sell in numbers high enough to make the MEMS fabrication process affordable. Prototyping and small scale production still is very expensive in the *MEMS* field. For the high volume market of projection display only recently two companies have announced prototype projection displays based on micromechanical spatial light modulators[42,43].

Using *MEMS* technology the U.S. company Texas Instruments has build *DMD* (Digital-Micromirror-Device) for displaying video images. The heart of the *DMD* is a chip which has on its surface thousands of square, movable aluminium mirrors only a fraction of hair-width in size. The electronic circuit in the chip allows each mirror to be tilted individually permiting or impeding the reflection of light onto a larger screen. Figure 1.2 shows a schematic drawing of an individual mirror which can be actuated by electrostatic forces. Figure 1.3 shows a cross-section in the *SEM* (Scanning-Electron-Microscope) of the 16 µm wide aluminium mirror. The torsion hinges are on the lower side of the mirror[44].

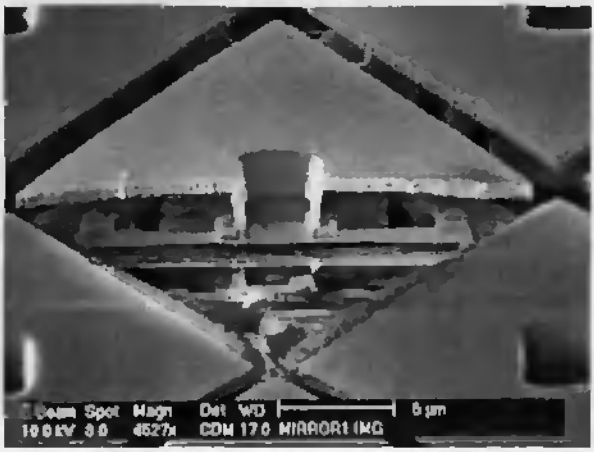

Figure 1.3: SEM cross-section of TI's micromirror and its suspension.

Silicon Light Machines in Sunnyvale, California is the second company developing a projection display based on a *MEMS* chip. Just as TI's *DMD* micromirror their system is also based on reflective *MEMS*, which they call the *GLV* (grating light

valve). Instead of redirecting light by a torsion mirror it uses diffraction to either reflect or diffract light[45]. To create a *GLV* device tiny picture elements, or pixels, are formed on the surface of a silicon chip. Each of these pixels is made up of multiple ribbon-like structures, which can be moved up or down over a very small distance (only a fraction of the wavelength of light) by controlling electrostatic forces. The ribbons are arranged in such a way that each pixel is capable of either reflecting or diffracting light. When appropriately addressed by control signals an array of pixels may thus form a pattern of light and dark points on the surface of the chip. An image is created by collecting the reflected or diffracted light with an appropriate lens system, either to be projected onto a front- or rear-screen system, or to be viewed directly by the eye. The *GLV* device is reflective, and therefore it can be highly efficient in its use of light.

1.3. Outline of the Thesis

The purpose of the present thesis is to explore *MEMS* devices for fiber optic communication applications. Our work focused on micromachined actuators for two distinct applications: The first is a reflective modulator for low cost communication links and the second is a fiber optic 2x2 switch for network reconfiguration and security by-passing of defect network nodes.

When I started work on the thesis in spring 1994 a considerable experience with micromechanical light modulators has already been gained at the IMT. Using the well established polysilicon surface micromachining technique[46] micro shutters, pivoting micromirrors and interference light modulators[47] were developed in the IMT laboratory. It was natural to continue in this field and orient the work already accomplished towards more specific applications with a commercial interest. In order to do this an industry partner with clear development goals is essential. I received this input from Ascom Tech AG, Bern, which also supported financially large parts of the project.

To exploit the advantage of the micromachining technology part of the packaging should already be included in the microfabricated chip. Especially in view of a commercial application, it is essential to have alignment structures for the fibers already integrated on the chip to suppress cumbersome optical alignment. In *chapter 2* some concepts and requirements are discussed for a passive alignment of

fibers with the help of micromachined structures. These concepts will find application in the reflective modulator and fiber optic switch.

Chapter 3 reports in a detailed manner on the design aspects of the reflective modulator, its fabrication by polysilicon surface micromachining and its characterisation.

Chapter 4 deals with the development of a 2x2 switch for single mode fibers. The switch is inspired by the surface micromachining approach but its fabrication is based on the new possibilities of deep reactive ion etching. *Chapter 4* reports on several aspects of the switch development: its design, fabrication and characterisation.

In view of the commercialisation of micromechanical components the long term stability and reliability issue has to be addressed. There is still little work available in literature on the long term behaviour of micromachined actuators; this is natural as there are practically no micromachined actuators on the market. To partly fill this gap *chapter 5* is dedicated to the reliability analysis of the reflective modulator and the fiber optic switch.

In the *chapter 6* conclusions are drawn and possible further developments are discussed.

[1] "Winzlinge für den Weltmarkt", *Vision das Schweizer Magazin für Wissenschaft und Innovation*, 5/96, pp. 18 - 20

[2] "A New Lilliputian World of Micromachines", *Time*, December 2, 1996, pp. 64 - 66

[3] H. Seidel, "The Mechanism of Anisotropic, Electro-Chemical Silicon Etching in Alkaline Solutions", *in Tech. Dig. IEEE Solid State Sensor and Actuator Workshop*, Hilton Head Island, SC, USA, June 1990, pp. 86 - 91

[4] C. Linder, L. Paratte, M. A. Gretillat, V. P. Jaecklin and N. F. de Rooij, "Surface Micromachining", *J. Micromech. Microeng.*, vol.2 (1992), pp. 122-132

[5] C. Harendt, B. Hoffinger, H. Graf, E. Penteker, "Silicon Direct Bonding For Sensor Applications: Characterisation Of The Bond Quality", *Sensors and Actuators A*, vol. A25-27 (1991), pp. 87-92

[6] W. H. Ko, J. T. Suminto, G. J. Yeh, "Bonding Techniques for Microsensors", in *Micromachining and Micropackaging of Transducers*, edited by C D Fung, P W Cheung, W H Ko and D G Flemming, Elsevier Science Publisher, 1985, pp. 41 - 62

[7] M. Despont, H. Lorenz, N. Fahrni, J. Brugger, P. Renaud, P. Vettiger, "High Aspect Ratio, Ultrathick, Negative-tone Near-UV Photoresist for MEMS Applications", *Proceedings of the 10th IEEE international workshop on Micro Electro Mechanical Systems*, Nagoya, Japan 26 - 30, 1997, pp. 518-522

[8] J. Gobet, F. Cardot, J. Bergqvist and F. Rudolf, "Electrodeposition of 3D Microstructures on Silicon", *J. Micromech. Microeng.* 3 (1993), pp. 123-130

[9] C. Marxer, M. A. Gretillat, N. F. de Rooij, R. Baettig, O. Anthamatten, B. Valk, P. Vogel, "Vertical Mirrors Fabricated by Reactive Ion Etching for Fiber Optical Switching Applications", *Proceedings of the 10th IEEE international workshop on Micro Electro Mechanical Systems*, Nagoya, Japan 26 - 30, 1997, pp. 49-54

[10] D. R. Owen, R. M. Zone, "Epoxy Encapsulants, Adhesives and Speciality Polymers for Microelectronic Applications", in *Micromachining and Micropackaging of Transducers*, edited by C D Fung, P W Cheung, W H Ko and D G Flemming, Elsevier Science Publisher, 1985, pp. 19 - 26

[11] J. H. Lau, *Flip Chip Technologies*, McGraw Hill, (1995)

[12] See the proceedings of LEOS Summer topic meeting on "Optical MEMS and their Applications", *Digest of IEEE/LEOS 1996 Summer Topical Meeting*, Keystone Co, USA, August 1996,

[13] Paratte L., *Integrated and Hybrid Electrostatic Rotary Micromotors Based on Silicon Technology*, Doctoral Thesis, University of Neuchatel, 1996, Chapter 2

[14] Preston K Jr. "An Array Optical Spatial Phase Modulator", in *Proceedings of the IEEE International Solid State Circuits Conference (Institute of Electrical and Electronics Engineers, New York, 1968)*, p. 100.

[15] J. A. van Raalte "A New Schlieren Light Valve for Television Projection", *Appl. Opt.*, vol. 9 (1970), pp. 2225 - 2230

[16] J. H. Jerman, D. J. Clift, R. S. Mallison, "A Miniature Fabry Perot Interferometer with a Corrugated Diaphragm Support", *Tech. Digest IEEE Solid-State Sennsor and Actuator Workshop*, Hilton Head Island, SC, June 4-7 (1990), pp. 140-144

[17] J. H. Jerman, D. J. Clift, "Miniature Fabry-Perot Interferometer Micromachined in Silicon for Use in Optical Fiber WDM Systems", *IEEE*, 1991, pp. 372-375

[18] M. C. Larson, J. S. Harris, "Broadly-Tunable Resoant Cavity Light Emitting Diode", *IEEE Photo. Tech. Lett.* 7 (11), pp. 1267-1269 (1995)

[19] A. T. T. D. Tran, Y. H. Lo, Z. H. Zhu, O. Haronian, E. Mozdy, *IEEE Photon. Technol. Lett.*, vol. 8, pp. 393-395, 1996.

[20] A. Aratani, P. J. French, P. M. Sarro, D. Poenar, R. F. Wolffenbuttel, S. Middelhoek, "Process and Design Considerations for Surface Micromachined Beams for a Tuneable Interferometer Array in Silicon", *Sensors and Actuators A*, A 43, 17-23 (1994)

[21] M. S. Wu, E. C. Vail, G. S. Li, W. Yuen, C. J. Chang-Hasnain, "Widely and Continuously Tunable Micromachined Resonant Cavity Delector with Wavelength tracking", *IEEE Photon Tech. Lalt.* 8 (1), pp. 98-100 (1996)

[22] Y. Uenishi, K. Honma, S. Hagoka, "Tunable Laser Diode Using a Nickel Micromachined External Mirror", *Electron. Lett.*, 32 (13), pp. 1207 - 1208 (1996)

[23] Y. Uenishi, M. Tsugal, M. Mehregany, "Hybrid-Integrated Laser-Diode Micro-External Mirror Fabricated by (110) Silicon Micromachining", *Electron. Lett.* 31 (12), pp. 965-966 (1995).

[24] V. P. Jaecklin, C. Linder, N. F. de Rooij, J. M. Moret, R. Vuilleumier, "Optical Microshutters and Torsional Micromirrors for Light Modulator Arrays", *Proc. IEEE Micro Electro Mechanical Systems (MEMS '93)*, Fort Lauderdale, Florida, Feb. 7-10 (1993), pp. 124 - 127

[25] L. J. Hornbeck, "Deformable Mirror Spatial Light Modulator", *Spatial light modulators and Application III, Spie Critical Raview*, vol. 1150, August 1989, pp. 86 - 102

[26] S. W. Chung, J. W. Shin, Y. K. Kim and B. S. Han, "Design and Fabrication of Micromirror Supported by Electroplated Nickel Posts", *Tech. Dig. 8th International Conference on Solid-State Sensors and Actuators (Transducers '95)*, Stockholm, Sweden, june 1995, vol. 1 pp. 308 - 311

[27] J. A. Walker, K. W. Goosen, and S. C. Arney, "Fabrication Of A Mechanical Anti-Reflection Switch For Fiber To The Home System", *IEEE J. Microelectromech. Syst*, Vol. 5, no. 1, pp. 45-51, 1996

[28] C. Marxer, M.A. Gretillat, V.P. Jaecklin, R. Baettig, O. Anthamatten, P. Vogel and N. F. de Rooij, "Megahertz Opto-Mechanical Modulator", *Sensors and Actuators A 52* (1996) pp. 46-50

[29] O. Solgaard, F. S Sandejas, D M Bloom, "Deformable Grating Optical Modulator", *Optics Letters 17*,(1992), no. 9, pp. 688-690

[30] J. M. Younse, "Projection Display Systems Based on the Digital Micromirror Device (DMD"), *Spie Conference on Microelectronic Structures and Micromechanical Devices for Optical Processing and Multimedia Applications*, Austin, Texas (October 24, 1995), Spie Proceedings, Vol. 2641, pp. 64 - 75

[31] V. P. Jaecklin, C. Linder, N. F. de Rooij, J. M. Moret, R. Vuilleumier, "Line-Addressable Torsional Micromirrors For Light Modulator Arrays", *Sensors and Actuators*, A 41-42, pp 324-329 (1994)

[32] R. A. Miller, G. W. Burr, Y. C. Tai, D. Psaltis, C. M. Ho, R. R. Katti, "Electromagnetic MEMS Scanning Mirrors for Holographic Data Sorage", *Solid State Sensor and Actuator Workshop*, Hilton Head Island, South Carolina, June 2-6 (1996), 163-166.

[33] M. Ikeda et al., "Two Dimensional Silicon Micromachined Optical Scanner Integrated With Photodetector And Piezoresistor", *Tech. Dig. 8th International Conference on Solid-State Sensors and Actuators (Transducers '95)*, Stockholm, Sweden, june 1995, vol. 1 pp. 293 - 296

[34] M.-H. Kiang, O. Solgaard, R. S. Muller, and K. Y. Lau, "Micromachined Polysilicon Microscanners For Barcode Readers", *IEEE Photon. Technol. Lett.*, Vol. 8, no. 12, 1996

[35] H. Gnewuch, R. Ulrich, "Fiber-Optic 1x6 Switch With Smooth Transmission Spectrum", *Sensors and Actuators A*, A 45, (1994), pp. 109 - 114

[36] C. Müller and J. Mohr, "A Microspectroemter Fabricated By The LIGA Process", *Proc. Transducers '93, (Yokahama, 1993)*

[37] T. R. Dhnstein, J. D. Zook, J. A. Cox, B. D. Speldrich, T. L. Wagener, H. Guckel, T. R. Christenson, J. Klein, T. Earles and I. Glasgow, "Tunable IR Filters Using Flexible Microstructures", *IEEE Micro Electro Mechanical Systems (MEMS '95)*, Amsterdam, NL, 1995

[38] T A Kwa, *Integrated Silicon Spectrometer Fabricated Using Bulk Micromachning Techniques*, PhD Thesis, Delft University, Delft University Press, 1995

[39] G. Vodin and P. M. Sarro, "Flexible Mirror Micromachined In Silicon", *Applied Optics*, 34, (1995), pp. 2968 - 2972

[40] L. M Miller, M.L Argonin, R.K. Bartman, W.J. Kaiser, T.W. Kenny, R.L. Norton, E.C. Vote, "Fabrication And Characterisation Of A Micromachined Deformable Mirror For Adaptive Optics Applications", *Proc. SPIE 1945*, (1993), pp. 421-430

[41] M. Hisanaga, T. Koumura, T. Nattori, "Fabrication Of 3-Dimensionally Shaped Si Diaphragm Dynamic Focusing Mirror", *Proc. IEEE workshop on Micro Electro Mechanical Systems*, p. 30, (1993)

[42] http://www.ti.com/dlp

[43] http://www.siliconlight.com

[44] L. J. Hornbeck, "Digital Light Processing and MEMS: Timely Convergence For A Bright Future", *SPIE Micromachining and Microfabrication '95*, Austin, Texas October 24, (1995).

[45] O. Solgaard, F. S Sandejas, D. M. Bloom, "Deformable Grating Optical Modulator", *Optics Letters* 17 (9), pp. 688-690

[46] C. Linder, *Electromechanical Polysilicon Structures and Micromachining Processes for Sensor and Actuator Applications*, Doctoral Thesis, University of Neuchatel, 1993

[47] V. P. Jaecklin, *Surface Micromachined Electrostatic Actuators*, Doctoral Thesis, University of Neuchatel, 1994.

Chapter Two

Passive Alignment of Fibers

2.1. Introduction

Packaging has become a key issue in evaluating the manufacturability and reliability of fiber optical devices. A significant part of the packaging problem is due to the stringent alignment tolerancas required for coupling between photonic devices and optical fibers. Nevertheless every practical device should meet this alignment tolerances by passive alignment of the fiber. Active alignment is too time and money consuming for production. Silicon micromachined fiber alignment grooves have traditionally facilitated the attachment of fibers to photonic devices[1,2]. By preferential crystallographic wet etching[3] very precise V-shaped grooves can be formed in <100> silicon to be used as alignment means. The accuracy of fibre alignment depends on the constancy of the groove dimensions (0.2 μm to 1 μm) and of the fiber geometry i.e. its diameter and core concentricity. With V-grooves reproducible alignment within a micrometer can be achieved.

To date, most applications have required the alignment of only one single mode fiber. However with the advent of integrated optical devices and parallel receiver/transmitter systems the need to align linear arrays of fibers has arisen. Chips with V-groove arrays were utilised to connect ribbons of up to 12 fibers with excess losses approaching the theoretical minimum[4]. The method of positioning fibers in silicon-V-grooves can also be used for aligning of fiber arrays to LEDs[5], for

photodiode arrays[6], laser arrays and for coupling of fibers to integrated optical waveguide devices[7]. In these devices the polished fiber array, which forms a separate chip, has to be actively aligned with the waveguides by recording the coupling loss. In this popular "butt coupling" technique[8] the fiber array is fixed by epoxy, UV-curing adhesive or by laser welding. However this alignment (3 to 6 degrees of freedom within +/- 10 µm for multimode and +/- 1 µm for singlemode fibers) is time consuming and cumbersome. A lot of research is going on to replace the active alignment of the silicon chip by passive means. Completely passive alignment is for example based on the mechanical positioning of the fibers in V-grooves on the one hand and on photolithgraphically defined mechanical reference structures on the device on the other hand. The V-groove chip is then passively aligned on the device chip by the integrated mechanical reference. Another method uses the self-aligning property of soldering in flip-chip bonding for a self-aligned hybrid assembly of chips[9]. Such systems are referred as silicon optical benches on a chip or as silicon optical motherboards[10],[11],[12]. In these devices the silicon chip is used as a base plate for the photonic devices and fibers assembled on it.

2.2. Coupling Light between Single Mode Fibers

To illustrate the stringent alignment tolerances in single mode optical devices, the coupling efficiency between two single mode fibers versus radial, angular and longitudinal misalignment will be calculated below. This configuration is current in fiber optic components: In a reflective modulator light from the input fiber has to be coupled back into the same fiber. Whereas for a fiber optic switch light from an input fiber has to be coupled into either one of two output fibers. Both configurations can be discribed using the same coupling theory. Actually if the use of refocalizing components or of fibers with lensed ends is avoided the coupling effeciency only depends on the separation between the fiber cores and the quality of the fiber end surface. It can be shown, that the fundamental modal field of single mode fibers is Gaussian to a good approximation[13]. Coupling loss calculations can therefore be reduced to evaluating the coupling between misaligned Gaussian beams. A general equation has been derived to calculate the coupling loss between identical single mode fibers with longitudinal, transverse and angular misalignment[14]. This equation

is particularly useful since it depends only on the mode field radius w of the fibers. The coupling loss Γ in dB is:

$$\Gamma = -10\log\left\{\frac{16n_{co}^2 n_o^2}{(n_{co}+n_o)^4}\frac{1}{q}\exp\left(-\frac{p\cdot u}{q}\right)\right\} \qquad (2.1)$$

where

$$p = (k_g w)^2/2$$

$$q = G^2$$

$$u = F^2 + 2FG(\sin\theta_t) + \left(G^2 + \frac{1}{2}\right)\sin^2\theta_t$$

$$F = r_0/k_g w^2$$

$$G = z_0/k_g w^2$$

$$k_g = 2\pi n_o/\lambda$$

n_{co} and n_o are the index of refraction values of the fiber core and the gap between the fiber ends, respectively. w is the mode field radius (radius at which the near field power falls to $1/e^2$ of its maximum value) of the transmitting and receiving fibers, respectively. λ is the wavelength of light used, and r_0, z_0 and θ_t are the transverse, longitudinal, and angular (tilt) misalignment, respectively, as shown in Figure 2.1.

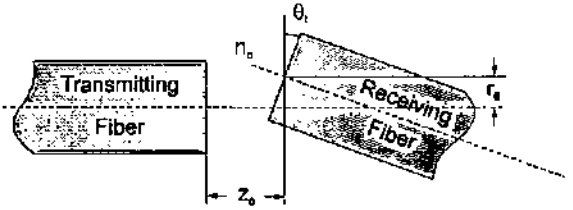

Figure 2.1: Diagram to define transverse offset r_0, longitudinal offset z_0 and angular misalignment θ_t, for a single mode fiber splice.

The first term of equation (1.1) expresses the loss due to the Fresnel reflection at the interface of the fiber core and the gap between the fiber ends. This reflection gives rise to a backreflection into the transmitting fiber. This backreflection can vary with wavelength and temperature due to interference effects. This unwanted reflection can be eliminated with an Anti-Reflective coating, or by filling the gap with

an index matching oil, or finally with fiber ends polished at an angle, so that the reflected light is not guided in the core anymore but transmitted into the cladding.

The second half of the equation (2.1) expresses the loss due to beam broadening and to the angular and transverse misalignment. Typical single mode fibers at 1.3 μm have mode field radii w between 2.5 and 5.1 μm depending on the index step parameters and core diameters[15].

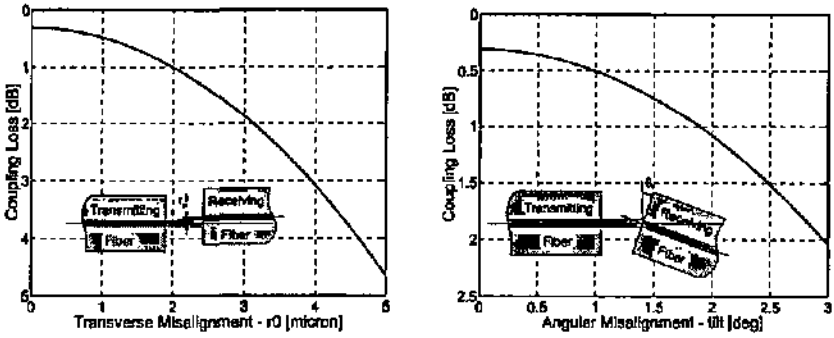

Figure 2.2: coupling loss between two misaligned fibers in air. a) lateral offset, b) angle offset.

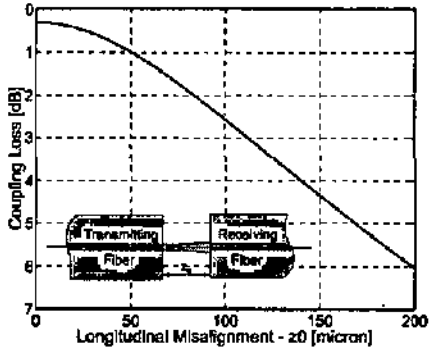

Figure 2.3: coupling loss between two fibers separated by air.

Figures 2.2 and 2.3 give numerical simulations of the coupling loss between typical single mode fibers for a wavelength at 1.3 μm. At zero offset the loss is already 0.3 dB (7%), which corresponds to the Fresnel reflections at the fiber-air interface. It can be seen that a transversal misalignment r_0 delermines a very sharp increase of

the coupling loss. A radial alignment error of 3 μm leads already to a loss of 2 dB (37%). The second graphic of Figure 2.2 shows the coupling loss as a function of the angle error. As for the transverse offset the angular error θ should be kept low; a tilt of 3 degrees already results in a loss of 2 dB (37 %). Only the longitudinal offset is less sensitive. Here at a separation of 50 μm the coupling loss is still as low as 1 dB (20 %).

2.3. *Surface Normal Passive Alignment*

The simplest way for aligning a fiber normal to the wafer surface is to use a backside hole defined by preferential crystallographic wet etching as shown in Figure 2.4 a). The 54.7° sidewalls of the square hole allow to centre the fiber. The alignment tolerance of the photolithography between the bottom and front surface of a wafer is ± 5 μm. Compared to this the concentricity error of the fiber core, which is ± 0.5 μm, is small. This method is not precise enough to align waveguides or lasers, but the precision is adequate for devices with relaxed positioning tolerances such as micromechanics or photodiodes. Although a simple KOH hole can align a fiber with a precision sufficient for many applications, the fiber has to be attached onto an additional holder to keep it in position under bending moments. Thus the attachment and a coarse positioning for the fibers has to be done in the package structure of the component and only the fine alignment of the fiber can be done by the KOH hole.

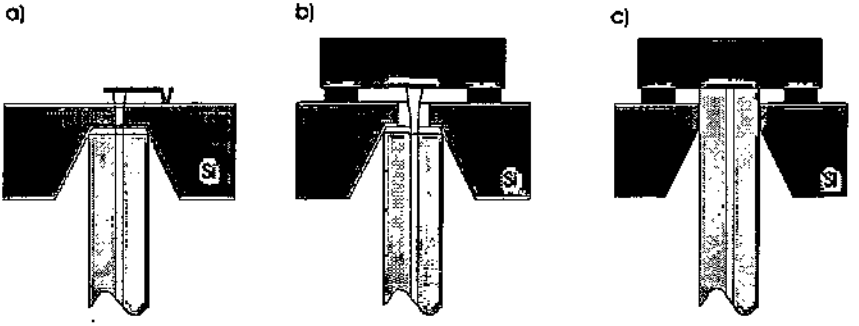

Figure 2.4: Surface normal alignment of fibers. a) alignment with KOH hole and AR coating for light transmission. b) alignment with KOH hole and through hole for light transmission. c) alignment with deep reactive ion etched circular hole.

In order to suppress the backreflection at the fiber-silicon interface the silicon substrate has to be anti-reflective coated. If the working wavelength is shorter than 1100 nm the light is absorbed in the bulk silicon and the hole has to be etched through the wafer. One possibility to completely open the hole is to continue the wet anisotropic etching until the topside insulation layers are reached. It has been demonstrated by *Y. Kim et al.* that such membranes are still strong enough to hold micromechanical structures such as a Fabry-Perot Cavity[16]. It no micromechanical structures have to interfere with the light beam the trough hole can also be opened from the top side by reactive ion etching as shown in Figure 2.4 b).

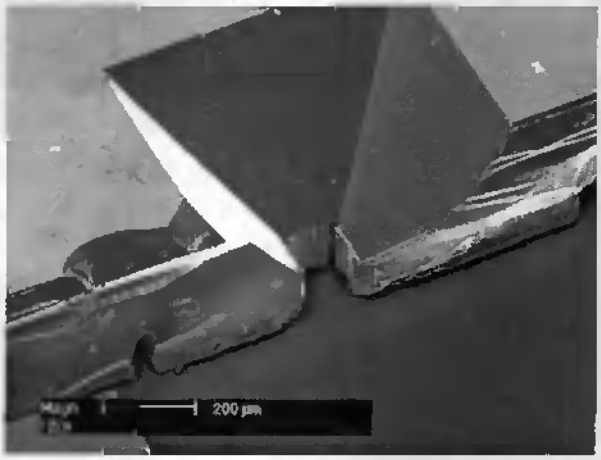

Figure 2.5: Hole for surface normal alignment and attachment of single mode fiber.

Such a reactive Ion etched hole can also be used as a passive alignment for fibers as shown in Figure 2.4 c) and Figure 2.5. If the hole is sufficiently deep it is sufficient not only to align the fiber but to keep the position under bending moments, which allows to additionally simplify the packaging. The alignment hole is plasma etched from the top side and can be aligned within ± 2 µm with the other topside structures such as contact lines, solder bumps etc. These allow for a hybrid integration of III-V components such as photodiodes or vertical cavity surface emitting lasers (VCSELs) by using flip-chip bonding techniques. An overall precision better than ± 3 µm should

be possible. Figure 2.5 shows a practical realisation of such a through hole, which is combined with a wet etched entrance for an easy insertion of the fiber.

2.4. Surface Parallel Passive Alignment

Integrated waveguides devices and edge emitting lasers need a surface parallel alignment of the fiber. This is usually achieved by wet crystallographic etched V-grooves. Figure 2.6 a) shows a cross section of a fiber in a V-groove and defines the parameters which are necessary to describe the positioning of the fiber in the truncated v groove.

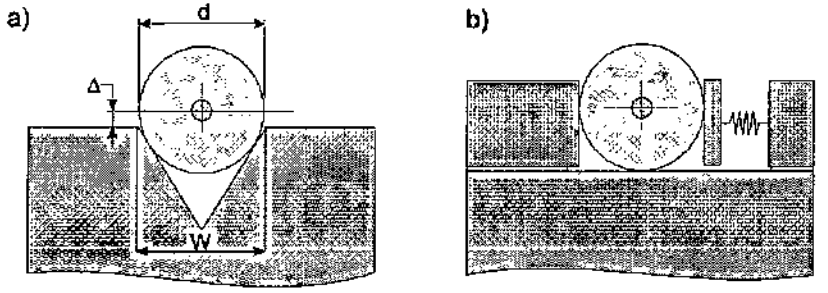

Figure 2.6: Surface parallel alignment of fibers in grooves. a) in a v-groove. b) in a rectanguar groove with clamping spring.

The fiber has a diameter d. The groove parameters are W, the width of the groove at the top surface and θ the crystallographically defined angle (54.7°). The fiber is placed in the groove in such a way that it contacts the side walls at two points. We find, that the fiber position is given by

$$w + \sqrt{2}\Delta = \sqrt{\frac{3}{2}}d \qquad (2.2)$$

where Δ is the distance from the silicon surface to the centre of the fiber core. Thus if the fiber diameter is known and if the depth of the waveguide mode below the crystal reference surface is known, then equation (2.2) can be used to calculate the required groove width W. For example to completely dig the fiber in the v-groove, i.e. for Δ = 62.5 µm, a width W = 241.5 µm necessary. On the other hand if the centre of the fiber should be at the substrate surface, i.e. for Δ = 0 µm, a width W = 153 µm is necessary.

Above equation can also be used to predict the alignment tolerance of several important parameters. A potential source of misalignment lies in the control of the fiber diameter. From (2.2) we have:

$$\frac{\partial \Delta}{\partial d} = \sqrt{\frac{3}{4}} \qquad (2.3)$$

So for d = 125 µm and a 1 percent diameter change we have a change of Δ = 1.1 µm and a corresponding excess loss of 0.3 dB. Another potential source of error is silicon groove width variation. Again from (2.2) we have:

$$\frac{\partial \Delta}{\partial W} = -\frac{1}{\sqrt{2}} \qquad (2.4)$$

If the etching mask is well aligned with the <110> crystal directions, the groove widths can be controlled down to ± 1 µm. Thus we expect to see offsets < 0.7 µm with corresponding excess losses of 0.1 dB. To align the etching mask within 0.1° with respect to the crystal directions, an alignment to the wafer flat is not sufficient, because the flat is only specified within +/- 1°. Therefore a first etching with special measurement patterns has to be done to determine the <110> crystal directions[17].

Figure 2.7: plasma etched rectangular groove for surface parallel fiber alignment

A second way to align fibers parallel to the chip surface is to use rectangular grooves as schematically shown in Figure 2.6 b). Such grooves may be fabricated by deep reactive ion etching of silicon, or other LIGA (Lithographie Galvanik Abformung) like technologies. The fibers are clamped to a vertical reference plan by spring structures and the alignment errors are basically reduced to the eccentricity of the fiber cores and of fiber diameter variations. For standard fibers the concentricity is within 1 µm and a fiber diameter is controlled within +/-1 µm. If all errors accumulate a radial offset of 3 µm is possible which would result in a loss of 1 - 2 dB. Figure 2.7 shows an example of such a groove realized on Silicon-on-Insulator wafers (SOI).

2.5. *Conclusions*

In view of large scale production of photonic devices a passive alignment of the fiber is essential. Only with a passive alignment the assembling time can be kept short, which besides cost and reliability is an important factor for a high volume production. To illustrate the stringent alignment tolerances we have calculated the coupling efficiency versus radial, transverse and angular misalignment between two typical single mode fibers. Radial and angular offset have to be very well controlled. A radial alignment error of 2 µm or a an angular error of 2° result in a loss of already 1 dB (20 %). On the other hand the longitudinal offset is not so critical, here the loss stays below 1 dB for an offset as high as 50 µm.

We have discussed micromachined silicon structures that allow a passive alignment of the fibers. For a surface normal positioning the sidewalls of a wet anisotropic etched backside hole can already act as a fiber alignment within ± 5 µm relative to the top surface structures. The major source of alignment error is the double side photolithography alignment.

For surface parallel alignment the most widespread approach is to use wet anisotropic etched V-grooves. For a precise groove width control it is necessary to align the groove with the <110> crystal orientations with a better precision than just the wafer flat. A second more compact alignment structure is based on plasma etched rectangular grooves. Integrated springs allow to clamp the fiber to a reference plan and to suppress the influence of the groove dimension on the alignment precision.

[1] B. Hillerich,"Micromechanics to Components for Optical Communication", In *Micro-System Technologies '90*, Editor H. Reichel, Berlin: Springer Verlag, pp. 458-464, (1990)

[2] E. J. Murphy and T. C. Rice, "Self-Alignment Technique for Fiber Attachment to Guided Wave Devices", *IEEE Journal of Quantum Electronics*, Vol. QE-22, no. 6, pp 928-932, June 1986

[3] D. B. Lee, *J. Appl. Phys.*, 40, pp. 4569-4574, (1969)

[4] C. M. Schroeder, *Bell Syst. Techn. J.* 57, p. 91-97 (1976)

[5] P.P. Deimel et al. *Tech. Digest OFC' 85*. (San Diego, Ca), TUC4 (1985)

[6] M. G. Brown et al., *Tech. Digest Int. Electron. Dev. Meet.* (San Francisco, Ca), p. 727 (1984)

[7] E.J. Murphy and T. C. Rice, *J. Lightwave Technol.* LT-1, pp.479-482 (1982)

[8] W. Van Etten and J. Van der Plaats, *Fundamentals of Optical Fiber Communication*, Hemel Hempstead: Prentice Hall, (1991)

[9] C. H. Bulmer, S. K. Sheem, R. P. Moeller, and W. K. Burns, " High Efficency Flip Chip Coupling Between Single Mode Fibers And $LinbO_3$ Channel Waveguides," *Appl. Phys. Lett.*, vol. 37, pp. 351-353, (1980)

[10] G. De Pestel, W. Delbare, K. Allaert, A. Ambrosy, Q. Tan, J. Verbeke and M. Vrana, "Multifiber Electro-Optical Modules Compatible With The Fiber In Board Technology", *Proc. IEEE Lasers and Electro-Optics Society* (LEOS '94), pp. 224-225, 1994

[11] B. Hillerich and A. Geyer, *Electon. Lett.* 24, pp. 918 - 919 (1988)

[12] J. W. Parker, P. M. Harrison, P. J. Ayliffe, T. V. Clapp, M. C. Gear and R. G. Peal, "8 x 700 Mbit/s Array Transmitter/Receiver Pair Realised In Opto-Hybrid Silicon Motherboard Technology", *Microelecron. Eng. 19*, pp. 215-218, (1992)

[13] D. Marcuse, *Bell Syst Tech. J. 56*: 703, (1977)

[14] S. Nemoto, and T. Makimoto. *Opt. And Quan. Elect. 11*: 447 (1979)

[15] C. M. Miller, C Mettler, A White, *Optical Fiber Splices and Connectors, Theory and Methods*, New York: Marcel Dekker Inc., 1986, Chapter 4.

[16] Y. Kim, D. P. Neikirk, "Micromachined Fabry-Perot Cavity Pressure Transducer", *IEEE Photonics Technology Letters*, Vol. 7, No. 12, December 1995, pp.1471-1473

[17] M. Vangbo and Y. Bäcklund, "Precise Mask Alignment To The Crystallographic Orientation Of Silicon Wafers Using Wet Anisotropic Etching", *J. Micromech. Microeng.* 8 (1998), pp. 279-284

Chapter Three

Reflective Modulator

3.1. Introduction

3.1.1. Reflective Modulation

It is generally expected, that the fibre optics, which already form the backbone of most telecommunication networks, will extend throughout the network to the subscriber location or even to the individual household. Crucial for a rapid and large scale expansion of such a fiber-to-the-home (FTTH) network is the price of the optical line termination[1,28]. An alternative to the active transceiver comprising a light emitting device such as a laser diode or a LED is the reflecting duplexer, where part of the incoming light is used to send back information. In a network architecture using a reflective modulator the number of components can be reduced to a minimum: a single fiber and only one laser are needed to achieve bi-directional data transmission between two locations. To send data from the service provider to the subscriber location, the laser diode is directly modulated and a photo-detector at the subscriber location receives the intensity modulated signal. To send data from the subscriber location to the service provider the incident light is modulated by the reflective modulator and returned into the fiber, schematically shown in Figure 3.1. At moderate bit rates reflective modulation devices consume considerably less electrical power than active light sources such as diodes or LEDs. Hence a reflective

transceiver on the customer premises leads to a reduced power consumption and lowers the costs for emergency power supplies, which also results in an increased reliability.

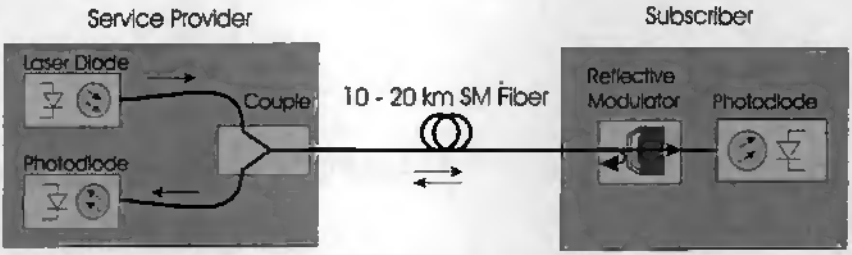

Figure 3.1: Point-to-point communication using reflective modulation.

A further advantage of using reflective modulation is the inherent maintenance of wavelength coherence of modulators. In a wavelength division multiplexed (WDM) network configuration every subscriber end is delivered with a distinct wavelength. If information has to be sent back from the subscriber location through the same fiber this information has to be carried by the same wavelength as the incident one. This wavelength coherence is readily obtained when a reflective modulator is used, whereas it is difficult to achieve if a light source has to be locked on the incident wavelength.

Several research groups have actively studied and demonstrated fiber-optic communication links based on reflective modulation[2,3,4]. During these investigations, it became clear that existing device technologies, based on waveguide technologies on $LiNbO_3$[5] or III-V substrates[6] for reflective modulators suffer from two drawbacks. First, in comparison with active light sources, commercially available components are not competitively priced at the present time. This is mainly due to high processing and packaging costs. Furthermore many devices suffer from polarisation-dependent operating characteristics and comparatively high optical losses, factors which have a negative impact on the possible link length. The existing device types for reflective modulators are based on electro-optic phenomena. In principle these effects provide extremely high modulation bandwidths up to tens of Gbit/s[7].

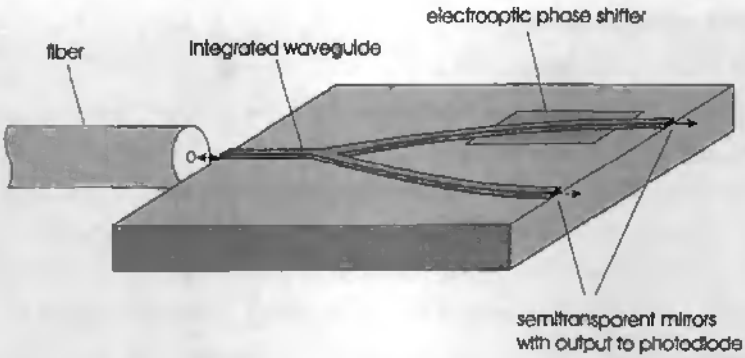

Figure 3.2: A reflective intensity modulator based on integrated waveguides on a lithium niobate or a III-V substrate using a Mach-Zehnder interferometer[8].

However, in most practical cases high capacity is only necessary in the 'downstream' direction from the service provider to the subscriber, whereas only limited bandwidth needs to be transmitted in the opposite upstream direction. Modulation rates up to several Mbit/s can be achieved with micro-mechanical modulators. Based on silicon micromachanics[9] such modulators have the potential of low fabrication costs and can be produced in large quantities.

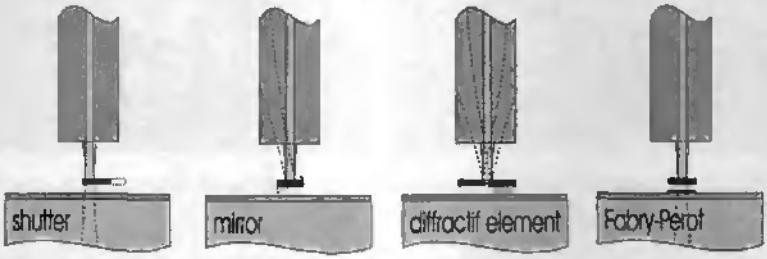

Figure 3.3: Reflective modulation using micromechanical principles.

3.1.2. Micromechanical Light Modulators

Research on micromechanical light modulators goes back to the late 1960-ies[10,11]. These early micromachined modulators were of the phase shifting or scanning mirror type. Since then a wide range of micro-opto-mechanical components fabricated by micromachining have been developed[12,13,14]. Many of these could be

used as reflective modulators for single mode fibers as schematically shown in Figure 3.3.

One possibility to modulate light mechanically is to use a shutter. In the microshutter configuration a mirror can be moved in and out of the optical path. If the shutter is out of the optical path the light beam is transmitted through the anti-reflection coated silicon wafer. In the on-state the shutter is placed in the optical path and the light beam is reflected back into the fiber. Realisations of such shutters are demonstrated in Ref.[15], and an example realized by Jaecklin et al.[16] is shown in Figure 3.4. The maximum operation frequency of such devices is quite low, only up to 30 kHz are reported. This reduced speed is a trade off between the actuation voltage and the maximum shutter displacement amplitude, which must be over 10 µm for a single mode fiber application.

a) b)

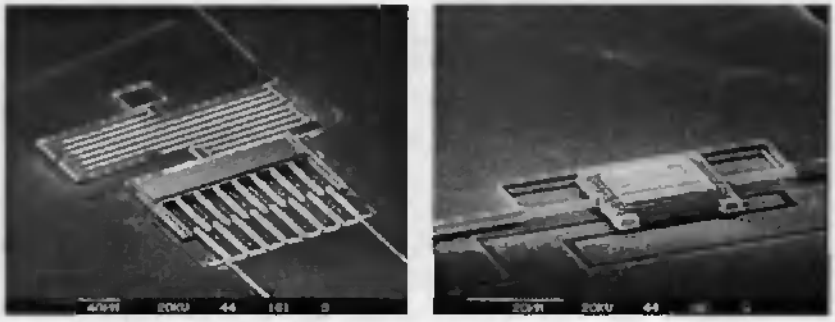

Figure 3.4: Micromechanical light modulators: a) A comb driven micro-shutter. b) A torsional micromirror[15].

In a torsional micromirror the necessary motion to modulate light is much smaller due to the fact that the light coupling into a single mode fiber drops drastically if the incident light beam forms an angle with the fiber core direction. A rotation amplitude of ± 1.5 can result already in a modulation amplitude of 10 dB (see Figure 2.2 in Chapter 2). For torsional micromirrors maximum operation speeds over 500 kHz are reported[15,17]. Although their speed is limited, an important characteristic of the shutter and mirror modulators is their wavelength insensitivity. The last two designs of Figure 3.3 are based on interference effects and are thus inherently wavelength sensitive.

In the third design a micromechanical diffractive element with a changeable phase step is used to redirect light[18,20]. A displacement of only λ/4 is necessary for modulation. An inconvenient of this approach is the tight positioning tolerance for the fiber, i.e. the fiber must be aligned above the small gap between the mirrors.
Finally the last configuration is based on a microfabricated Fabry-Perot modulator consisting of two semitransparent mirrors, arranged one over the other seperated by an air gap. Displacement of one of the two mirrors changes the interference properties, which results in a light modulation. Important advantages of this solution compared with the three other micromechanical principles is the high speed over 1 MHz. In addition the design offers a relaxed fiber positioning tolerance, the ease of integration in a planar surface micromachining technology and the possibility to collect part of the light on the other side of the wafer for the down stream data detection. Because this approach promises the highest speed we didn't investigate further the above alternative solutions but concentrated our work on the Fabry-Perot device. The response of a Fabry-Perot is inherently sensitive to the operation wavelength, therefore the design has to be optimised for the operation wavelength range. In our case we have focused on the first telecom window at wavelengths around 1.31 μm.

3.1.3. Fabry-Perot Modulator

The operation principle of the Fabry-Perot modulator, shown in a schematic view in Figure 3.5, is as follows: One of the mirrors is fixed whereas the other one can be displaced. Part of the incident light is reflected from the first mirror. The remainder of the optical wave reaches the second mirror, where a second reflection occurs. Part of this wave will reach the incident light and will build constructive or destructive interference. The sum of these and all subsequent reflections depends on the distance separating the two mirrors.
For two mirrors with an identical reflectivity it turns out that the reflected waves exactly neutralise one another if the airgap is an integer multiple of half the optical wavelength. Whenever this condition is fulfilled the mirror arrangement becomes fully transparent. Thus a small movement of the mirror can modulate the device reflection between nearly 0 % and 90 %.

These kind of modulators are actuated by electrostatic forces. Several different mirror materials have been described. For the movable mirror there have been used: a silicon nitride membrane[19,20,21] a silicon nitride - polysilicon multilayer [22] and a silicon-on-insulator (SOI) - silicon nitride bilayer[23]. The fixed mirror is formed by the silicon substrate[19,20,23] or by a thin polysilicon[22] layer on an anti-reflection coated wafer.

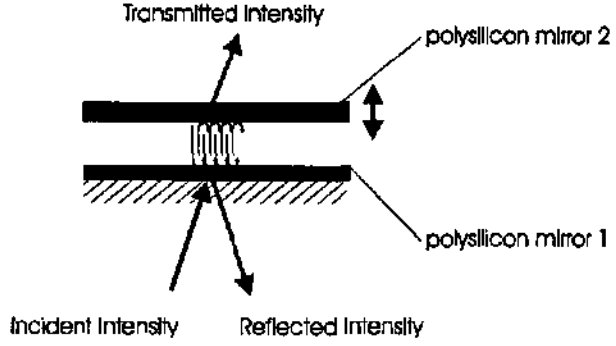

Figure 3.5: Fabry-Perot cavity consisting of mirrors having high reflectance and low absorption.

In order to use the well established polysilicon surface micromachining technique we have worked with a design where both mirrors of the Fabry-Perot cavity consist of polysilicon layers[24,25] having a reflectivity of about 70 % each. For operating wavelengths above 1.1 µm polysilicon is transparent. Due to the high refractive index of polysilicon our Fabry-Perot modulator has the potential of achieving higher finesse and reflectivity compared to the silicon nitride devices.

Figure 3.6 shows the configuration of a micromechanical reflective modulator. On the topside of the chip a first polysilicon thin film serves as the fixed mirror. Fabricated by surface micromachining the second free standing polysilicon layer can be deformed by electrostatic forces and acts as the second mirror of the Fabry-Perot. The deformation results in a change of the optical path between the mirrors which leads to a reflectivity modulation.

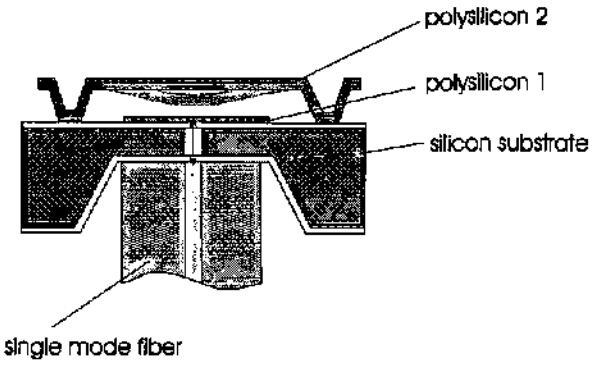

Figure 3.6: Cross section of the Fabry-Perot modulator, where the fixed mirror is formed by the polysilicon 1 layer and the movable mirror by the polysilicon 2 layer. The single mode fiber is placed into an etched hole for simplified packaging and reduced insertion loss.

A single mode fiber is placed into an etched hole in the chip backside. This hole is necessary to reduce the distance between the fiber end and the modulator thus limiting the loss of light. The beam divergence is further reduced due to the high refractive index of silicon. In addition illuminating the mirror from the backside has the advantage of a simplified packaging. The fiber end is simply placed into the backside hole, the sidewalls of this can act as a passive alignment. A draw back of the back-illumination is that the hole surface has to be anit-reflection coated, because the reflection at the fiber-silicon interface can act as an parasitic Fabry-Perot cavity with the topside modulator.

In the next paragraphs of this chapter we will report on the modelling, fabrication and characterisation of a reflective modulator based on the Fabry-Perot principle. The potential application of such a device lies in communications. The specifications are defined in consequence: The operational wavelength range should be from λ=1275 nm to λ=1350 nm, thus in the first telecom window. The development will focus on two distinct devices, one with the highest possible speed and one with a low operation voltage.

3.2. Numerical Modelling of Electrostatic Fabry Perot Modulator

In this paragraph the used approach for the design of the reflective modulator is presented. First the basic theory of thin film optical filters will be resumed. Applying the theory will allow to refine our optical design and to predict the effects of layer thickness mismatch and the effect of a change in the operation wavelength.

The mechanical modelling is subdivided into a static and a dynamic part. First the electromechanical behaviour of the electrostatic driven membrane is simulated. Than the limitation of the maximum modulation rate by the resonant frequency of the mechanical membrane and the air damping is discussed.

Finally the effect of process variation and the different operating wavelengths on the modulator response are discussed. Design goals that should be met are a maximum modulation rate above 3 Mbit/s and an On-Off contrast above 10 dB over a wavelength window between 1275 nm and 1350 nm. The air damping of the resonator should be close to critical in order to suppress the overshot ringing.

3.2.1. Optical Modelling

3.2.1.1. Optical Theory of Interference Coating

A multilayer nonabsorptive thin-film coating, as our micromechanical Fabry-Perot, can be represented as a multilayer dielectric system. Each layer is characterised by its index of refraction n_j and its thickness d_j. Standard optical theory allows to solve the total reflection of such a system using a matrix method[26]. Each layer j can be expressed by a matrix M_j. For our modulator light incidence is normal to the layer surface. In this case the matrix becomes independent from the light polarisation, which means that the modulator will inherently show no polarisation sensitivity.

$$M_j = \begin{bmatrix} \cos\delta_j & -\frac{i}{\eta_j}\sin\delta_j \\ -i\eta_j \sin\delta_j & \cos\delta_j \end{bmatrix} \qquad (3.1)$$

where δ_j is the optical phase change

$$\delta_j = \frac{2\pi}{\lambda} n_j d_j \qquad (3.2)$$

where λ is the wavelength in air, n_j and d_j are the refractive index and the thickness of the coating material. η_j is the optical admittance of a layer, which is the refractive index of the layer devised by 377 Ω, the impedance of vacuum.

$$\eta_j = \frac{n_j}{377} \qquad [\Omega^{-1}] \qquad (3.3)$$

If the angle of incidence of the light is not normal to the surface the optical admittance η_j becomes angle and polarisation dependent, i.e. the optical admittance and thus the reflectivity and transmission become angle and polarisation dependent:

for s-polarisation (Transverse Electric):

$$\eta_j = 377 n_j \cos\vartheta_j$$

for p-polarisation (Transverse Magnetic):

$$\eta_j = \frac{377 n_j}{\cos\vartheta_j}$$

An important property of the matrix M_j is that its determinant always equals 1, also in presence of absorption.

The matrix

$$M = M_1 \cdot M_2 \cdot M_3 \cdots M_m \qquad (3.4)$$

incorporates the optical properties of all the layers. Noting η_{m+1} the admittance of the substrate, then the equivalent optical admittance of the layer system can be calculated by

$$\eta = \frac{C}{B} \qquad (3.5)$$

where B and C are given by above matrix and the admittance of the substrate:

$$\begin{bmatrix} B \\ C \end{bmatrix} = M \begin{bmatrix} 1 \\ \eta_{m+1} \end{bmatrix} \qquad (3.6)$$

The reflectivity R can be expressed in a similar form as the well known Fresnel formula:

$$R = \left| \frac{\eta_0 - \eta}{\eta_0 + \eta} \right|^2 \qquad (3.7)$$

This formula is the basis for all subsequent optical simulations.

3.2.1.2. Fabry Perot Interferometer

As already shown in the introduction to micromechanical light modulators our Fabry-Perot cavity consists of two polysilicon mirrors. At the working wavelength of $\lambda = 1.3$ µm polysilicon is transparent, thus there is no light loss due to absorption. The reflectivity R_1 and R_2 of the thin film mirrors is maximum if their thickness is an odd multiple of a quarter wavelength, $\lambda/(4n)$, where λ is the working wavelength and n the refractive index of polysilicon. At 1.3 µm the refractive index of single crystal silicon is 3.5[27]. For quarter wavelength films the reflectivity R_1 and R_2 of the mirrors can be expressed according to equation (3.5) and (3.7) by

$$R_{1,2} = \left(\frac{n^2 - n_0 n_i}{n^2 + n_0 n_i} \right)^2 \qquad (3.8)$$

Where n_0 is the refraction index of the underlying medium and n_i the refraction index of the incident medium. For the free standing polysilicon membrane the underlying medium is air and $n_0 = n_i = 1$. Thus equation (3.8) yields a reflectivity of 72 % for R_2. In order to get the same reflectivity for R_1, the refractive index of the substrate has to be matched by an anti-reflection coating. Thus it is possible to get an equivalent refraction index n_0 close to 1.

In the practical realisation the first mirror has a nominal thickness of $3\lambda/4n$ = 280 nm and the second one a thickness of $5\lambda/4n$ = 468 nm allowing for an optimum reflectivity at the working wavelength of 1310 nm.

Table 3.1: Thicknesa of polyailicon mirrors with optimum reflectivity at a wavelength of 1300 nm

polysilicon 1	$3\lambda/4n$ = 280 nm
polysilicon 2	$5\lambda/4n$ = 468 nm

The transmission T of a lossless Fabry-Perot modulator is a function of the reflectivity R_1 and R_2 of its mirrors and of the air gap h between the mirrors:

$$T = \frac{(1-R_1)(1-R_2)}{(1-\sqrt{R_1R_2})^2 + 4\sqrt{R_1R_2}\sin^2 2\pi\frac{h}{\lambda}} \qquad (3.9)$$

This expression has maxima and minima when the sine in the denominator is respectively zero and one. Thus for h being a multiple of $\lambda/4$, the transmission becomes:

$$T_{max} = \frac{(1-R_1)(1-R_2)}{(1-\sqrt{R_1R_2})^2} \quad \text{for } h = 0, \lambda/2, \lambda \ldots \qquad (3.10)$$

$$T_{min} = \frac{(1-R_1)(1-R_2)}{(1+\sqrt{R_1R_2})^2} \quad \text{for } h = \lambda/4, 3\lambda/4 \ldots \qquad (3.11)$$

The reflectivity of the Fabry-Perot can become zero, only if the mirrors are of equal reflectivity. In this case equation (3.10) is always 1. Thus, to get a maximal contrast and a maximum reflectivity of the Fabry-Perot, the reflectivity R_1 and R_2 of the two mirrors must be as equal as possible and as high as possible.

Using the above interference filter theory it is possible to simulate the response of the modulator as a function of the airgap separating the mirrors as shown in Figure 3.7. The reflectivity attains its minimum at every airgap thickness which is an integer multiple of half the optical wavelength.

Thus at mirror separations of 650 nm, 1300 nm and 1950 nm the Fabry-Perot is in optical resonance and the reflectivity has a sharp minimum. The air gap distance at minimum reflectivity depends sensitively on the working wavelength. The Fabry-Perot is in its maximum reflectivity state over a broader air gap and also wavelength

range. In order to be able to adjust easily the working point, i.e. the minimum in reflectivity, the membrane should stay in a high reflecting state in its rest position.

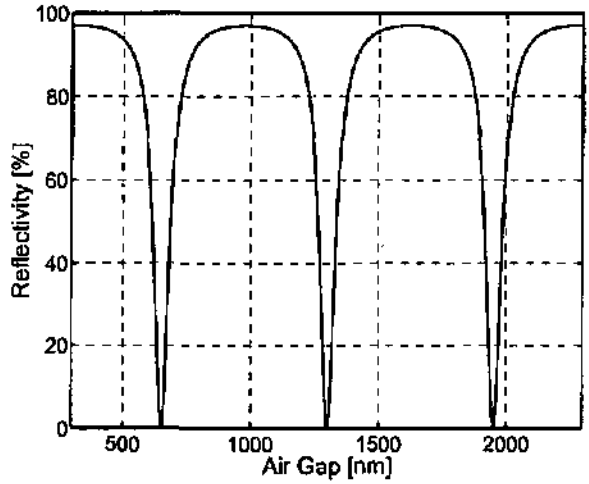

Figure 3.7: Simulated reflectivity as a function of the distance separating the two mirrors for ideal layer thickness at a wavelength λ=1.3 μm.

Both the variable wavelength and the imprecision in the mirror thickness affect the Fabry-Perot performance. On the one hand the On-Off ratio may be reduced, on the other hand the air-gap height for minimum reflectivity may shift by more than the wavelength, i.e the membrane actuation must allow to adjust the air-gap height over a wider range than just the wavelength range. The effect of wavelength change and layer thickness variation on the On-Off ratio is maximum when the difference in the reflectivities of the two mirrors is highest. An assumed imprecision of 5 % in the layer thickness reduces the On-Off ratio from over 20 to 11 dB at worst, as shown in Figure 3.8. The maximum On-Off ratio reduction at 1275 nm results from errors in the layer thickness, where the first mirror exceeds by 5 % the nominal thickness, whereas the thickness of deformable mirror remains 5 % below the nominal thickness (Figure 3.8 a)). At a working wavelength of 1350 nm the highest reduction of the On-Off ratio results when the first mirror is 5 % too thin and the moveable

mirror is 5 % too thick (Figure 3.8 b)). The shift of the air-gap height of minimum reflectance is small; the gap height at optical resonance is close to the wavelength.

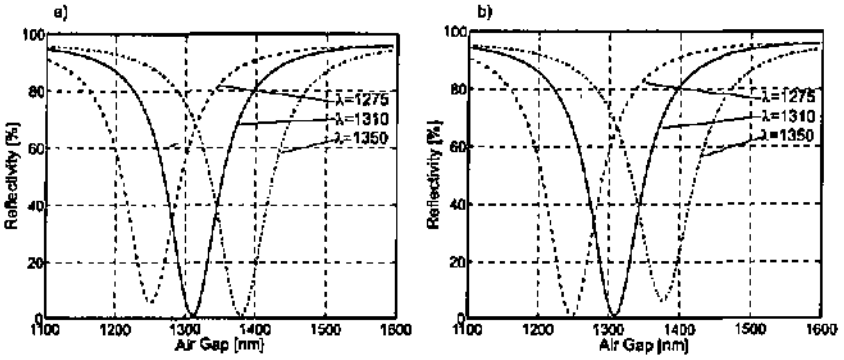

Figure 3.8: Effect of a 5 % error in layer thickness on On-Off ratio: a) 5 % too thick poly-1 and 5 % too thin poly-2 mirrors b) 5 % too thin poly-1 and 5 % too thick poly-2 mirrors. In the worst cases the On-Off ratio is reduced to 10 dB.

The effect of wavelength modification and layer thickness variation on the shift of the air gap at optical resonance is maximum if the error in the layer thickness goes in the opposite direction to the change in wavelength. At a plus 5% error in layer thickness (Figure 3.9 a)) and at a working wavelength of 1275 nm the minimum reflection condition is reached at an airgap of only 1.2 μm. The difference between the air gap height and the working wavelength is as high as 75 nm. All the same the modulator maintains an On-Off ratio above 20 dB. At a minus 5% error in layer thickness (Figure 3.9 b)) and at a working wavelength of 1350 nm the air gap height at minimum reflection moves up to 1.42 μm. Figure 3.9 shows that an unfortunate combination of processing imprecisions can considerably scatter the air-gap height at optical resonance.

Generally a low actuation voltage is desired. Therefore the smallest possible airgap is best. One would preferably choose the working point at the optical resonance with the smallest airgap, i.e. at 650 nm as shown in Figure 3.7. As will be described in detail in the paragraph on mechanical modelling, parallel plate electrostatic actuators only allow for a stable deformation of 30% - 40% of the initial air gap height, then a collapse occurs. As it appears in Figure 3.9 a deformation of 400 nm

can be necessary to cover the wavelength range. This is not possible when the initial air-gap is 950 nm because after 30 % - 40 %, i.e after 290 nm - 380 nm of deformation, the instability of the electrostatic actuator is reached. Therefore the smallest possible undeformed air gap height is 1.55 - 1.6 µm.

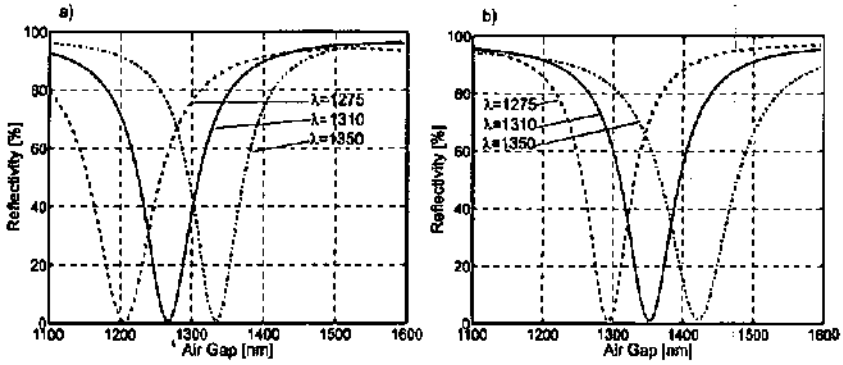

Figure 3.9: Effect of a 5 % error in layer thickness on air-gap height at optical resonance: a) 5 % too thick mirrors shift optical resonance 70 nm down. b) 5% too thin mirrors shift optical resonance 75 nm up.

In the simulations of Figure 3.7 to Figure 3.9 the mirror surfaces are supposed to be parallel and flat. In the actual design the moveable mirror is a deformable membrane which is no longer flat in the actuated position, but deformed. For a membrane deformation of 300 nm this curvature introduces an airgap difference of about 10 nm between the center and the border of the light spot. If the light distribution is supposed to be uniform, which is worse than the actual gaussian beam, than an additional On-Off contrast reduction of 1-2 dB is introduced.

Whereas the air gap height at minimum reflectivity has to be adjusted to the working wavelength within the range of a few nm, the influence of the air gap height is less critical in the high reflecting state. As shown in the reflectivity spectrum of Figure 3.10 the modulator has a high reflectivity for wavelength between 1200 and 1350 nm for an airgap of 1.55 µm. At an air-gap height of 1.3 µm the reflectivity is drastically reduced for a wavelength around 1.3 µm. The spectral width of the wavelength range with more than 50 % transmission is here 45 nm only.

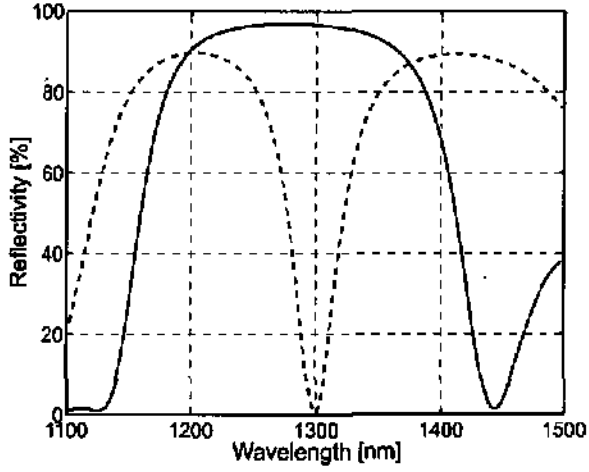

Figure 3.10: Simulated reflection spectrum at an air gap of 1.55 μm (plain line) and 1.3 μm (dashed line).

3.2.1.3. anti-reflective coating

As shown in the cross-section of Figure 3.6 the silicon substrate is anti-reflective coated on both sides. On the upper side this coating should match the index of the substrate to that of air so that the fixed polysilicon mirror can have the same reflectance as the second polysilicon mirror according to equation (3.8). On the bottom side the AR-coating should reduce the reflection between the fiber and the silicon substrate to a minimum.

If a single layer can be used for the Anti-Reflective coating, it should have a thickness d_f of a quarter wavelength[26]:

$$d_f = \frac{\lambda}{4n_f} \qquad (3.12)$$

The refraction index n_f of the film should have a value[28] of

$$n_f = \sqrt{n_0 n_s} \qquad (3.13)$$

where n_i is the index of the incident medium and n_0 is the index of the silicon substrate, which is 3.50[27] at 1.3 μm. For a coating towards air the ideal index is

n_f = 1.87, for a coating towards a fiber the index of the quarter wavelength film should be n_f = 2.26.

In polysilicon surface micromachining the substrate is usually passivated by a silicon dioxide - silicon nitride bilayer. Silicon dioxide has a refraction index of 1.46. The refraction index of silicon nitride is process dependent and can vary between 1.9 and 2.1. In our laboratory the stochiometric silicon nitride has a refraction index of 2.0. The refractive indexes of these films were measured in our laboratory by an ellipsometer at 633 nm.

With a bilayer AR-coating consisting of a thermal oxide and a nitride it is possible to get a perfect coating towards air, because the index of the ideal single layer coating, i.e. 1.87, lies between 1.49 and 2.0, the refraction indexes of silicon dioxide and silicon nitride. With a bilayer coating it is possible to match the underlying silicon substrate to any refraction index, which lies in between the index of the two layers. The corresponding layer thickness would be 60 nm for the oxide and 96 nm for the nitride. The thickness of these layers are numerically calculated using equations (3.4) - (3.6).

Another pair of values of layer thickness, which results in a minimum reflection, consists of a quarter wavelength thick nitride layer on a half wavelength thick oxide layer. A half wavelength thickness results in a so called absence layer, i.e. at the working wavelength the oxide layer doesn't influence the reflectivity. A quarter wavelength nitride layer ($d_{nitride}$ = 162 nm, $n_{nitride}$ = 2.0) has an anti-reflective effect. The resulting admittance is n = 1.14. The reflectivity towards air is still below 0.5 % with the advantage, that the reflectivity towards glass is below 2 %. The first coating design with a zero reflection towards air would lead to a 4 % reflection towards glass.

Table 3.2: Possible AR-coatings with oxide-nitride bilayer

	Oxide	*Nitride*	*Reflection to Glass*	*Reflection to Air*
Design 1	60 nm	96 nm	4 %	0 %
Design 2	445 nm	162 nm	1.9 %	0.5 %

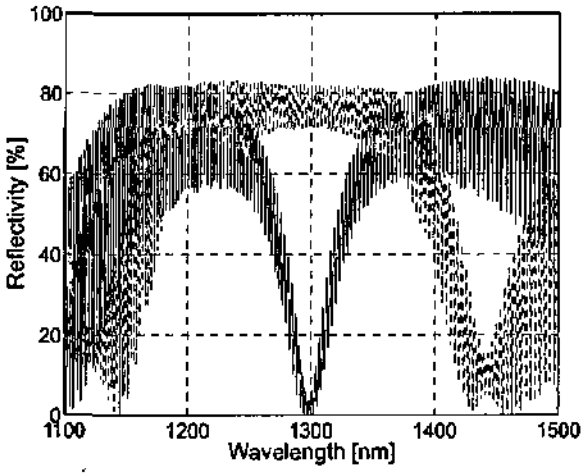

Figure 3.11: Simulated Reflection spectrum at an Fabry-Perot air gap of 1.55 µm (plain line) and a Fabry-Perot air gap of 1.3 µm (dashed line) taking into account the 1.9% reflection at the interface between fiber and the nitride-oxide coated substrate and the beam divergence.

In order to use the same nitride-oxide coating on the backside (Figure 3.6) as well, we have chosen the second design. Another good reason to use the second design is their thicker layer thickness permitting a smaller capacitance to the substrate and also technological considerations. To avoid, that the nitride layer is etched away during sacrificial layer etching, it should have a thickness above 140 nm, which can only be realised by the second coating.

However in the practical realisation it was observed, that a 2 % reflection at the fiber-substrate interface is too high. If this reflection is above 1 % the performance of the back illuminated modulator becomes wavelength and temperature dependent due to the parasite Fabry-Perot cavity between the bottom and top surface of the silicon substrate. As shown in the simulation of Figure 3.11 a 1 %,reflection of the backside AR-coating can generate variations of the On-state of more than 20 %[28]. Therefore the coating based on the standard oxide-nitride layers had to be replaced by a titanium oxide layer with a refractive index close to 2.3 in order to reduce the reflection to glass well below 0.5 %.

3.2.2. Mechanical modelling

3.2.2.1.Static mechanical response

The electro-mechanical behaviour of parallel plate electrostatic actuators is well described in literature[29]. The most simple approach is the lumped model[30],[31]. Here the membrane deformation is regarded to be uniform, i.e. the capacitor plates remain parallel. The lumped model consists of a single parallel-plate capacitor suspended above a ground plane by an ideal linear spring as shown in Figure 3.12.

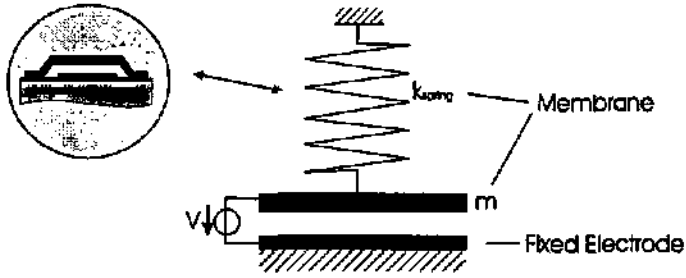

Figure 3.12: Lumped model of a deformable membrane electrostatic actuator.

At static equilibrium the elecrostatic force and the restoring spring force have to compensate each other:

$$kx = \frac{\varepsilon S}{2}\frac{V^2}{(g_0 - x)^2} \qquad (3.14)$$

where k is the spring constant, x is the displacement of the membrane center, g_0 is the initial gap, ε the permittivity of air, S the electrode area, and V is the applied voltage. The spring constant can be expressed in terms of the geometrical dimensions of the beam[32]:

$$k = 16E\frac{wt^3}{l^3} \qquad (3.15)$$

E is Young's modulus of polysilicon, l is the beam's length, t is its thickness and w its width. As the voltage is increased, the gap decreases until an instability or collapse condition is reached. With equation (3.14) and the fact, that at the pull-in

voltage the first derivative of the electrostatic force equals the spring constant, one can calculate the critical pull-in voltage V_p and the critical pull-in gap distance g_p [33]:

$$V_p = \sqrt{\frac{k}{\varepsilon S}\left(\frac{2g_0}{3}\right)^3} \qquad (3.16)$$

$$g_p = \frac{2g_0}{3} \qquad (3.17)$$

According to equation (3.17) only the first third of the initial airgap distance can be used for a stable actuation. If the membrane is deformed more than one third of the initial air gap g_0 the membrane collapses. The voltage necessary for pull-in has to exceed the value given by equation (3.16).

According to equation (3.16) the effect of a variation of the layer thickness on the pull-in voltage is:

$$V_p \propto \sqrt{t^3 g^3} \qquad (3.18)$$

Therefore an error of 5% in both the airgap and the membrane thickness results in a variation of the pull in voltage of 16 %.

To refine the lumped model the spring and electrode function of the free standing membrane can no longer be separated. On the one hand the membrane is a deformable electrode and the electrostatic force is maximum where the deformation is highest. On the other hand the spring constant can also be regarded as distributed, i.e. the electrostatic pressure close to the clamping end contributes little to the membrane deformation, whereas the electrostatic pressure in the membrane center contributes strongly. To take into account these two effects we have performed an FEM analysis with the commercial Ansys© program. We used two dimensional structural elements. The electrostatic pressure was calculated on every element with the built in APL (Ansys Programming Language) programming language. The electrostatic pressure is a function of the membrane deformation. To couple it with the structural analysis of the FEM program we used a Newton-Rephson algorithm which had also to be programmed in the APL language. In Figure 3.13 a) the lumped model is compared with the FEM simulation. In the lumped model the maximum membrane deformation is only one third of the air gap

height, whereas the FEM simulation indicates, that this deformation can be 40 % of the initial air gap height.

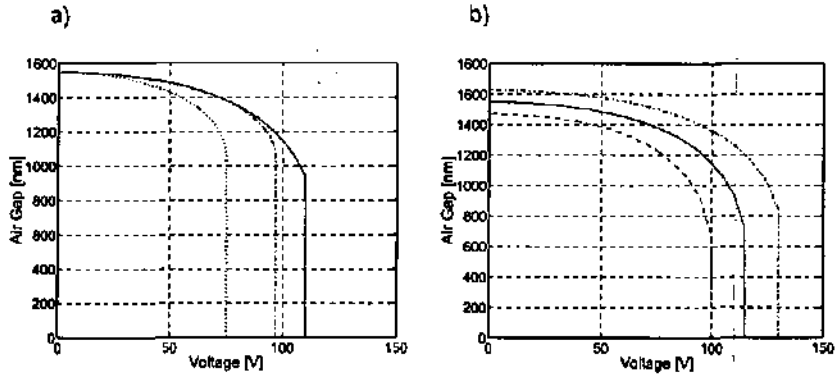

Figure 3.13: Simulated Electro-Mechanical behaviour of a 50 µm long, 0.47 µm thick beam. Initial air gap is g_0= 1.55 µm. a) Plain line shows the FEM simulation, dashed line shows the response according to equation (3.14), point-dashed line is the response according to equation (3.14) but supposing an active electrode area of 60 % of the total surface. b) FEM-simulated deformation - Voltage behaviour for minus 5% (dashed), 0 % (plain) and plus 5% (pint dashed) error in the layer thickness of the polysilicon membrane and the air gap.

In Figure 3.13 b) the influence of a ± 5 % variation in the air gap and polysilicon membrane thickness is simulated. As for the analytical calculation of equation (3.18) the shift in the pull in voltage is about ± 16 %. The relative shift of the bias-voltage, at which the membrane is pulled to an air gap of 1.3 µm, can attain up to ± 22 %. Thus not only the optical response but also the mechanical behaviour is strongly affected by errors in the layer thickness.

3.2.2.2. dynamic mechanical response

The maximum modulation speed of the device is limited by the mechanical movement of the membrane. If we admit a critically damped resonator, excluding overshoot ringing, then during one cycle of the membrane 2 bits of information can

be imprinted on the light. Thus the maximum modulation rate is about twice the resonant frequency of the membrane. For a simple beam structure the resonant frequency can be expressed by[33,34]:

$$f_{res} = \frac{1}{2\pi}\frac{4.73^2}{l^2}\sqrt{\frac{Et^2}{12\rho}}\sqrt{1+\frac{12}{4.73^2}\left(\frac{l}{t}\right)^2\frac{\sigma}{E}} \qquad (3.19)$$

The thickness t is fixed by optical considerations to be *468 nm*, i.e the beam thickness has to be an impair multiple of $\lambda/4n$ in order to get a high reflectivity layer. If the internal stress σ is zero, then the second square root in equation (3.19) is 1 and the only parameter to control the resonant frequency is the length l. For the Young's modulus we assume 170 GPa[33,35] and the density ρ at 2300 kg/m^3. The internal stress σ in the polysilicon membrane is process dependent. It can be adjusted at values close to zero or even slightly tensile[35]. For a beam length of 55 µm equation (3.19) yields a resonance frequency of 1.36 MHz; The frequency doesn't depend on the width of the beam, all the same this parameter is important in the design - it will be used to adjust the critical air damping. For a modulator with a maximum modulation speed of over 3 Mbit/s the beam length should be shorter than 52 µm in order to get a resonance frequency of over 1.5 MHz.

As explained in Figure 3.7, when at rest the modulator is in its high reflecting state, i.e. the air gap between the two mirrors should be 1.5 - 1.6 µm. To put the modulator into its low reflecting state a certain voltage (see Figure 3.13) is applied. To avoid switching between high voltage steps, preferably a DC bias is applied and a small AC modulation signal is superimposed. Due to the non-linear character of the electrostatic force the DC bias not only affects the static membrane displacement but also the dynamic behaviour. Actually the resonance frequency depends on the DC bias. This dependence can be expressed by a modified expression of the resonance frequency of an harmonic oscillator:

$$f_{res} = \frac{1}{2\pi}\sqrt{\frac{k_{eff}}{m}} = \frac{1}{2\pi}\sqrt{\frac{1}{m}\left(k-\frac{dF_{es}}{dx}\right)} \qquad (3.20)$$

where m is the equivalent mass of the membrane, and k_{eff} is the equivalent spring constant, composed of the mechanical spring constant k and an electrostatic spring

constant, which is the first derivative of the electrostatic force. Introducing equation (3.14) and (3.15) results in expression (3.21), which can be solved numerically:

$$f_m = \frac{1}{2\pi}\sqrt{\frac{1}{m}\left(k - \frac{\varepsilon S V^2}{(g_0 - x)^3}\right)} \qquad (3.21)$$

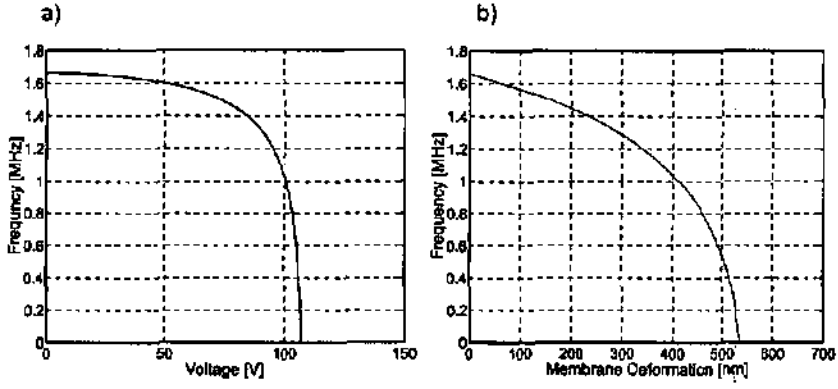

Figura 3.14: Resonance Frequency of the electrostatic membrane actuator. a) As a function of applied DC bias. At the pull-in voltage V_p the resonance frequency becomes numerically zero. b) As a function of membrane displacement. (Initial airgap = 1.65 µm, length 50 µm)

Figure 3.14 shows the dependence of the resonance frequency on the applied voltage or on the resulting deformation. It can be seen in graph a), that the resonance frequency drops drastically, when the bias voltage gets in the vicinity to the pull-in voltage. For the modulator design Figure 3.15 b) is more important. We have seen in the paragraph on optical modelling, that the air-gap height must be adjusted between 1200 nm and 1400 nm, if the modulator has to operate over a wavelength range of between 1275 and 1300 nm and if we admit an imprecision in the layer thickness of ± 5%. For an initial air gap height of 1.6 µm the membrane deformation can vary between 200 and 400 nm. According to Figure 3.15 b) this leads to a reduction of the initial resonance frequency between -16 % to - 37%. Thus also the modulation bandwidth is strongly affected by errors in the layer thickness.

3.2.2.3. scaling law between bandwidth and voltage

In the above considerations we have focused on a modulation bandwidth higher than 2 Mbit/s and we have seen, that for a frequency this high the actuation voltage is high. It is now interesting to see how a reduction in speed, i.e. the resonance frequency, will affect the necessary driving voltage. According to the lumped model the resonance frequency f can be expressed in terms of the spring constant k and the mass m:

$$f = \frac{1}{2\pi}\sqrt{\frac{k}{m}} \qquad (3.22)$$

The force F necessary to modulate the light is the displacement, which is in the order of $\lambda/4$ times the spring constant k:

$$F = \frac{\lambda}{4}k \qquad (3.23)$$

This force is generated by the applied voltage V values:

$$F = \frac{1}{2}\varepsilon\frac{S}{(g_0 - \frac{\lambda}{4})^2}V^2 \qquad (3.24)$$

,where S is the electrode surface and g_0 the initial air gap.
At equilibrium the spring force (3.23) has to neutralise the electrostatic force (3.24). Introducing equation (3.22) and (3.23) into equation (3.24) finally leads to an expression of the necessary driving voltage V as a function of the resonance frequency f:

$$V = fg_0\sqrt{\frac{2}{\varepsilon}t\rho} \qquad (3.25)$$

,where ρ is the density and t the thickness of the membrane. Thus the driving voltage varies linearly with the resonance frequency. A 500 kbit/s device with a resonance frequency of 250 kHz would need a driving voltage around 15 V only.

3.2.2.4. Air Damping

In order to damp the resonant mechanic oscillations the device is operated in atmospheric pressure. The major dissipation mechanism is the squeezed air film

between the free standing polysilicon membrane and the underlying electrode. To discuss the effect of geometrical variations on the damping behaviour we can describe the free standing polysilicon membrane with the differential equation of a damped harmonic oscillator with mass *m*, spring constant *k*, mechanical resistance *R* and and excitation force *f(t)*.

$$m\frac{d^2x}{dt^2} + R\frac{dx}{dt} + kx = f(t) \qquad (3.26)$$

For two parallel discs of area S, with average spacing g_0, the equivalent mechanical resistance is[37]:

$$R = \frac{3\mu S^2}{2\pi g_0^3} \qquad (3.27)$$

where μ is the air's viscosity (18x10-6 kg/ms for air at 20° C and atmospheric pressure). Notice the strong dependence on the air gap g_0 which has to be multiples of 650 nm, i.e multiples of half of the working wavelength. The above equation supposes parallel plate large discs and small vibration amplitudes with respect to the spacing g_0. In order to include large amplitude effects and non-parallel geometries a numerical solution of the Reynold's equation is necessary. This is a challenging topic which will not be further developed in this thesis. Recent interesting approaches to solve the Reynold's equation for micromechanical devices are presented in References[38],[39],[40]. It can be shown, that the viscous damping effect of the air dominates at low frequencies, but spring-like behaviour of the air-film predominates at higher frequencies[41].

For linear damped oscillators a characteristic of the damping is the so called quality factor, which expresses the ratio between the energy stored in the oscillator divided by the energy lost during a cycle of vibration. For a critical damped oscillator the quality factor, or simply Q-value, is 0.5; for underdamped oscillators the Q-value is larger than 0.5 and for overdamped structures the Q-value is lower than 0.5.

The quality factor Q can be expressed by the following equation:

$$Q = \frac{m}{R}\sqrt{\frac{k}{m}} = 2\pi\frac{m}{R}f \qquad (3.28)$$

In the case of a modulator structure with a simple beam shape the quality factor can be written as a function of the materials properties and the geomerical dimensions. Introducing equation (3.19) and (3.27) in above formula yields:

$$Q = \frac{2\pi 4.73^3}{3\mu}\sqrt{\frac{E\rho}{12}}\frac{t^3 g^3}{w l^3}\sqrt{1+\frac{12}{4.73}\left(\frac{l}{t}\right)^2\frac{\sigma}{E}} \qquad (3.29)$$

Admitting an internal stress close to zero above equation yields a quality factor of $Q = 1.9$ for a $l = 52$ µm long beam, which according to equation (3.19) would have a resonance frequency of 1.53 MHz. A quality factor above 1 is not advantageous. According to above equation the Q depends strongly on the geometrical dimensions:

$$Q \propto \frac{t^3 g^3}{w l^3} \qquad (3.30)$$

The thickness of the polysilicon beam t and of the air cushion g are fixed by the optical considerations. The only free parameters to adjust the Q-value are the length l and the width w of the membrane. Whereas the width w doesn't influence the resonance frequency, the length l has a strong effect on the resonance frequency, i.e. $\propto l^{-2}$, and also on the quality factor, i.e. $\propto l^{-3}$. For a decreasing length of the beam the quality factor increases at the third order but the resonance frequency only increases at the second order. Thus the quality factor increases faster than the resonance frequency for a given membrane thickness and air gap height. There exists a length and a corresponding frequency for which the quality factor is close to 1. The width w only allows a reduced tuning of the quality factor, because w shouldn't be too small to allow easy alignment of the fiber, on the other hand a too large width w can cause problems during the sacrificial oxide etching, because the nitride might be attacked. In addition too high a width to gap ratio can cause a nonlinear damping behaviour, i.e the pull-down movement may be damped more than the return movement. For the above example of a 55 µm long beam the width w resulting in a quality factor of 1 would be as large as 65 µm. For an assuming ideal width of 40 µm the corresponding length, i.e. resulting in a quality factor of 1, would be $l = 65$ µm. The corresponding resonance frequency would be 1.0 MHz. Thus for the simple beam design the maximum achievable modulation bandwidth is limited by the damping mechanism to about 2 Mbit/s, i.e. about twice the resonance frequency.

As shown in Table 3.3 for the simple beam design the damping can not be scaled with the resonance frequency. Actually for structures faster than 1 MHz the Q-value is larger than 1, which leads to undesired overshoot ringing.

Table 3.3: Calculated Resonance frequency and Q-value of beams for different lengths and a constant width of 40 µm.

Length	50	55	60	65	70
resonance frequency	1.66 MHz	1.37 MHz	1.15 MHz	980 kHz	846 kHz
Q-value	2.2	1.6	1.3	1	0.8

To increase the maximum modulation bandwidth while maintaining a damping response close to critical the resonance frequency has to be increased by design variations that allow an increased length for a given frequency. Under the condition to maintain the beam thickness *t* and of the air gap g, there exist three possibilities to increase the resonance frequency of the simple beam structure without increasing its length:

a) internal tensile stress

b) increased beam stiffness by profiled beam

c) clamping at more than two points

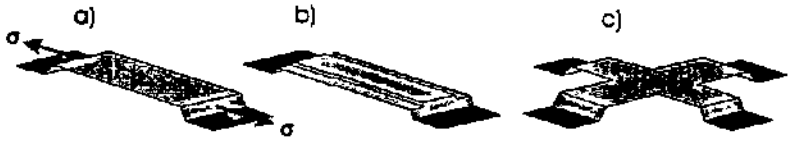

Figure 3.15: Design variations for an increased resonance frequency and maintaining a critical damping. a) Internal tensile stress, b) increased beam stiffness by profiled beam, c) clamping at more than two points.

The most important surface increase, respectively damping increase, - keeping the same resonance frequency - can be obtained with the design c). To determine the geometrical dimensions for a given resonance frequency we have performed an Finite Element analysis:

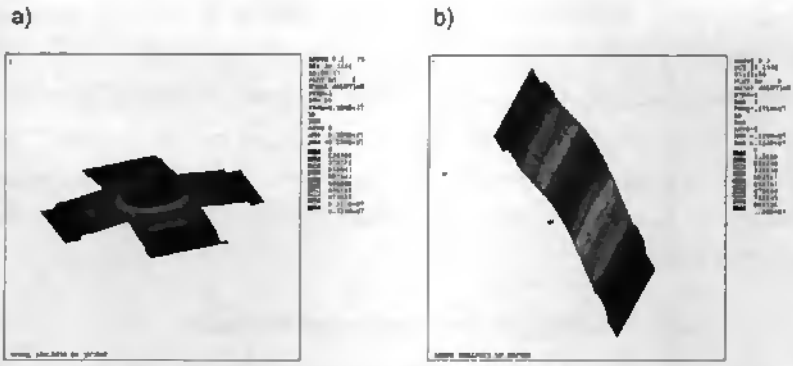

Figure 3.16: Finite Element modal Analysis. a) cross-type membrane with a resonance at 1.66 MHz. b) profiled beam. The resonance is at 1.71 MHz.

The resonance frequency is 1.66 MHz for a membrane width of 26 µm and a length of 60 µm; thus the length is 10 µm longer than for the simple beam design, which reduces the Q value according to equation (3.29) and (3.30) by 20 %. Internal stress is supposed to be zero.

On the other hand the design variation b) with a profiled beam structure not only increases the resonance frequency compared with a ordinary beam of the same length, but also the damping is increased by the smaller gap at the profiled regions.. Figure 3.16 b) shows the modal analysis of a 56 µm long beam. It has a resonance frequency of 1.72 MHz. The length is 7 µm longer than a simple beam design with the same resonance frequency. The reduction of the Q-value is 14 % when we only consider the increased length. If we take into account also the reduced gap height due to the profiled beam, the Q-value reduction is even higher. From a technological point of view the fabrication of profiled beams needs an additional mask, i.e. one additional photolithography and one etching step.

The third way to get a higher resonance frequency with the same beam dimensions is to build in tensile stress. With well tuned processing conditions tensile stresses higher than 100 MPa can be obtained in polysilicon[42]. According to equation (3.19) a 100 MPa tensile stress increases the resonance frequency of a 60 µm long beam by 250 %. To get the same resonance frequency as without stress the length can be

increased by 58 %. Thus also the Q-value could be reduced by almost 60 % for the same frequency.

With the combination of internal tensile stress and cross membrane design the maximum modulation frequency with still critical damping can be doubled, if we assume, that a Q-value between 1-2 is still acceptable. The maximum modulation bandwidth, which can be obtained with a micromechanical modulator may be as high as 6-10 Mbit/s.

3.2.3. Influence of Layer Thickness Mismatch

In the previous paragraphs it has been shown, that the operation wavelength and the imprecision of the layer thickness can change the optical (Figures 3.8 and 3.9), the static (Figure 3.13) and the dynamic (Figure 3.14) characteristics of the Fabry-Perot modulator. In this paragraph we will combine above simulation results. The four important parameters which describe the modulator performance are: *On-Off Contrast, Modulation Bandwidth, Extinction Voltage and Modulation Voltage*. In the following we will estimate how these four parameters are affected by the changing wavelength and by layer thickness variations.

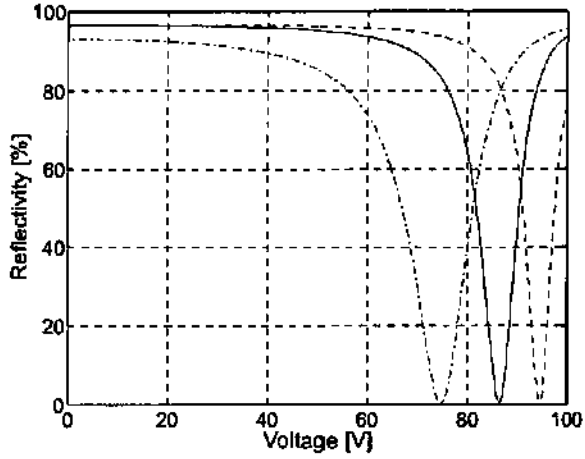

Figure 3.17: Simulated response at 1250 nm (dashed), at 1300 nm (plain) and at 1350 (point-dashed) without error in layer thickness.

Figure 3.17 shows the static electro-optic simulation for a wavelength of 1250 nm, 1300 nm and 1350 nm without an error in the layer thickness. This simulation was obtained by a combination of the simulation of Figure 3.7 and Figure 3.13. The initial air-gap was 1.55 µm. The extinction voltage, i.e. the voltage at minimum reflectivity is 75 V at 1350 nm, 86 V at 1300 nm and 94 V at 1250 nm. The voltage necessary to modulate the reflectivity between 80 % and the minimum is called the modulation voltage. At 1350 nm it is almost 20 V, whereas at 1250 nm already 8 V are sufficient. According to equation (3.21) respectively Figure 3.14 applying a bias voltage leads also to a decrease of the modulation bandwidth. For the ideal mirror thickness and an airgap of 1.55 µm this frequency variation is below 5 % between 1350 nm and 1250 nm operation wavelength.

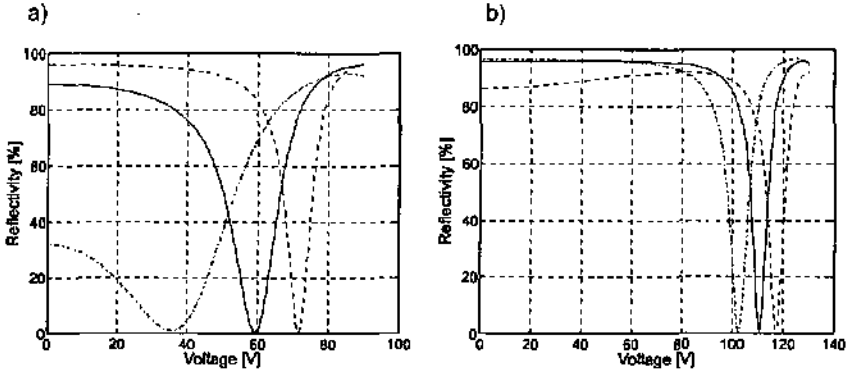

Figure 3.18: a) Response at 1250 nm, 1300 nm and 1350 nm with layers having a minus 5 % thickness error. b) Response at 1250 nm, 1300 nm and 1350 nm with layers having a plus 5 % thickness error.

In Figure 3.18 a) and b) the electro-optic response is simulated for an error in the layer thickness of minus 5 % in Figure 3.18 a) and a plus 5 % error in Figure 3.18 b). Not only the thickness of the mirrors but also the thickness of the initial air gap is changed by 5 %. The error in the layer thickness is introduced in that way, that all layers are 5 % too thick or 5% too thin. This leads to the biggest change of the air gap height at optical resonance, which in turn affects mostly the extinction voltage and the modulation voltage, but the On-Off ratio stays good for these errors. It was

shown on Figure 3.8 that the On-Off is affected when the error in the mirror thickness has opposite sign for the fixed and the moveable mirror.

Table 3.4: Effect of layer thickness and wavelength variation on the device characteristics.

thickness	ideal			ideal plus 5%			ideal minus 5%		
wavelength [μm]	1.25	1.30	1.35	1.25	1.30	1.35	1.25	1.30	1.35
On-Off ration [dB]	20	25	20	20	20	20	20	20	20
extinction Voltage [V]	92	86	75	117	111	103	72	59	38
modulation Voltage [V]	8	10	20	8	8	9	11	23	38
frequency [MHz]	1.3	1.38	1.46	1	1.2	1.26	1.38	1.45	1.5

The simulation results are summarised in Table 3.4. If we omit the response at 1350 nm of the minus 5 % error simulation, where the initial air gap got too thin to allow a correct modulation, we can see, that the extinction voltage can vary between 60 V and over 110 V. This wide scatter is above all due to the large effect of the error in the air gap thickness. For a perfect air gap thickness this extinction voltage can only vary between 65 V and 96 V over the wavelength range and admitting an error in the mirror thickness of 5 %, which is not far away from the values for the ideal response, which is between 75 V and 92 V. The modulation voltage is much less affected as long as the membrane deformation for modulation stays high enough, i.e. when the initial air gap is not too thin and the working wavelength 1350 nm. At higher initial air gaps a modulation voltage below 10 V is sufficient, but for the longer wavelength or low air-gaps modulation voltages up to 20 V are necessary.

The drawback of high initial air gaps, i.e. higher than 1.6 μm is the increased extinction voltage and the reduced bandwidth. At a plus 5% error the bandwidth may be reduced as much as 40 % due to the electrostatic spring softening. This result may be surprising: the membrane is 5 % thicker and therefore much stiffer. Nevertheless at the necessary bias voltage the bandwidth is lower than for the ideal thickness. This is because also the air gap is increased by 5 % resulting in an

increased bias voltage. This bias voltage softens the equivalent spring and reduces the resonance frequency. An excellent control of the air gap thickness better than ± 2% is thus necessary to reduce the scatter in the bandwidth and in the bias voltage. On the other hand for the mirror layers a precision of +/- 5 % can be accepted.

3.3. Fabrication

Fabrication is based on polysilicon surface micromachining a well established technology in the MEMS (micro-electro-mechanical-systems) field. However a number of process modification are necessary in order to meet the special requirements of the reflective modulator. First to bring the fiber sufficiently close to the modulator a hole is etched into the backside of the wafer. The bottom of the hole has to be AR-coated in order to avoid a second Fabry-Perot cavity between the fiber end and the modulator. So the conventional single side process becomes a double side process, where care has to be taken to ensure the compatibility of the processing done on the top surface with those done on the bottom layers. A second concern is the conservation of the thickness of the layers troughout the process. Not only the layers have to be deposited with a high precision and uniformity, but the layer thickness has also be conserved throughout the process.

3.3.1. Polysilicon Surface Micromachining

Polysilicon micromachining has become a powerful tool for the fabrication of integrated sensors and already has found application in a commercialised accelerometer. Polysilicon's popularity is a direct results of its mechanical properties and its relatively well-developed deposition and processing technologies, which shares many common features with current IC technology. The electrical and mechanical properties, i.e. the resistivity and the internal tensile or compressive stress, can be tailored in choosing appropriate processing conditions. This characteristic makes polysilicon very attractive but also has its inherent difficulties. Good introductions on polysilicon micromachining can be found in textbooks on the MEMS technology[43] or in review articles[44,45].

The fabrication sequence of the reflective modulator is based on a total number of 6 masks, starting with a thick oxidation for a anisotropic wet etching mask. The backside oxide is structured and holes are etched using 40% KOH solution at 60° C. To allow a passive alignment the bottom dimension of the hole has to fit to the cladding diameter of the fiber. We measured the dimension of the hole in an optical microscope with an optical ruler and time stopped the etching.

After stripping the KOH-etching mask a passivating anti-reflection coating is deposited. It consists of a wet silicon dioxide and a low pressure chemical vapour deposited (LPCVD) silicon nitride. These layers have a thickness of 445 nm and 162 nm respectively according to Table 3.2.

The next step is the double side alignment to define the alignment marks and the substrate contact holes on the top surface. This alignment has to be done in a precision better than +/- 5 μm to make sure that the passive alignment works correctly. Substrate contact holes are opened through the anti-reflection coating by plasma etching. Then a 280 nm thick LPCVD polysilicon is deposited and structured by plasma etching. This conductive layer serves as the first mirror and the bottom electrode.

The next step is the chemical vapor deposition of a 1.55 µm thick phosphorus doped sacrificial oxide (PSG). High phosphorus content can result in PSG reflow[45] or dewetting, manifested in structural layer deformation during high temperature stress relaxation cycles. This problem is circumvented by employing a composite sacrificial film[47]. Two third of the thickness is composed of highly doped PSG and the top third of non doped silicon dioxide. The sacrificial oxide is structured in buffered hydrofluoric acid. Then the second LPCVD polysilicon is deposited. In order to get a sufficient mechanical stability it has a thickness of 464 nm, $\frac{5}{4}\lambda/n$.

This polysilicon layer will serve as the mechanically active membrane. The control of its mechanical properties and internal stress is of primary importance. Many researchers have reported on the effect of the processing conditions on the mechanical properties of polysilicon layers deposited by LPCVD[48],[49],[50]. The mechnical properties, i.e. Young's modulus and internal stress are dependent on

deposition, doping and subsequent annealing steps. Although subsequent annealing can reduce a lot of the as-deposited-film stress, the initial microstructure will contribute significantly to ultimate film properties. Typically both fully amorphous and fully polycrystalline as-deposited LPCVD silicon films are in a state of compression with stress magnitudes ranging up to ca. 700 MPa[51],[52]. In order to reverse the as-deposited compressive stress into a beneficial tensile stress polysilicon has to be deposited at temperatures corresponding to the transition temperatures between amorphous and crystalline material ranging from 560-600 °C [53],[54]. For LPCVD silicon films deposited under these conditions, the magnitude and sign of the as-deposited stresses extremely depend on process conditions and typically range from +500 MPa tension to - 500 MPa compression[50],[35],[55],[56],[57]. It is reported, and we could reconfirm this result in our laboratory, that initial compressive layers change the sign of stress if the amorphous silicon present in the film matrix is recrystalized in an annealing step above 625° C[58]. The art of polysilicon micromachining consists in adjusting the amount of amorphous polysilicon in the as-deposited layer with subsequent annealing and doping steps in order to get a reproduceable, slighly tensile stressed film. The polysilicon used for the reflective modulator is deposited at a temperature of 570 °C, silane flow rate and furnace pressure are adjusted to get a deposition rate of 35 Å/min[59],[33]. Under these conditions wafer bow measurements indicate a compressive stress of the as-deposited film of -240 MPa. After recrystallisation of the polysilicon film at 625° C the as-deposited compressive stress is reversed into a tensile stress as high as 190 MPa.

Table 3.5: Measured stress in polysilicon at IMT

	as-deposited film stress	**annealing 1050°C, 30 min**	**annealing 1050°C, 30min, doped P**	**annealing 950°C, 30 min, doped P**
Deposition at 600°C	- 200 MPa	- 20 MPa	- 20 MPa - - 50 MPa	compressive
Deposition at 570°C	- 230 MPa	± 5 MPa	± 10 MPa	+ 100 MPa (tensile !)

To reduce the internal stress near to zero and to dope the polysilicon film an annealing step is performed. During this step the polysilicon layer is doped from a phosphorus-doped oxide deposited on top the polysilicon. As the sacrificial oxide, this oxide also is composed of a doped non-doped composite oxide in order to prevent structural layer deformation. The process used to dope polysilicon films can have significant impact on electrical, chemical and mechanical properties[60],[61],[62]. At our institute the process parameters used are an anneal step at 1050 °C during 30 minutes. We obtained a sheet resistance of 300 - 500 Ohm/square. The stress in the annealed film is close to zero; between 2 - 10 MPa tensile were measured. In case of a too high doping at 100 Ohm/square at 1050° C the tensile stress is again reversed into slight compressive stress. If the annealing is performed at temperature too low the stress is not completely released. After doping and annealing at 950° C the tensile stress was still 100 MPa.

At the higher deposition temperature of 600 °C the stress release is more doping dependent. At a slight doping to 500 Ohm/square a compressive stress around -20 MPa was obtained. A too important doping to 100 Ohm/square could result in a compressive stress of -50 MPa. At an annealing temperature of 950 °C the compressive stress could not be sufficiently reduced. Table 3.5 summarizes the stress measurements for two different deposition temperatures and various annealing steps.

After removal of the doping oxide the top polysilicon layer is plasma structured. This plasma etching is anisotropic and results in nearly vertical sidewalls. Due to this anisotropy it should be taken care, that no etching has to be done on steps , as for example on the 1.5 μm high sacrificial oxide step. LPCVD polysilicon has very good step coverage; at such steps the polysilicon can only be removed by a long overetching which may destroy other sensitive parts of the structure. If the overetching is not complete small polysilicon wires persist on these steps.

The layers on the backside of the wafer are now stripped and the wafer is anti-reflective coated with titanium oxide. Titanium oxide is a high refraction index material with an index *n* between 2.2 - 2.3[63] for an amorphous layer.

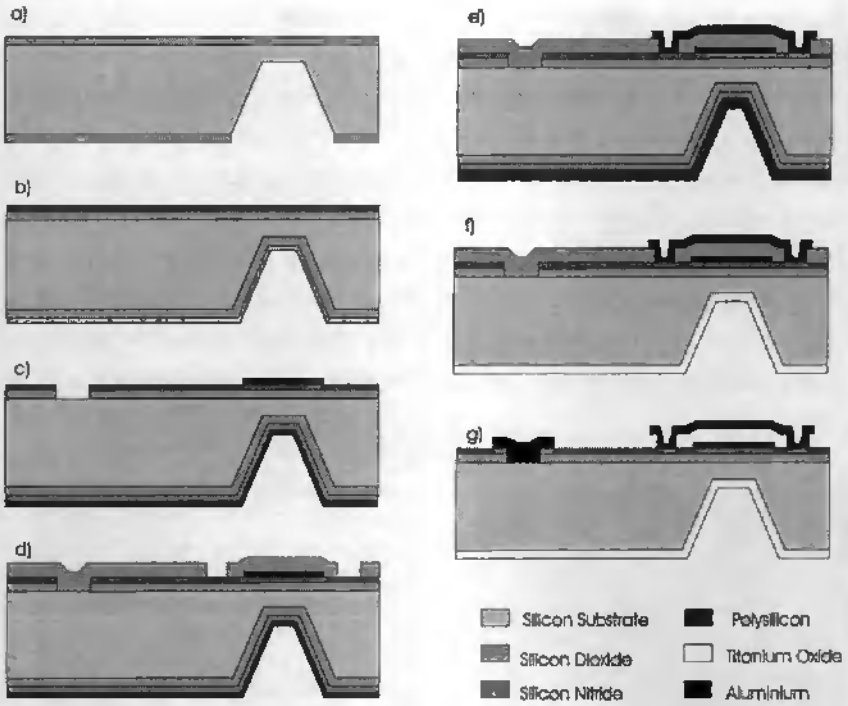

Figure 3.19: Schematic process flow for the fabrication of the modulator:

a) silicon dioxide mask and KOH etching

b) deposition of oxide (440 - 450 nm) and nitride (155 - 170 nm) AR-coating

c) opening of Contact holes, Polysilicon 1 (280 - 300 nm) deposition and structuring

d) sacrificial oxide (1.55 - 1.6 μm) deposition and structuring

e) polysilicon 2 (470 - 490 nm) deposition, doping, annealing and structuring

f) Stripping of backside layers and deposition of AR-coating

g) sacrificial layer etching and metalisation

With the TiO_2 coating it is possible to match the index of silicon to that of the fiber and to reduce the back-reflection below 0.5 % over the working wavelength range. The sacrificial oxide is then etched in hydrofluoric acid to obtain free standing polysilicon structures. Depending on the etch solution used considerable attack of

the polysilicon can occur leading to a non-uniform layer thickness of the thin film mirrors. We have obtained best results with 50% HF at ambient temperature. Attack of polysilicon was not measurable, but the etch rate of nitride can be as high as 200 Å/min. The etch rate of PSG with 4% Phosphorus content is 10 µm/min in a fresh etch solution. To free the membranes a 3 minutes etch was sufficient; thus leaving intact a sufficiently thick nitride for substrate insulation. After the sacrificial layer etching a special drying process has to be applied to prevent the membranes from sticking to the substrate. When the water is dried without precaution capillary forces appear on the liquid-air interface. In the small gap between the membrane and the substrate this force pulls the membrane down to the substrate, where it can remain stuck.

a) b)

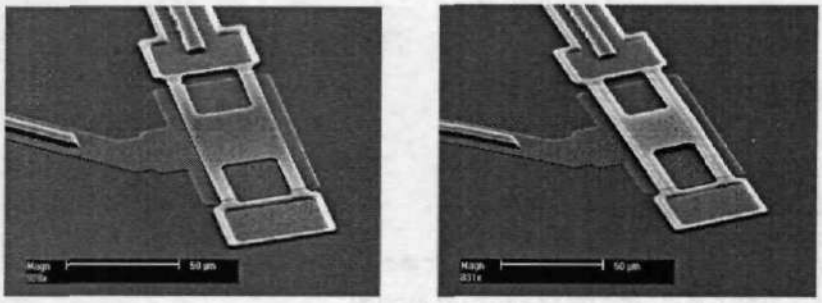

Figure 3.20: Sticking after the free-etching of the membranes. a) Stuck membrane. b) free standing membrane - Stiction is prevented by a profiled beam suspension.

To reduce this sticking several methods have been proposed. The simplest and most widespread method is to use ispropanol alcohol *(IPA)* as the last rinsing agent[64]. *IPA* has a low surface tension and the water is well dissolved. The water is supposed to be responsible for the permanent hydrogen bonding of the microstructures. It has been shown, that a rough surface can considerably reduce sticking[65] as is shown in Figure 3.20 where the surface roughness is increased by a profiled beam structure. Also mono-layer coatings, which reduce the surface tension at the interface, have been proposed[66]. Others methods have been developed which completely eliminate the capillary forces. In the supercritical CO_2 drying process, first reported by *Multhern et al.*[67] liquid is transferred to vapour via the supercritical

phase. Carbon dioxide is used because of its low critical temperature T_c = 31.1 °C, p_c = 72.8 bar. During evaporation of the carbon dioxide no liquid-vapour interface exists, so there are no capillary forces working. Another approach for the liquid removing without capillary forces is the freeze-dry method first applied to micromachining by *Guckel et al*[68]. The liquid surrounding the wafer is frozen and the solid is than removed by sublimation. Cyclohexane was found to be a practical solvent for freeze drying because its melting point is at 6 °C and the sublimation can be done at atmospheric pressure in a nitrogen ambient[69]. After the sacrificial layer etching a 2 µm thick aluminium layer is evaporated and structured for the contact lines. In this step aluminium is evaporated on the free standing polysilicon membranes, which are frozen in the aluminium layer. So conventional IC processing as spinning can be carried out on the micromechanical structures.

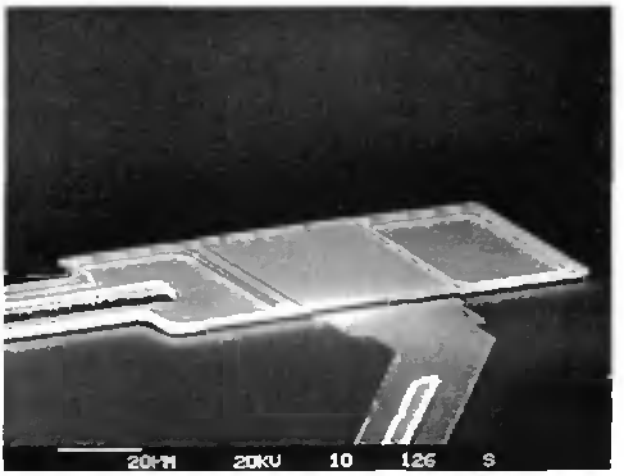

Figure 3.21: SEM photograph of a finished device.

3.3.2. Limitations of the Fabrication

There are various process imperfections which may reduce the device performance. The effect of errors in the layer thickness of the films has been discussed in the modelling chapter and it was shown that a precision better than ± 5% is necessary

for the polysilicon mirrors and the AR-coating, whereas the air-gap should be defined better than ± 2%.

The precision which can be reached depends above all on the deposition equipment used. Modern deposition furnaces are capable of producing very uniform layers with a reproduceabilty within a 1 % variation. An error in layer thickness can be classified in three different classes: first there is the non-uniformity on a single wafer. If the deposition is carried out on a whole batch of wafers there might also be an on-batch variation. For example the film thickness on the first wafer is different from the film thickness on the last wafer. Finally there might be a variation from one deposition run to the next.

For the polysilicon and nitride deposition we used low pressure chemical wafer deposition (LPCVD), which resulted in very uniform depositions, but the run-to-run variation was not better than ± 3 %. Still this is sufficient for these layers. A major concern is the sacrificial oxide, which has to be very precise. We tried first a atmospheric pressure CVD available at the IMT laboratory, which yielded layers with a 5 % non-uniformity over the wafer surface. To get better more reproduceable results we got LPCVD depositions of the sacrificial oxide done at CSEM, Switzerland.

Another concern with optical films is their roughness. It has been reported, that the surface roughness of polysilicon can be affected by the deposition conditions. For 0.5 µm thick polysilicon a roughness value as low as 8 Å rms is reported in litterature[70]. For thicker polysilicon films the roughness increases and for optical applications of 5 µm thick polysilicon structures even chemical-mechanical polishing was used to reduce the roughness from 400 Å Ra below 17 Å Ra[71]. For our 0.5 µm mirrors roughness hasn't been a concern.

Another roughness problem can arise from the surface roughness of surfaces etched in anisotropic wet etching such as KOH, TMAH, EDP. Due to the roughness part of the light is scattered away and is lost. Figure 3.22 shows a measurement with a confocal microscope of a typical aspect of a 300 µm deep etched bottom surface of an (100) wafer. The surface has an orange peel aspect, the height of the notches are up to 0.2 µm. In the micromachining community there has developed considerable folklore and hear say about the nature of this roughness.

a) b)

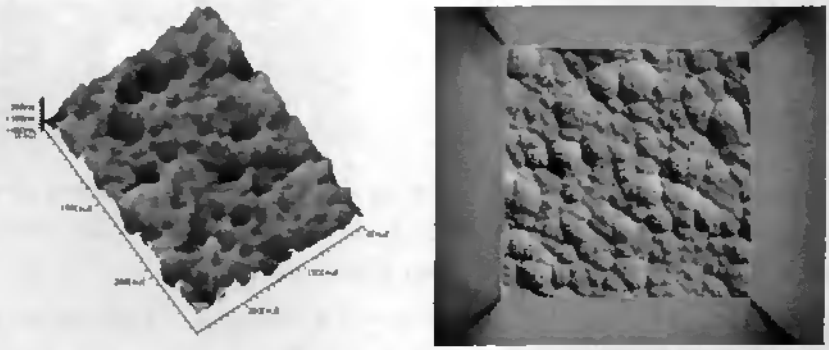

Figure 3.22: a) Measurement of surface roughness of KOH etched (100) surface with a scanning confocal microscope (UBM) after 300 µm deep etching. Ra roughness is 110 nm. Hole size is 300 x 300 micron. b) Same Surface in an optical microscope in phase contrast mode (Normaski).

In references[72,73,74] the effect of KOH concentration and temperature on the roughness has been studied. They found that etching at temperatures higher than 60°C and at concentration of 30 % gave best results.Other researcher have reported that the roughness can be considerably reduced by a clean etching bath[75,76,79], by preventing of CO_2[78] contamination respectively metal contamination[76], by reducing high temperature processing steps[77], by adding hydrogen peroxide to the etching bath[78]. Cambell et al. even claimed obtaining "atomically flat etch surfaces" by oxygen bubbling and adding isopropanol to the etching bath[79], which couldn't be reproduced in our laboratory. Others observed that very resistive silicon(> 2000 Ωcm) fabricated by the float zone technique[80] leads to mirror polished surfaces.

In our experience the silicon quality can have a considerable influence on the aspect of etched surfaces. But we haven't been able to suppress the roughness just by modifying the etching parameters and the substrate material. To completely avoid any surface roughness we have used buried oxide wafers, so called Silicon-on-Insulator wafers (SOI). Figure 3.23 illustrates the etch stopping with a buried oxide.

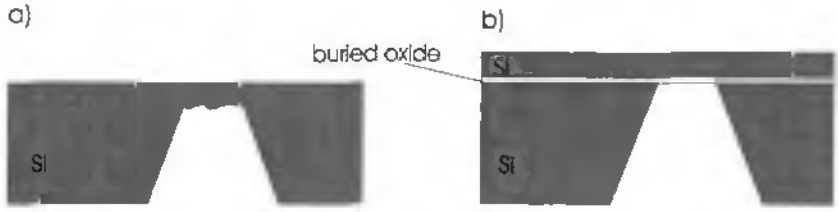

Figure 3.23: a) Etching holes in KOH of conventional wafers results in a bottom roughness of 0.1 µm rms. b) Etch stopping on the buried oxide of SOI wafers eliminates the bottom roughness in the hole.

In Figure 3.24 the extinction ratio of modulators with a conventional KOH hole and a SOI etch-stopped hole arecompared. A single mode fiber is scanned over a surface of 60 x 60 µm in the backside hole. For the conventionally etched hole the extinction ratio is distributed in a less homogenous manner than for the SOI wafer. This is due to the influence of the light scattering and focalisation in relation with the surface roughness. Also the diameter of the region, in which a maximum extinction ratio is obtained, is smaller for the conventionally etched hole.

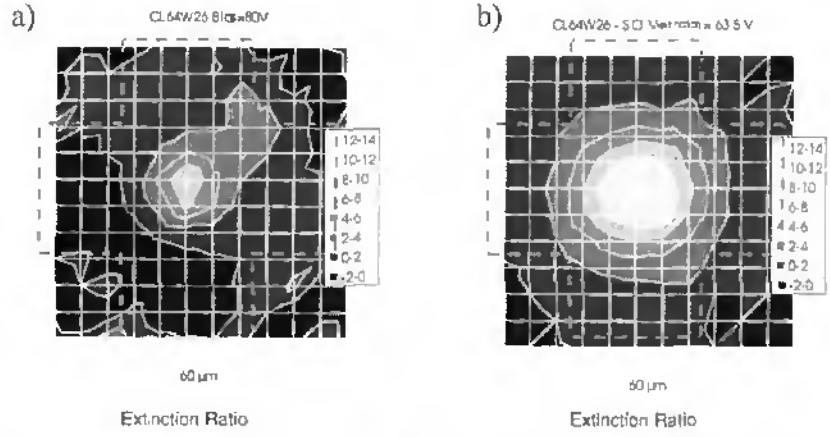

Figure 3.24: Extinction ratio when the modulator is illuminated from the backside hole, scanned over the etched surface. a) KOH-hole of conventionally wafer. Extinction voltage is 80 V. b) hole of SOI-wafer. Extinction voltage is 63.5 V. Note, that the reduced the fiber position tolerance

of a) is due to the higher membrane deformation at 80 V, i.e. a higher initial air gap, and not due to the surface roughness (measurement O. Anthamatten, Ascom Tech AG)

But this effect is not due to the surface roughness in the KOH hole but due to the different air-gaps of the two modulators. Actually for the modulator on the SOI wafer already 63.5 V are sufficient to extinct the light signal, i.e. the air gap between the polysilicon mirrors is about 1.51 µm, whereas for the modulator on the conventional wafer over 80 V are necessary for modulation. This modulator has an initial air gap of 1.6 µm. Thus the polysilicon membrane is much more deformed for the first modulator than on the SOI wafer, which reduces the area of maximum extinction ratio. *All the same both modulators achieve an extinction ratio over 12 dB; the* performance degradation due to the surface roughness is not dramatic, therefore the use of conventional wafers is acceptable.

Another method for eliminating the surface roughness is electropolishing[81]. By anodic polarization of silicon in aqueous solution a surface oxide is formed, which is etched away by hydrofluoric acid (HF). Depending on the substrate type, i. e. *n* or *p*, its resistivity and the applied polarisation voltage either porous silicon formation or electropolishing occurs. In our surface micromachining process we have to use *n* type silicon, because micromechanical polysilicon is preferably Phosphorus doped. N type silicon yielded very bad electropolishing results. Porous silicon formation could not be eliminated, which resulted in a brown surface aspect. So this method was not further pursued, but *p* type silicon may give better results.

3.4. Characterisation of Reflective Modulator

3.4.1. Measurement Set-Up

A schematic view of the experimental set-up is shown in Figure 3.25 and Figure 3.26. The Set-up of Figure 3.25 allows fast measurements using prober needles for contacting the chip. The set-up of Figure 3.26 needs a longer preparation but is more stable and is the configuration used in the packaged devices.

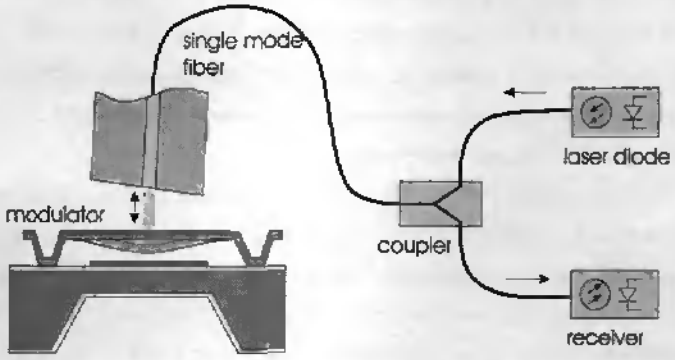

Figure 3.25: Measurement Set-Up for fast characterisation, which can be used for on wafer measurements.

As shown in Figure 3.25 a single mode fiber is aligned above the modulator. In order to eliminate the 4% reflection at the fiber-air interface, the fiber end is polished at an angle of about 8°. The light reflected from the interface is not guided in the fiber-core anymore and is transmitted into the cladding and lost. If a fiber without an angle at the end was used, a second Fabry-Perot cavity would be formed between the modulator and the fiber end. In this case the response of the modulator would be very sensitive to the distance between the fiber and the modulator. The fiber for measurement is connected to the input of a directional coupler with a laser diode and a photodiode receiver at its outputs. Depending on the voltage applied to the modulator more or less light is reflected back into the fiber and detected at the receiver end.

In the second configuration shown in Figure 3.26 the modulator is illuminated form the backside hole.

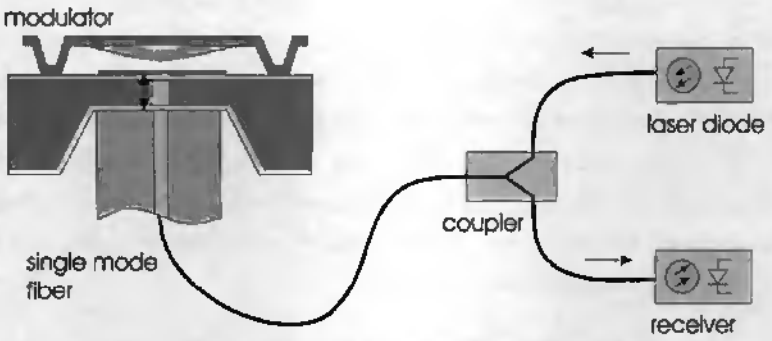

Figure 3.26: Placing the fiber in the back side KOH-hole is the configuration used in the packaged devices.

3.4.2. High Speed modulator

3.4.2.1. static response

When zero voltage is applied on the Fabry-Perot modulator, the air-gap between the two mirrors is 1.6 µm and the modulator is in its high reflecting state. About 50 - 70 % of the light are returned back into the single mode fiber resulting in a typical insertion loss of 1 - 3 dB. The distance between the fiber end and the modulator is 70 µm; with such a fiber-modulator separation theoretically an insertion loss in the vicinity of 1 dB is possible. But in addition to the loss due to the beam divergence light loss arises from an angular misalignment and light scattering at the anti-reflective coated silicon-fiber interface. The hole was fabricated by crystallographically selective wet etching, which introduces a surface roughness of 0.1 µm Ra.

When a voltage is applied an electrostatic force arises between the two mirrors and the free standing polysilicon membrane is deformed. To put the modulator in its low reflecting state the voltage has to be increased until the air gap gets close to the wavelength, i.e. for different wavelengths different actuation voltages will be necessary. Figure 3.27 shows the voltage-reflection curve for a wavelength of 1260 nm, 1300 nm and 1350 nm. At 1260 nm the deformation must be higher than at

1300 nm or 1360 nm to put the Fabry-Perot in optical resonance. Therefore the applied voltage must be higher at shorter wavelengths. At a wavelength of 1360 nm the extinction voltage, i.e. the voltage with the minimum in reflectivity, is 78 V, at 1300 nm the extinction voltage is 87 V and at 1260 nm already 92 V are necessary. Whereas at 1360 nm an On-Off ration higher than 15 dB is achieved, at 1300 nm and 1260 nm the On-Off ratio gets smaller but stays above 9 dB in any case. This reduction in the modulation contrast is due to a slightly too thick polysilicon membrane on the one hand and to the increased membrane bending at shorter wavelengths on the other hand. In both cases the reflectivity of the free standing membrane is reduced at shorter wavelengths.

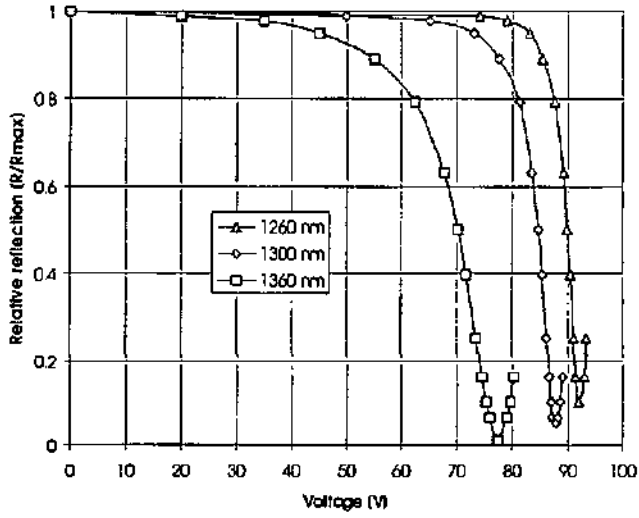

Figure 3.27: Normalized reflectivity of the modulator as a function of applied voltage for 1360 nm, 1300 nm and 1260 nm.

To modulate the reflectivity between 80 % and its minimum, a 17 Vpp signal must be superimposed on a bias voltage of 69 V at 1360 nm. At 1300 nm and 1260 nm 5 Vpp signal is already sufficient, whereas the bias voltage must be higher. At shorter wavelength the modulation signal can be lower because of the non-linear character of the electrostatic force, which is proportional to V^2/d^2, where V is the bias voltage

and d the gap between the electrodes. Therefore at a higher bias voltage a superimposed modulation signal yields a higher deformation amplitude.

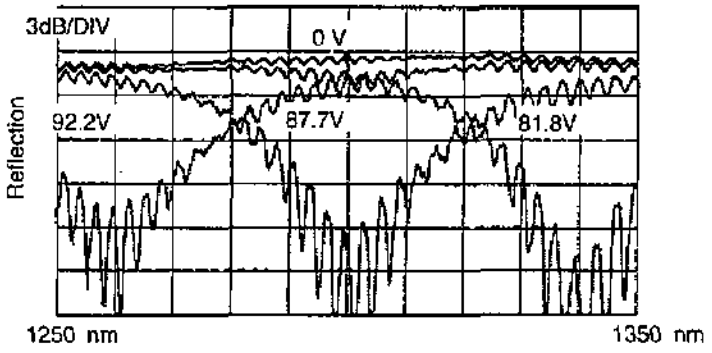

Figure 3.28: Spectral response of the modulator at 0 V, 81.8 V, 87.7V and 92.2 yielding a minimum in reflectivity at 1340 nm, 1300 nm and 1260 nm. The vertical scale is in dB.

Figure 3.28 shows the spectral response of the back-illuminated modulator at different voltages. At 0 V the reflectivity is constant within 1.5 dB with a spectral ripple of 0.8 - 1 dB superimposed. This comes from a residual backreflection of about 0.5 % in the alignment hole at the silicon - fiber interface. This wavelength ripple is relatively increased in the low reflection state, but is of reduced importance here. For an applied voltage of 81.7 V the reflectivity is reduced by 12-15 dB around 1340 nm. Here the spectral width of the 10 dB attenuation is 10 nm. As for the measurement of Figure 3.27 also the spectral response shows a reduction of the contrast at shorter wavelengths. But due to the ripple with a narrow-band laser the contrast can increase considerably.

Because the Fabry-Perot principle is based on interference effects the modulator is inherently wavelength dependent. With a spectral width of approximately 10 nm also wide band laser diodes can well be modulated. But to compensate for wavelength drift and to be able to adapt automatically to different wavelength a feed back control of the bias voltage of the modulator is necessary. This can be realised by mounting a monitor photodiode on the modulator. This photodiode will also be used for detecting the downstream data signal.

3.4.2.2. Dynamic response

The maximum modulation speed of the Fabry-Perot is limited by the mechanical movement of the free standing membrane. The movement of the membrane can be described as a damped spring - mass system. The modulation bandwidth of such a mechanical system is maximum if overshot ringing and overdamping is avoided, thus the damping should neither be too weak nor too strong i.e. close to critical. This is achieved by ajusting the width of the free-standing membrane and operating the device at atmospheric pressure to take advantage of air damping. Figure 3.29 a) shows the large signal step response of the modulator to a 3.5 *Vpp* square wave at a bias voltage of 84.5 *V*. The response is slightly underdamped with some overshot cycles corresponding to a Q value of 1.6. Their amplitude is about 10 % of the maximum signal. This overshot ringing is low enough to allow a clear definition of the On and Off state at a speed as high as the resonance frequency. Figure 3.29 b) shows a close-up view of the rise and fall time of the modulator. The fall time form 90 % to 10 % is 170 ns, whereas the rise time form 10 % to 90 % is 200 ns. This 17 % slower rise time is explained by nonlinear damping, which is slightly higher in the rise cycle than in the fall cycle.

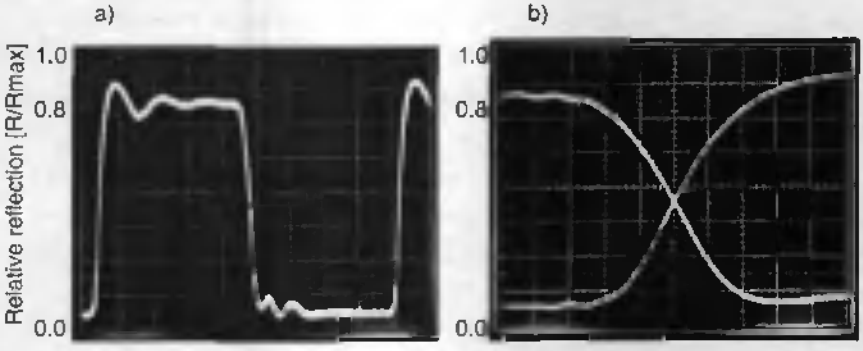

Figure 3.29: Large signal step response to +/- 3.5 V square wave with a 84.5 bias voltage. A) modulator response at 220 kHz. (Time scale: 0.5µs/div) B) close-up view of rise and fall times. (Time scale: 0.05µs/div)

According to Figure 3.30 the -3 dB small signal bandwidth is 1.64 MHz. The Q-value is 1.5, which is low enough to keep the influence of the overshoot ringing small. The modulator characteristics are summarized in Table 3.6.

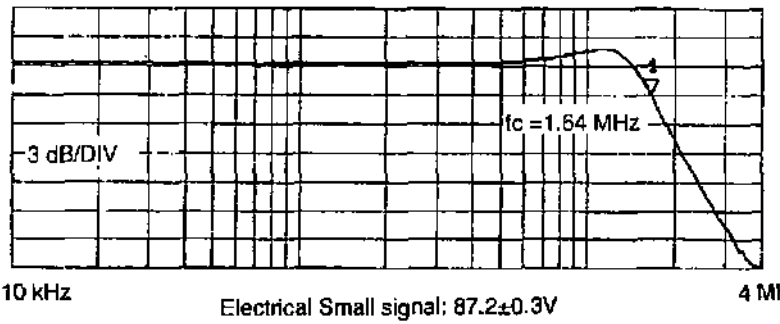

Figure 3.30: Small signal frequency response of a cross type membrane. The -3 dB bandwidth is 1.64 MHz.

Table 3.6: Measured Modulator Characteristics:

wavelength	Insertion loss	On-Off ratio	Bias Voltage	Modulation Voltage V_{pp}	rise time
1260 nm		9 dB	90 V	5 V	
1310 nm	< 3 dB	10 dB	84 V	7 V	200 ns
1360 nm		15 dB	69 V	17 V	

If we compare the frequency response of the 60 µm long cross membrane with a simple beam design of 55 µm length we can observe a similar bandwidth with a resonance frequency at atmospheric pressure of about 1.4 MHz, but the damping is considerably weaker. At resonance an amplitude increase of about 5 dB is observed, which corresponds to a Q-value of about 4.

In order to reduce further the overshot ringing we have fabricated beam and cross type membranes with larger widths. It was observed, that the frequency response becames non-linear if the width was too large. Already above 100 kHz a first attenuation of about 3 dB was observed and at resonance a peak of 3 - 5 dB was still present. The step response of such non-linear modulators showed different

response times for the rise and fall cycle. For beam type membranes with an initial airgap height of 1.55 μm the maximum width was 45 μm to keep a linear damping response. For cross type membranes the maximum width was 30 μm.

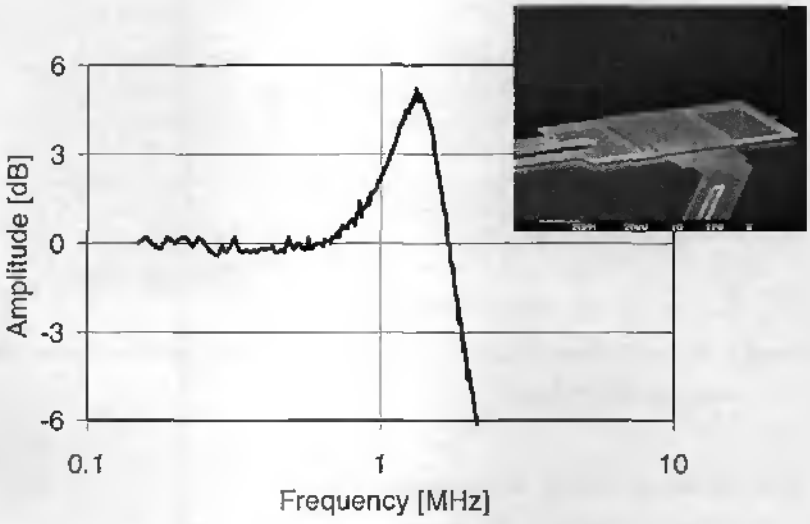

Figure 3.31: Frequency response of a beam-type modulator. Resonance frequency is at 1.4 MHz at a bias voltage of 70 V. The Q-value is 4. (Length 55 μm; Width 40 μm)

3.4.3. Low Speed Modulator

3.4.3.1. Static response

Many applications like battery powered communication links require a low power consumption and thus a low operation voltage. To reduce the operation voltage the membrane has to be made softer, and thus modulation will become slower. It has been shown with equation (3.25), that there is a linear dependence between the bias voltage and the modulation bandwidth. Figure 3.32 shows the static response of the reflectivity of a 130 μm long modulator. The DC bias voltage is only 24 and a +/- 2 V signal is sufficient to modulate at an extinction ratio over 12 dB.

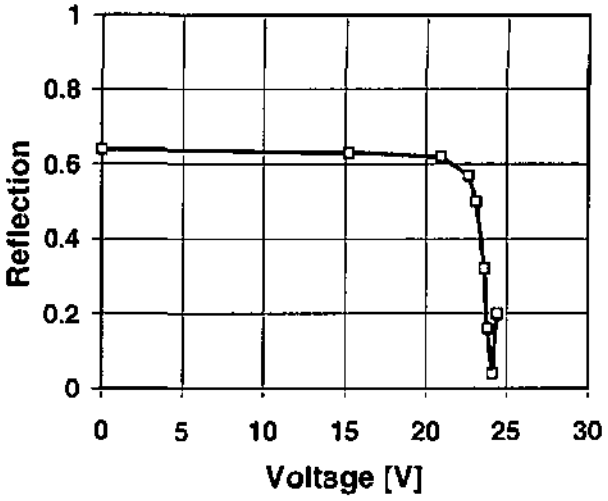

Figure 3.32: Static reflectivity response of a modulator of reduced speed. Necessary bias voltage is 24 V. On-Off ratio is 12 dB.

3.4.3.2. Dynamic response

Contrary to the high speed membranes where damping is too weak, the damping of membranes with a resonance frequency of a few 100 kHz is too strong and it has to be reduced by venting holes in the membrane. As shown in Figure 3.33 the frequency response can be very flat with almost no overshot with appropriate venting holes in the membrane. Below modulator shows a resonsonce frequency of about 200 kHz. Damping is almost critical with an amplitude increase of only 1.5 dB. The maximum modulation rate of this modulator was measured to be over 600 kBit/s. Typical modulator performance is summarised in Table 3.7.

Table 3.7: Typical modulator performance of low speed modulator

On/Off ratio	bias Voltage	modulation Voltage	bandwidth	Q-value
9 - 13 dB	20 - 25 V	±2 V to ±4 V	0.6 Mbit/s	0.5 - 2

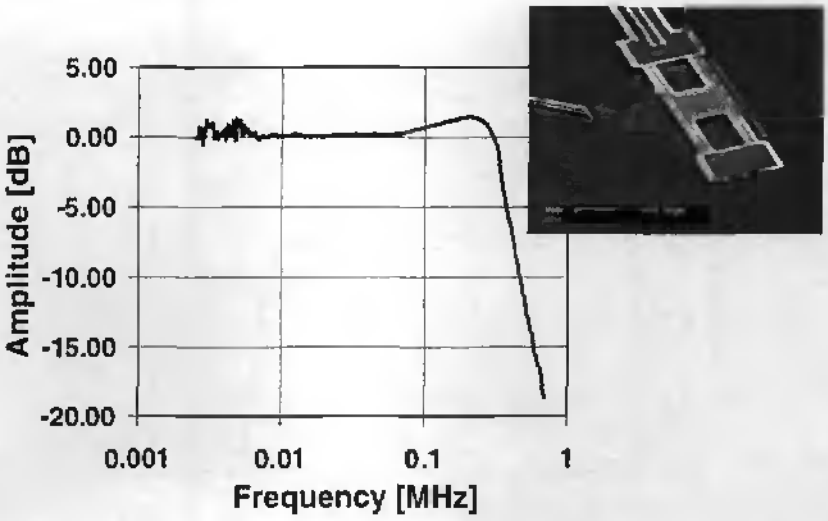

Figure 3.33: Dynamic response of a modulator with reduced speed. Venting holes in the membrane allow to adjust a critical damping.

3.5. Conclusions

In this chapter we have reported on the design, fabrication and characterisation of a reflective modulator for telecommunication applications. The micromechanical modulation principle presents the advantage of released packaging tolerances and inherent polarisation insensitivity. When the modulator is combined with a receiving photodiode a compact receiver-transmitter microsystem can be built which has a very low cost potential. Figure 3.34 shows a schematic view of such a transceiver. Based on the modulator developed in this thesis Ascom Tech has built a micromechanical receiver-transmitter microsystem and Figure 3.35 shows an example of a fully packaged device.

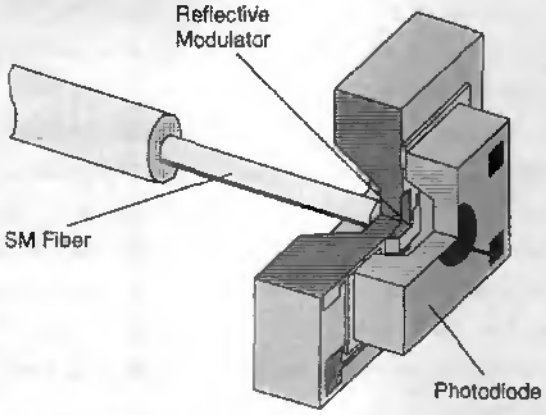

Figure 3.34: Modulator-receiver microsystem

In the first part of the chapter the choice of the Fabry-Perot modulation principle was motivated. Realized in the surface micromachining technology the electrostatic Fabry-Perot modulator offers the highest speed compared with other micromechanical solutions. Nevertheless the interference based modulation principle is inherently wavelength dependent. To circumvent this drawback torsion mirrors may be a good solution, but for low speed applications only.

In the second part of the chapter the optical and mechanical behaviour of the modulator was modelled and simulated in detail. With the combination of these simulations the electro-optic response of the modulator could be calculated taking

into account variations in the operation wavelength and possible errors in the layer thickness. Simulations were focused on high speed modulators with a bandwidth above 2 Mbit/s. For a perfect thickness of the mirror layers the extinction voltage, i.e. the voltage at which the minimum of reflectivity is reached, was simulated to be 75 V at a wavelength of 1350 nm. This value increases for shorter wavelength to become over 90 V at a wavelength of 1250 V. The modulation voltage, i.e. the voltage to modulate between 0% and 80% of reflectivity, has been simulated to be over 20 V at 1350 nm, whereas at 1275 nm already 8 V are sufficient. An unfortunate combination of errors in the mirror thickness can increase the wavelength dependence and reduce the On-Off contrast.

Another point of interest of the modelling chapter have been the speed limits of the micromechanical modulation principle. It has been shown, that the bandwidth is limited by air damping to 3 - 6 Mbit/s. For a higher frequency the damping becomes too weak and overshot ringing appears.

Than a short overview over the fabrication process is given. The fabrication is based on the well established polysilicon surface micromachining technique. Care has to be taken to ensure a good precision of the layer depositions. Typically a ± 5 % reproduceability was achieved. For the polysilicon mirrors this has been sufficient, but the sacrificial oxide should be defined within ± 2 %. Another difficulty of the fabrication arises from the back side hole, which is used to align the fiber and to bring it sufficiently close to the modulator. This hole has to be etched and aligned with a good precision.

The last part of the chapter deals with the characterisation. The insertion loss of packaged modules was below 3 dB, with typical loss values around 2 dB. The On-Off contrast is typically around 10 dB. A maximum modulation rate of Fabry-Perot modulators over 3 Mbit/s has been obtained. Although the modulator shows good optical performance, the electrical operation is not straightforward. To drive modulators at these high frequencies a bias voltage up to 100 V is necessary. The modulation voltage is between 5 V_{pp} up to 15 V_{pp}, depending on the wavelength. Also layer thickness variations can change the operation voltages. Therefore the modulator characteristics may change from one fabrication run to the other if the layer thickness cannot be exactly reproduced. To get a good modulation contrast over a wide wavelength range a feed-back control of the driver voltage is necessary.

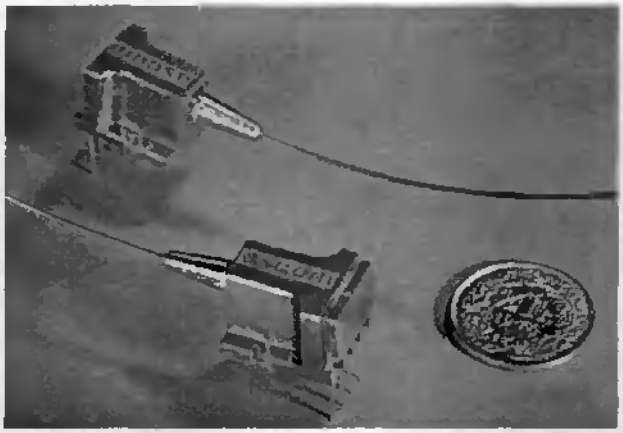

Figure 3.35: Packaged Modulator-Receiver module.

The high operation voltage and the need for a feed back control are drawbacks, which reduce the attractivity of the micromechanical modulator. On the other hand the reflective modulation principle has the inherent advantage of wavelength conservation, which is an important feature for wavelength division multiplexed *(WDM) systems.*

For various applications a bit rate of only a few hundred kbit/s is sufficient. We showed that for such modulators the operation voltage and therefore also the power consumption is considerably lower. In particular we have fabricated a 625 kbit/s device which needs a 25 V bias voltage and 4 Vpp modulation voltage.

[1] Micro Structure Bulletin, No. 3, Aug 1994

[2] L. Altwegg, A. Azizi, P. Vogel, Y. Wang and F. Wyler, "LOCNET: A fiber in the loop system with no light source at the subscriber end", *J. Light. Tech.*, vol. 12, pp. 535 - 540, (1994)

[3] P. J. Duthie, M. J. Wale,I. Bennion, and Hankey, "Bidirectional fiber-optic link using reflective modulation", *Electron. Lett.*, vol. 22 p. 517, 1986

[4] T. H. Wood, R. A. Linke, B. L. Kasper, and E. C. Carr, "Observation of coherent Rayleigh noise in single-source bidirectional optical fiber systems", *J. Light. Tech.*, vol. 6 p. 346 - 352, (1988)

[5] R. C. Alferness, "Waveguide Electrooptic Modulators", *IEEE Transactions on Microwave Theory and Techniques, vol. MTT-30*, no. 8, pp. 1121-1137 (1982)

[6] P. Buchmann, H. Kaufmann, H. Melchior, and G. Guekos, "Broadband Y-branch electrooptic GAAs waveguide interferometer for 1.3 μm", *Appl. Phys. Lett.*, vol. 46, pp. 462-464, 1985

[7] S. Y. Wang, S. H. Lin, and Y. M. Houng, "GaAs travelling wave electrooptic waveguide modulator with bandwidth > 20 GHz at 1.3 μm", *in Proc. OFC/IOOC Reno*, NV, 1987, p. 177.

[8] R. G. Walker, "High-Speed Electrooptic Modulation in GaAs/GaAlAs Waveguide Devices", *J. Light. Tech.*, vol. LT-5, no. 10, pp. 1444-1453, (1987)

[9] C. Linder, L. Paratte, M.-A. Gretillat, V. P. Jaecklin and N. F. de Rooij, "Surface micromachining", *J. Micromech. Microeng.*, vol.2 (1992), pp. 122-132

[10] Preston K Jr. "An array optical spatial phase modulator", in Proc. of the *IEEE International Solid State Circuits Conference* (Institute of Electrical and Electronics Engineers, New York, 1968), p. 100.

[11] J. A. van Raalte. "A new Schlieren light valve for television projection", *Appl. Opt.*, vol. 9 (1970), pp. 2225 - 2230

[12] K. E. Petersen, "Micromechanical light modulator array fabricated on silicon", *Applied Physics Letters*, Vol. 31, No. 8, 15 October 1977, pp 521 - 523

[13] M. A. Cadman, A. Perret, F. Porret, R. Vuilleumier, P. Weiss, "Novel electromechanical microshutter display using metallic films", *IEEE Electron. Dev. Lett.*, vol. 4 (1983), no. 1

[14] L. J. Hornbeck, "Deformable mirror spatial light modulators", in *Proc. Soc. Photo-Opt. Instrum. Eng.*, vol. 1150 (1989), pp. 86 - 102

[15] V. P. Jaecklin, C. Linder, N. F. de Rooij, J.-M. Moret, R. Vuilleumier, "Optical microshutters and torsional micromirrors for light modulator arrays", *Tech. Dig. IEEE Micro Electro Mech. Syst. Workshop*, Fort Lauderale, FL, USA, Frebruary 1993, pp. 124-127

[16] M. T. Ching, R. A. Brennen, R. M. White, "Microfabricated optical chopper", *Optical engineering*, Nov. 1994, vol. 33 No. 11, pp 3634-3642

[17] K. E. Mattson, "Surface micromachined scanning mirrors", *Microelectronic Engineering* 19 (1992) 199-204

[18] V. P. Jaecklin, *Surface Micromachined Electrostatic Actuators*, Doctoral Thesis, Faculty of Sciences, University of Neuchâtel, 1994, pp. 96 - 99

[19] G. W. Goosen, J. A. Walker, S. C. Arney. "Silicon modulator based on mechanically-active anti-reflection layer for fiber-in-the-loop applications". *Proceedings of the Optical Fiber Communications Conference '94*; pp. 50-53

[20] R. B. Apte, F. S. A. Sandejas, W. C. Banyai, and D. M. Bloom. "Deformable grating light valves for high resolution displays". *Proc. Solid state sensor and actuator workshop*, (Hilton Head Island, South Carolina, june 13 - 16, 1994) pp. 1 - 6

[21] J. A. Walker, K. W. Goosen and S. C. Arney, "Fabrication of Mechanical Antireflection Switch for Fiber-to-the-Home Systems", *J. of MicroElectroMechanical Systems*, Vol. 5, No. 1, March 1996

[22] K. Aratani, P. J. French, P. M. Sarro, R. F. Wolffenbuttel and Middelhoek. Digest of Techn. Papers, *The 7th Int. Conf. Solid-State Sensors and Actuators, Transducers '93* (Yokohama, Japan, June 7 - 10, 1993) pp 678 - 681

[23] W R Wiszniewski, R E Collins, and B E Pailthorpe., *Proc. of The 7th Int. Conf. Solid-State Sensors and Actuators, Transducers '93* (Yokohama, Japan, June 7 - 10, 1993) pp 1027 - 1030

[24] V. P. Jaecklin, *Surface Micromachined Electrostatic Actuators*, Doctoral Thesis, Faculty of Sciences, University of Neuchâtel, 1994

[25] C. Marxer, M.-A. Gretillat, V. P. Jaecklin, R. Baettig, O. Anthamatten, P. Vogel and N. F. de Rooij, "Megahertz Opto-Mechanical Modulator", *Sensors and Actuators A 52* (1996) pp. 46-50

[26] Macleod, *Thin Film Optical Filters*, Adam Hilger Ltd, Bristol 1986, Chapter 2

[27] D. E. Aspnes, "Optical functions of intrinsic Si: Table of refractive index, extinction coefficient and absorption coefficient vs Energy (0 to 400 EV)", in *Properties of Silicon*, London: Inspec, The institution of electrical engineers, pp. 72-78, (1988)

[28] O. Anthamatten, R. K. Bättig, B.Valk, P.Vogel, C. Marxer, M.-A. Grétillat and N.F. de Rooij, "Packaging of a reflective optical duplexer based on silicon micromechanics", *Proc. of the IEEE/LEOS Summer Topical Meetings, Optical MEMS and their Applications*, Keystone, Colorado, 1996

[29] R. Legtenberg, H.A.C Tilmans., "Electrostatically driven vacuum-encapsulated polysilicon resonators, Part II, - Theory and performance", *Sensors and Actuators A, 44* (1994), pp. 67 -

[30] H. C. Nathanson, W. E. Newell, R. A. Wickstrom, J. R. Davis Jr., "The Resonant Gate Transistor", *IEEE Trans. Electron. Devices* ED-14 (1967) pp. 117-133

[31] P. Osterberg, H. Yie, X. Cai, J. White and S. Senturia, "Self-cosistent simulation and modeling of electrostatically deformed diaphragms", *Proceedings of IEEE Micro Electro Mechanical Systems*, 1994, Japan, pp. 28 - 32

[32] R. J. Roak and W.C. Young, *Formulas for Stress and Strain*, 5th ed., McGraw-Hill International Edition, Singapore, 1976

[33] C. Linder, *Electromechanical Polysilicon Structures and Micromechinig Processes for Sensor and Actuator Applications*, Doctoral Thesis, Faculty of Sciences, University of Neuchâtel, 1993

[34] S. Timoshenko, D.H. Young and W. Weaver, *Vibration Problems in Engineering*, 4th ed., Wiley, New York, 1974, Ch.5.

[35] H. Guckel, D.W. Burns, H.A.C. Tilmans, D.W. DeRoo and C.R. Rutigliano, "Mechanical Properties of fine grained polysilicon the repeatability issue", *Tech. Dig. IEEE Solid-State Sensor and Actuator Workshop*, Hilton Head Island, SC, June 1988, pp. 55-58

[36] L. Lin, R. T. Howe, A. P. Pisano, "A Passive, In Situ Micro Strain Gauge", *Tech. Dig. IEEE Solid-State Sensor and Actuator Workshop*, Hilton Head Island, SC, 1993, pp. 201 - 206

[37] T B Gabrielson, "Mechanical-Thermal Noise in Micromachined Acoustic and Vibration Sensors", *IEEE Transactions on Electron Devices*, Vol. 40, No. 5, May 1993.

[38] Y. J. Yang, S. D. Senturia, "Numerical Simulation of Compressible squeezed-film Damping", *Solid-State Sensor and Actuator Workshop Hilton Head*, South-Carolina, June 2-6, 1996, pp. 76 - 79

[39] R. K. Gupta, E. S. Hung, Y. J. Yang, G. K. Anathasuresh and S. D. Senturia, "Pull-in Dynamics of Electrostatically Actuated Beams", *Solid-State Sensor and Actuator Workshop Hilton Head*, South-Carolina, June 2-6, 1996

[40] C. L. Chen and J. J. Yao, "Damping control of mems devices using structural design approach", *Solid-State Sensor and Actuator Workshop Hilton Head*, South-Carolina, June 2-6, 1996, pp. 72-75

[41] J. J .Blech, "On Isothermal Squeeze Films", *J. of Lubrification Techn.*, Vol. 105, 1983, pp. 615-620.

[42] M Biebl, G T Mulhern, R T Howe, "In Situ Phosphorus-Doped Polysilicon for Integrated MEMS", *Proceedings of the 8th International Conference on Solid-State Sensors and Actuators and Eurosensors IX*, Stockholm, Sweden June 25-29, 1995 (Transducers '96), pp. 198-201

[43] Ristic Ljubisa, editor, *Sensor Technology and Devices*, Artech House, Norwood MA, 1994

[44] P. J. French, "Development of surface micromachinig techniques compatible with on-chip electronics", *J. Micromech. Microeng.* 6 (1996) pp. 197-211.

[45] C. Linder, L. Paratte, M.-A. Grétillat, V. P. Jaecklin and N. F. de Rooji, "Surface micromachining", in *J. Micromech. Microeng. 2 (1992), pp. 122-132*

[46] R. A. Levy and K. Nassau, "Viscous Behaviour of Phosphosilicate and Borophosphosilicate Glasses in VLSI Processing", *Solid State Technology*, 1986, p. 123

[47] M. W. Puty, S Chang, R. T. Howe, A. L. Robinson, and K. D. Wise, "Process Integration for active Polysilicon Microstructures", *Sensors and Actuators*, Vol. 20, 1989, p.143

[48] G. C. Johnson, P. Krulevitch, D. Mirfendereski and A. D. Kiureghian, "Effects of Processing on the Behaviour of thin film Materials for Micromechanical Systems", Office of Industrial Science and Technology Frontier Program, AIST, MITI, *IARP proceedings of the Workshop on Micromachine Technologies and Systems*, 26 - 28 October 1993, Tokyo

[49] M Biebl, G T Mulhern, R T Howe, "In Situ Phosphorus-Doped Polysilicon for Integrated MEMS", *Proceedings of the 8th International Conference on Solid-State Sensors and Actuators and Eurosensors IX*, Stockholm, Sweden June 25-29, 1995 (Transducers '96), pp. 198-201

[50] L.S. Fan and R.S. Muller, "As deposited Low strain LPCVD Polysilicon", *Tech. Digest, IEEE Solid State Sensor and Actuator Workshop*, Hilton Head Island, SC, 1988, p. 55

[51] H. Guckel and D.W. Burns, "Measurement and control of Mechanical Properties of thin films", *IV International Workshop on the Physics of Semiconductor Devices*, Madras, India, 1987

[52] H. Guckel, D.W. Burns, C.C.G. Visser, H.A.C. Tilmans and D. Deroo, "Fine Grained Polysilicon Films with built in tensile Stain", *IEEE Trans. Electron Dev.*, Vol. ED-35, No.6, 1988, p. 800.

[53] T. I. Kamins, M. M. Mandurah and K.C. Saraswat, "Structure and stability of low pressure chemically vapor deposited silicon films", *J. Electrochem. Soc.*, Vol. 125, No.6, 1978, p. 927

[54] G. Harbeke, L. Krausbauer, E.F. Steigmeier, A. E. Widmer, H. F. Kappert and G. Neugebauer, "Growth and Physical properties of LPCVD Polycrystalline Silicon Films", *J. Electrochem. Soc.*, Vol. 131, No. 3, 1984, p. 675.

[55] P. Krulevitch, G.C. Johnson and R.T. Howe, "Stress and Microstructure in Phosphurus Doped Polycrystalline Silicon", *Mat. Res. Soc. Symp. Proc.*, Vol 276, 1992.

[56] A. T. Voutsas and M. K. Hatalis, "Structure of As-Deposited LPCVD Silicon Films at Low Deposition Temperatures and Pressures", *J. Electrochem. Soc.*, Vol 139, No. 9, 1992, p. 2659.

[57] J. Adamczewska and T. Budzynski, "Stress in Chemically Vapor Deposited Silicon Films", *Thin Solid Films*, Vol. 113, 1984, p. 271.

[58] P. J. French, van Dreënhuitzen, D. Poenar, J. F. L. Goosen, R. Mallée, P. M. Sarro, R. F. Wolffenbuttel, "The Development of a low stress Polysilicon Process Compatible with Standart Device Processing", *J. of Microelectromechanical Systems*, Vol. 5, No. 3, September 1996, pp. 167 - 196

[59] C. Linder, N. F. de.Rooij, "Investigations on Free Standing Polysilicon Beams in View of Their Application as Transducers", *Sensors and Actuators A*, Vol. A21-A23, 1990, p. 1053.

[60] T. A. Lober and R. T. Howe, "Surface Micromachinig Processes for Electrostatic Microactuator Fabrication", IEEE Solid state sensor and actuator workshop, Hilton Head, 1988, pp. 59-62

[61] S. Marco, O. Ruiz, J. Samitier, J. R. Morante and J. Bausells, "Relation between electrical conductivity and structural characteristics in boron-doped LPCVD polycrystalline silicon used in sensor devices", *Sensors and Actuators A*, 37-38 (1993) pp. 68-73

[62] D. Maier-Schneider, A. Ersoy, J. Maibach, D. Schneider and E. Obermeier, "Influence of Annealing on Elastic Properties of LPCVD Silicon Nitride and LPCVD Polysilicon, Sensors and Materials, Vol. 7, No. 2 (1995), pp. 121-129

[63] Balzers AG, Liechtenstein, Product Information, Materiaux d'évaporation

[64] P. R. Scheepers, J. A. Voorthuyzen, W. Othius and P. Bergveit, " Investigation of attractive forces between PECVD silicon nitride microstructures and an oxidized silicon substrate", *Sensors and Actuators A30*, 1992, pp. 231

[65] Y. Yee, K. Chun, J. D. Lee, "Polysilicon Surface Modification Technique to reduce Sticking of Microstructures", *Proc. of the 8th International Conference on Solid-State Sensors and Actuators and Eurosensors IX (Transducers '95)*, Stockholm, June 25 - 29, 1995, p.206-209

[66] M. R. Houston, R. Maboudian and R. T. Howe, "Self-Assembled Monolayer Films as Durable Anti-Stiction Coatings for Polysilicon Microstructures", *Solid-State Sensor and Actuator Workshop*, Hilton Head SC, June 2-6, 1996, pp. 42-47

[67] G. T. Multhem, D. S. Soane, R. T. Howe, "Supercritical carbon dioxide drying of microstructures", Proc. 7th Int. Conf. On Solid State Sensors and Actuators (Transducers '93), Yokahama 93, pp. 296-299

[68] H. Guckel, J. J. Sniegowski, T. R. Christenson, S. Mohney and T. F. Kelly, "Fabrication of micromechanical devices from polysilicon films with smooth surfaces", *Sensors and Actuators* 20, (1989), pp. 117-120.

[69] R. Legtenberg, *Electrostatic actuators fabriceted by surface micromachining techniques*, PhD Thesis, 1996, University of Twente

[70] H. Guckel, J. J. Sniegowski and T. R. Christenson, "Advances in Processing Techniques for Silicon Micromechanical Devices with Smooth Surfaces", *Proceedings of the IEEE Workshop on MicroElectroMechanicalSystems*,1989, pp. 71-75

[71] A. A. Yassen, S. W. Smith, M. Mehregany and F.L. Merat, "Diffraction Grating Scanners Using Polysilicon Micromotors", *Proceedings of the IEEE Workshop on Micro Electro Mechanical Systems* 1995, Amsterdam, NL, pp. 175-180

[72] G. Findler, J. Muchow, M. Koch and H. Münzel, "Temporal Evolution of silicon surface roughness during anisotropic etching processes", *Proc. IEEE workshop on Micro Electro Mechanical Systems*, Travemünde (Germany), February 4 -7, 1992

[73] E. D. Palik, O. J. Glembocki, I. Heard, P. S. Burno and L. Tenerz, "Etching roughness for (100) silicon sorfaces in aqueous KOH", *J. Appl. Phys.* 70 (6), 15 September 1991

[74] Y. Uenishi, M. Tsugai and M. Mehregany, "Micro-opto-mechanical devices fabricated by anisotropic etching of (110) silicon", *J. Micromech. Microeng.* 5 (1995) 305-312

[75] E. Peeters, *Process devevelopment for 3D Silicon Microstructures with Application to Mechenical Sensor Devices*, PhD Thesis, March 1994, Katholieke Universiteit Leuven, Chapter 2

[76] T. A. Kwa and R.F. Wolffenbuttel, "Effect of Solution Contamination on Etched Silicon Surfaces", Proceedingds of Micro Mechanics Europe (MME '94), 1994, Pisa Italy, pp. 36 - 39

[77] T. A. Kwa, P. M. Sarro, W. van der Vlist, P. J. French and R. F. Wolffenbuttel, "Fabrication of extremely smooth mirror surfaces in silicon for application in an integrated spectrometer", *Proceedings of the 7th International Conference on Solid-State Sensors and Actuators, (Transducers '93)*, Yokahama, pp. 242-245

[78] Schnakenberg et al; *Sensors and Actuators A*, 25-27,(1991), 1-7

[79] S. A. Cambell, K. Cooper, Dixon, R. Earwaker, S. N. Port and D. J. Schiffrin, "Inhibition of pyramid formation in the etching of Si p<100> in aqueous potassium hydroxide-isooropanol", *J. Micromech. Microeng.* 5 (1995) 209-218

[80] private communication Dr. H. Hunziker, Institute of Quantum Electronics, ETH, Zürich

[81] X. G. Zhang, S. D. Collins and R. L. Smith, "Porous Silicon Formation and Electropolishing of Silicon by Anodic Polarization in HF Solution", *J. Electrochem. Soc.*, Vol. 136, No. 5, May 1989

Chapter Four

Fiber Optic Switch

4.1. Introduction

4.1.1. Fiber Optic Switching

Switching of light from one input fiber in either of two output fibers is becoming increasingly important to allow reconfiguration of fiber optic networks down at the optical level. Especially for network reliability there is a growing interest for low-speed, polarisation and wavelength insensitive switches. For many applications the speed of the switch itself can be in the range of a millisecond, which is accessible for micromechanical devices.

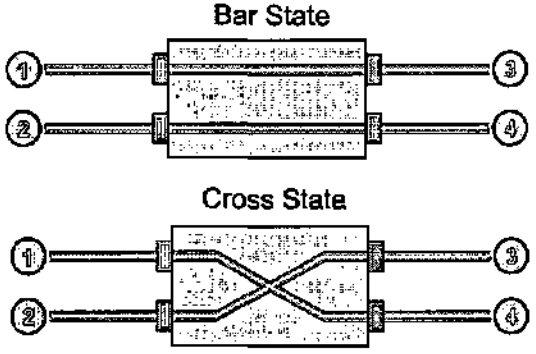

Figure 4.1: Functional principle of an optical 2x2 switch. Light from input fiber 1 can be directed into output fiber 3 or 4.

Figure 4.1 shows the functional principle of a 2x2 switch. In the bar state the light from input fiber 1 respectively 2 is coupled to output 3 and 4 respectively. In the cross state the light from input 1 is redirected to output 4, and the light from input 2 is redirected to output 3.

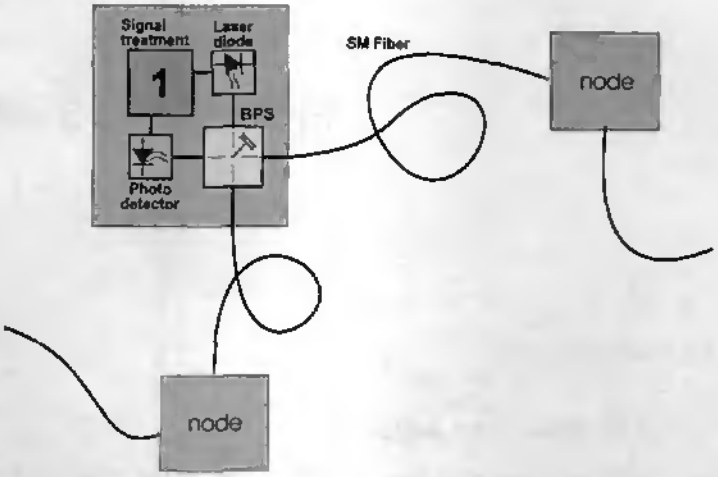

Figure 4.2: Schematic view of a network ring configuration with a By-Pass-Switch, which allows to operate the ring also with a node out of service.

Figure 4.2 shows a possible use of a 2x2 switch as a "by-pass-switch" in an fiber optic network ring in order to increase its reliability. Every network node receives an optical data stream which is converted into electrical data in the photodetector. The data processing of the node transmits the data which are destined to other nodes, i.e. the electrical data is again converted into an optical signal in the laser diode. If this network node now shuts down, for example because of a power shortage or because of maintenance work, the network node has to be by-passed, to allow the network ring to continue operations. The optical data are transmitted to the next node passively without processing and amplification. To do this the by-pass-switch commutes into its cross state and the data stream no more enters into the node but is directly reflected into the output fiber and passively transmitted to the next node.

A wide variety of principles have been proposed for fiber optic switches. They can be grouped in two families based either on optical effects in waveguides, or on the mechanical movement of a mirror or the fiber itself.

Optical waveguides can be integrated on many different substrates, such as plastic, silicon, III-V materials and LiNbO3. In GaAs[1] and LiNbO3[2] the electro-optic effect can be exploited for the construction of switches and hole switch matrixes[3]. In silicon[4] and InGaAsP/InP[5] the carrier induced refractive index change is an effect that can be used for waveguide based switches. Electro-optic and carrier-induced-refraction-index-change switches allow a very high switching speed over 1 GHz. Their operation principle is either interferometric or mode sorting. All the same for network reconfiguration and reliability there is a considerable interest in low cost switches with a switching speed of around one millisecond. For such medium speed applications the waveguide based thermo-optic switch has been proposed, which has the advantage of a more versatile operating principle. It is based on a so called adiabatic waveguide crossing[6], i.e. a mode sorting switch, where switching occurs when one branch of a crossed waveguide structure is heated. The waveguide itself can be made of various materials. Low cost approaches are based on polymer waveguides[7,8,9] or silica layers[10], both can be deposited and structured on silicon.

But also mechanical switches allow a switching speed in the range of a few milliseconds. In addition to their availability they show good optical performance, i.e. low loss and high isolation. Most currently available mechanical switches are fabricated using conventional machining. These switches are built up out of macro-mechanical parts and are based on the mechanical displacement of fibers[11,12,13] moveable waveguide structures[14], a thin movable mirror[15] or the rotation of a mirror[16].

Others have built up switches using conventional modulators based for example on the liquid crystal technology[17].

4.1.2. Micromechanical Fiber-Optic Switches

In order to reduce fabrication costs and to increase switching speed, silicon micromachining techniques have been explored to fabricate mechanical fiber optic switches. Inspired from the conventional mechanical switches micromechanical

devices were developed, where the fibers are moved with a thermal actuator[18] or with electrostatic actuation of metallized fibers[19,20]. In such a switch the fiber has to be deformed at least 125 µm, which corresponds to the fiber diameter. For integrated actuators 125 µm presents a too large distance to be practical. Therefore it has been proposed to combine the silicon micromachined motherboard with conventional magnetic actuation[21],[22]. To reduce the necessary fiber deformation *Olfier et al.* have used integrated optical waveguides, which are bent by an electrostatic actuator[23].

As shown in Figure 4.3 another way to achieve fiber optic switching is to use micromirrors. Light is no more coupled directly between the mobile waveguides, but the switching is achieved by a mobile mirror and the waveguides remain fixed. In the first configuration the micromirror is brought into the optical path by a linear displacement[24],[25] or by a 90° out of plane rotation[26] of the mirror. Thus in the bar state the mirror is outside of the optical path. In the second configuration the light is always reflected by the mirror but can be redirected in different fibers by a rotation of the mirror[27].

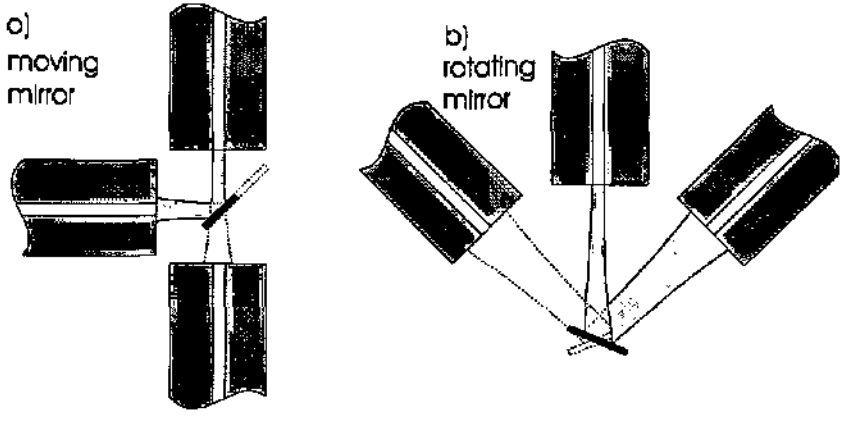

Figure 4.3: Micro-Mechanical principles for fiber-optic switches.

4.1.3. 2x2 Switch Based on Plasma Etched Vertical Mirror

Our switch is based on the mechanical movement of a vertical silicon mirror which can be moved into the optical path between two pairs of single mode fibers. Figure

4.4 shows a top view of the switch in bar and cross position. In order to minimise coupling loss the fibers have a tappered end, so that they can be put closer together. In the bar state light from fiber 1 is coupled into fiber 3 and light from fiber 2 into fiber 4. In the bar position the vertical mirror reflects the light from fiber 1 by an angle of 90 ° into fiber 4. Light from fiber 2 is reflected into fiber 3.

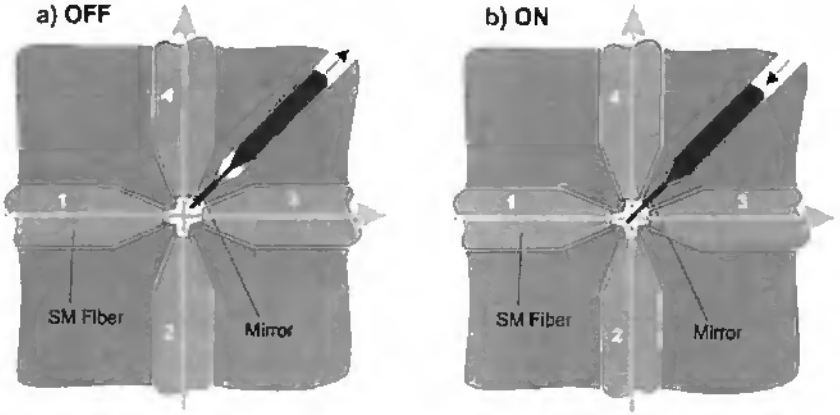

Figure 4.4: Top view of 2x2 switch in a) bar and b) cross state.

The integration on silicon of vertical mirrors with optical quality is a challenging task. Several fabrication techniques have been explored. It has been proposed to use KOH etching of <110> silicon to fabricate vertical mirrors[28]. Others worked with controlled underetching of (100) planes in <100> wafers[29,30]. These mirrors have to be aligned with the crystal directions, which limits the geometrical freedom to define other mechanical structures like suspensions and actuators in the same etching step. With these mirrors only very simple actuator functions and passive elements like splitters, attenuators and couplers have been realized.

More sophisticated mirror structures can be fabricated by using thick film photolithography and electroplating. In Reference[31] a vertical mirror-actuator structure was fabricated by standard UV light lithography of thick photoresist and subsequent electroplating. The movable mirror was used to tune a laser diode[32]. The LIGA technique, a x-ray based lithography with galvanic filling of the mold, can produce more vertical and higher electroplated structures than with UV-light based thick film photolithography. In Reference[25],[33] a 2x2 switch is presented, which is

similar to our design. The vertical moving mirror is fabricated by the LIGA technique. To reduce coupling loss the design uses ball lenses, which have to be assembled individually[34].

Another technique for fabricating high aspect ratio vertical mirrors is based on conventional polysilicon micromachining. The vertical mirrors are fabricated by rotating hinged polysilicon structures out of plane[35]. It has been shown, that these mirrors can be integrated together with lenses[36], sensor and actuator structures[37,38] to form micro-optical benches on a chip. A potential application of such a micromachined optical bench has been demonstrated in Reference[39] as a bar-code reader.

In our design no postprocessing or assembly of other parts than the fibers is necessary: The fabrication of the vertical mirror is based on the new possibilities of deep anisotropic reactive ion etching[40,41] to fabricate the mirror together with the suspension, actuation and fiber-alignment structures in one processing step.

Figure 4.5 shows a schematic view of the vertical mirror switch. The switch is composed of a small beam etched out of silicon which forms the vertical mirror.

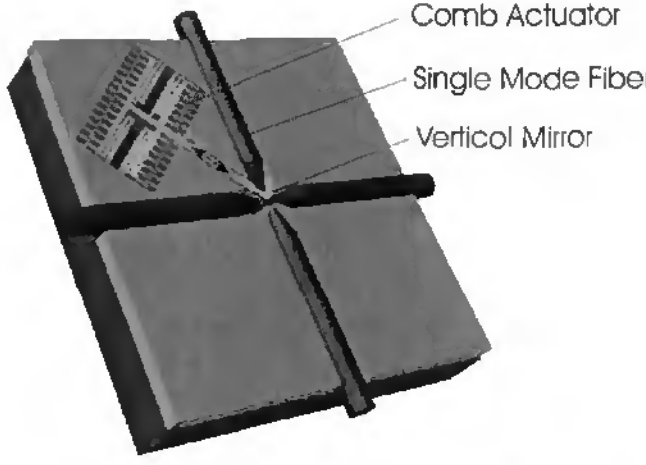

Figure 4.5: Schematic view of the micromechancial switch. It consists of a metallized vertical silicon mirror which can be moved by electrostatic comb actuators into the optical path between two pairs of fibers.

The mirror structure is suspended by folded spring suspensions, which have a high compliance in the direction parallel to the mirror plane. In all other directions the suspensions should be as stiff as possible to suppress parasitic mirror displacements and undesired vibrations or even instabilities. The mirror can be actuated by so called comb drive actuators[42],[43]. They work with electrostatic forces. The spot diameter of the light beam is about 10 µm. The mirror moves in a 45° angle to the light path, thus the minimum mirror displacement is $\sqrt{2}$ * 10 µm = 14.1 µm. In order to account for positioning tolerances and to prevent light diffraction at the mirror edge, the minimum displacement should be 20 µm. In the push-pull configuration shown in Figure 4.5 one of each comb actuator has to generate a 10 µm displacement.

4.2. Design Considerations

4.2.1. Optical Design Considerations

4.2.1.1. Metal coated silicon mirror

In order to increase the reflectivity of the vertical silicon mirror, it has to be metal coated. Figure 4.6 shows a schematic arrangement of the vertical mirror in between the two pairs of optical fibers. In order to minimize the light loss the mirror should have a maximum reflectivity and a minimum thickness.

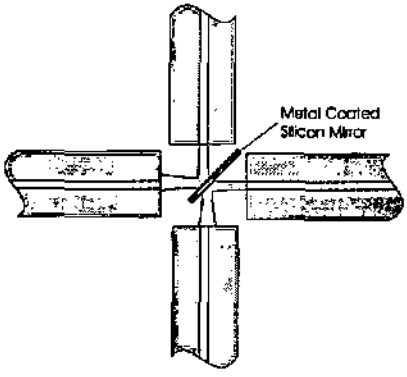

Figure 4.6: Reflection on a metal coated silicon mirror for the fiber optic switch application.

The reflectivity of the metal coated silicon increases with increasing film thickness but saturates to the reflectivity value of the bulk metal when the film gets sufficiently thick[44]. Using standard thin film interference theory[45] and tabulated values for the complex refractive index[46] we have calculated the reflectivity of various metals on silicon substrates at a working wavelength of 1.3 µm. Figure 4.7a) shows the reflectivity as a function of layer thickness at normal incidence. It can be seen, that an aluminium coated mirror reaches its maximum reflectivity of 97 % at a film thickness of 40 nm already. Gold films also result in a good reflectivity of 97.5 % at a layer thickness of only 60 nm. Other current micromachining materials like nickel and chrome have smaller reflectivities of only 72 % and 63 % respectively. A good reflectivity alone is not sufficient for a good mirror in a switch application. Also the light transmission should be attenuated below 1 ppm in order to get a channel insulation over 60 dB. For aluminium coated mirrors the light transmission falls below 1 ppm when the aluminium film has a thickness above 100 nm. For gold coatings a minimum layer of 170 nm is necessary and for nickel and chrome coatings the thickness should even be over 270 nm and 320 nm respectively.

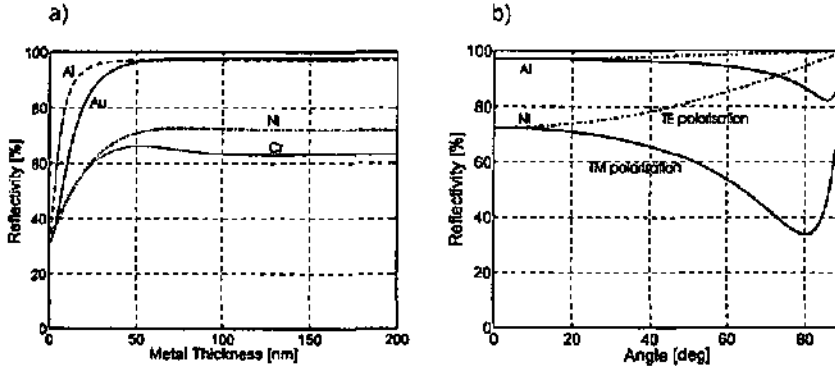

Figure 4.7: Simulated reflectivity (λ = 1300 nm) of a metal coated silicon surface as a function of a) metal thickness (at normal incidence) and b) incidence angle (for layer thickness 120 nm).

Similar to dielectrics the reflectivity of metallic surfaces becomes polarisation dependent for non-normal incidence angles. This polarisation sensitivity depends on the metal and on the incidence angle. Figure 4.7 b) shows the polarisation

dependence as a function of the incidence angle for aluminium and nickel mirrors. At a 45° incidence angle the high reflectivity aluminium mirror has a polarisation dependence of only 1.1 %, whereas the nickel mirror with the lower reflectivity also manifests a more pronounced polarisation dependence of 11 %. Results of above calculations are summarised in Table 4.1.

Table 4.1: Simulated thin film mirror characteristics at a wavelength of 1300 nm.

	Gold	Alu	Nickel	Chrom
refractive index[46]	0.4+8.3i	1.3+13i	2.9+5.1i	4.53+4.3i
reflectivity	97.5 %	97 %	72.1 %	63 %
min. thickness for transm. < 1 ppm	170 nm	100 nm	270 nm	320 nm
pol. sens. at 45°	0.9 %	1.1 %	11.4%	16%

4.2.1.2. Effect of surface roughness

When light illuminates a rough surface the reflected beam no longer remains straight but fractions of the light are scattered in different directions. This property has been used to measure the surface quality of optical components and mechanical parts as well. For optical surfaces even a small degree of roughness produces measurable light scattering. The theoretical description of scattered light on a gently sloped surface is possible with the Kirchhoff formalism[47], where the scattered field is given by the phase integral over the illuminated region. It can be shown, that the angular distribution of the reflected light is proportional to the power spectral density of the surface height as long as the rms roughness stays below 5 % of the wavelength[48]. In our application we are only interested in the total amount of scattered light. In the case of a gently sloped surface with a Gaussian distribution of the surface height the amount of scattered light can be estimated from the *rms* surface roughness σ using the relationship[49]:

$$\frac{P_{scat}}{P_{tot}} = 1 - e^{-\left(\frac{4\pi\sigma\cos\theta_i}{\lambda}\right)^2} \qquad (4.1)$$

,where P_{scat} is the flux of light scattered away from the specular direction, P_{tot} is the total reflected flux. θ_i is the incidence angle and λ is the wavelength of the light. Using this formula the amount of scattered light is calculated for different rms surface roughness and resumed in Table 4.2. The light loss due to scattering remains below 10 % as long as the rms surface roughness is smaller than 47 nm or 3.6 % of the wavelength.

Table 4.2: Calculated amount of scattered light at λ=1300 nm and an incidence angle of 45 °.

σ	5 nm	10 nm	25 nm	50 nm	100 nm
P_{scat}/P_{tot}	0. 12%	0.47 %	2.9 %	11 %	37 %

4.2.1.3. Effect of mirror verticality on coupling loss

An important characteristic of fiber optic devices is their insertion loss, i.e. the efficiency of the light connection. For a longitudinal separation of 50 µm between two single mode fibers the theoretical coupling loss due to the Fresnel reflection at the fiber ends and and due to beam divergence stays below 1 dB (at a wavelength of 1.3 µm) even without a lensed fiber end. Thus the light coupling between single mode fibers can be very efficient as long as there is no transversal and no angular offset and as long as the distance between the fiber ends can be kept below 50 µm. All the same the diameter of single mode fibers is standardised to be 125 µm. To bring more than two fibers closer together than their cladding diameter the fiber end can be machined down to the core diameter.

When the light beam is not coupled directly between two fibers but reflected in between on a mirror, an additional coupling loss is introduced because of this mirror. First the mirror has a non zero thickness which results in a transverse offset of the beam. In addition the verticality of the mirror is not exactly 90° and an angle error is also introduced. Light coupling between single mode fibers is quite sensitive to angular (tilt) and transverse offset alignment errors. The loss due to these two imperfections is estimated with the coupling theory of Gaussian beams[50]. In Figure 4.8 the coupling loss between two fibers is plotted, when the beam is reflected by 90° on a mirror placed in the middle between the two fibers. The coupling efficiency

is plotted as a function of the verticality error of the mirror and for different mirror thickness which result in a transverse offset. The distance between the fiber ends is assumed to be 50 μm.

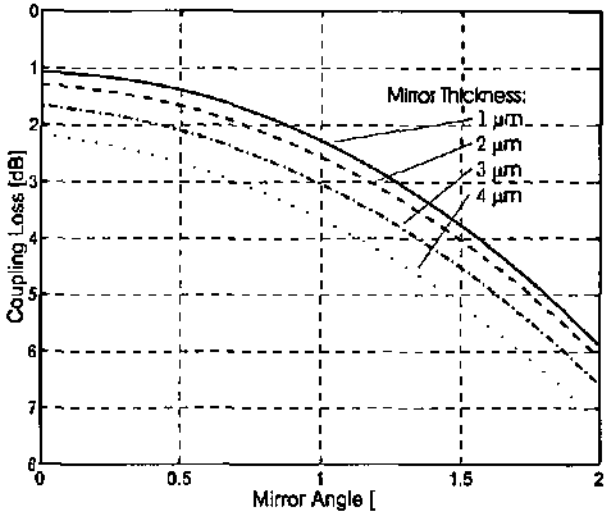

Figure 4.8: Coupling loss as a function of mirror verticallity at different mirror thickness. Longitudinal fiber seperation is 50 μm.

It can be seen from Figure 4.8, that to keep losses below 2 dB the mirror thickness should be smaller than 3.5 μm for a verticality of 90°. For an angle error of 0.7° the mirror thickness should be as low as 2 μm to obtain a coupling loss still below 2 dB.

4.2.2. Electro-Mechanical Design Considerations

4.2.2.1. Comb actuator

The vertical mirror is driven by a so-called electrostatic comb-drive actuator[42],[43], which is schematically described in Figure 4.9.

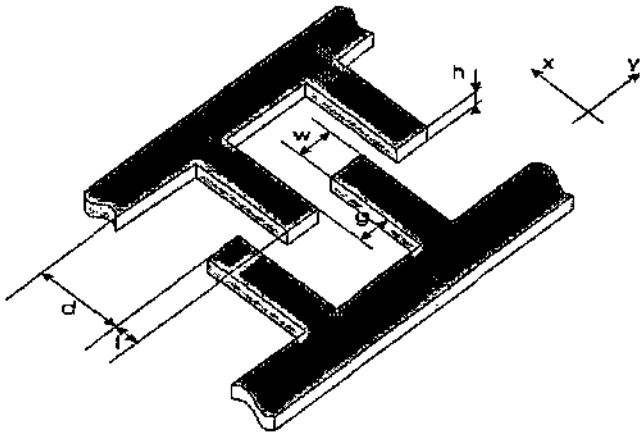

Figure 4.9: Comb-drive-actuator

The two comb structures are electrically insulated, one of them is fixed, whereas the other is mechanically connected to the suspension spring and the mirror structure. The second comb structure is thus moveable. When the comb structure is moved the capacitance is increased according to equation (4.2).

$$C = 2n\varepsilon\left(\frac{w \cdot h}{d - x} + \frac{(l + x)h}{g}\right) \qquad (4.2)$$

C is the capacitance formed by the comb structure, assuming a homogenous electrostatic field, n is the number of comb fingers of one side of the actuator, w is the width of the fingers, d is the distance between the finger tip of one comb and the comb base of the other comb, x is the comb displacement, l is the overlapping of the comb at zero displacement, h is the comb height and g is the gap between the comb finger as shown in Figure 4.9. The first term of above equation expresses the capacitance between the finger tips whereas the second term is the capacitance between the finger sidewalls.

When a voltage is applied between the two comb electrodes, a force is generated which equals:

$$F_x = \frac{1}{2}\frac{dC}{dx}V^2 \qquad (4.3)$$

according to equation (4.2), F_x becomes:

$$F_x = n\varepsilon V^2\left(\frac{wh}{(d-x)^2}+\frac{h}{g}\right) \qquad (4.4)$$

The first term of this equation expresses the force generated by the parallel plate capacitors of the finger tips, it increases with a quadratic term in the denominator. When x becomes close to d, i.e. when the finger tip gets close to the comb base, this term diverges. As shown for the reflecting modulator this term can lead to a pull-in behaviour. To prevent the comb-electrodes to touch each other mechanical stoppers are integrated, which limit the maximum displacement. The second term arises from the finger side-walls; it is a constant and doesn't depend on the displacement x. For small displacements the force due to the sidewall capacitor is much larger than the force from the finger tips. If the finger width w is assumed to be similar to the gap width g, then the first term is small as long as the distance (d - x) is larger than the gap g. Pull-in occurs when the first term which is non-linear with displacement x gets much larger than the second term, i.e when the distance (d - x) is smaller than the gap g, for a finger width w similar to the gap g.

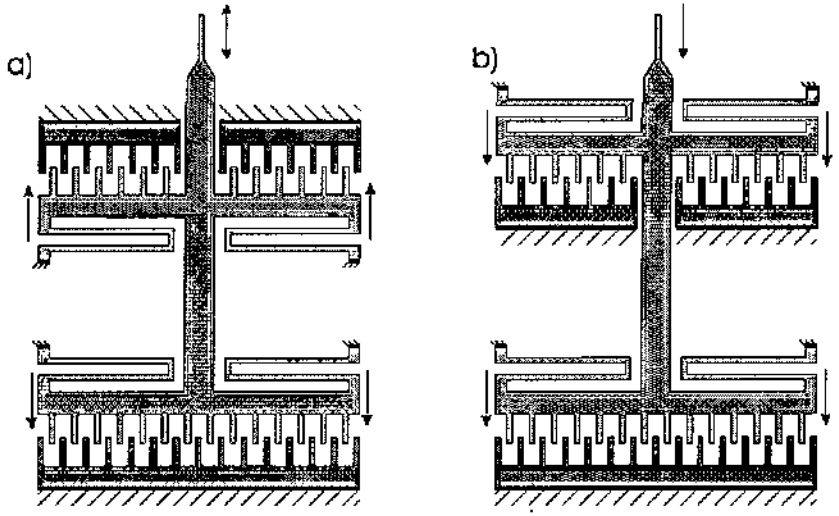

Figure 4.10: Tha comb can be arranged a) in a push-pull or b) in a ona way configuration.

As schematically shown in Figure 4.10 the comb actuator, which has to move the mirror, can be arranged in either a push-pull configuration or simply in a one way configuration. In the push-pull configuration the mirror can be moved forwards and backwards. This allows to have shorter comb fingers. The pull-in behaviour can be exploited to obtain a reduced driving voltage. Also during switching the mirror passes from one actuated position into the other, where the same amount of energy is stored in the suspension springs. The overshoot ringing is suppressed by the stopper electrodes. In addition the switching speed is considerably increased, because both the restoring spring force and the electrostatic actuation push the mirror. A drawback of this push-pull design is that the switch needs to be powered in either of its bar or cross state, i.e. when power is turned off the mirror is in a intermediate position. This can't be accepted for a by-pass switch, which has to spring into a well defined state when power shuts down. For these applications only the one-way configuration is useful.

The electrostatic force is counterbalanced by a spring force of the form:

$$F_x = k_x x \qquad (4.5)$$

The suspension spring is formed by thin etched beams, which have two beams in parallel to increase to spring constant in the transverse direction.

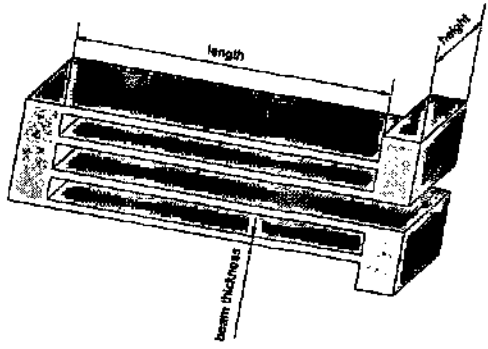

Figure 4.11: Spring meander with high stiffness in the transverse direction.

The spring constant in *x*-direction can be calculated with elastic beam theory. A double beam with both ends guided as shown in Figure 4.11 has a spring constant of[51]:

$$k_x = \frac{t2EI}{l^3} \qquad (4.6)$$

where *I* is the moment of inertia of the cross section, *l* the length and *E* the Young's modulus. Single crystal silicon is an anisotropic elastic crystal. The Youngs modulus depends on the crystal direction and can vary between 150 and 194 GPa. To simplify we assumed a isotropic Young's modulus of 170 GPa. In the actual design the mirror-actuator structure is suspended by four of above springs. The final spring constant is thus 4 times equation (4.6).

With equations (4.5) and (4.6) the static behaviour of the actuator is described. These equations can be solved numerically. If we assume the force due to the parallel plate finger tips small compared to the force due the finger sidewalls an analytical solution for the driving voltage V_{switch} exists:

$$V_{switch} = \sqrt{\frac{4k_x x_{max}}{n\varepsilon}\frac{g}{h}} = \sqrt{\frac{4t^3 x_{max} gE}{n\varepsilon l^3}} \qquad (4.7)$$

For a thickness *t* of the spring beams of 2 µm and a length *l* of 450 µm, a maximum displacement x_{max} of 25 µm, a finger sidewall gap of g = 4 µm, a number of fingers on one side of *n* = 100 we obtain a switching voltage V_{switch} = 80 V. For the push-pull design the maximum actuator course x_{max} is only 10 µm, which reduces the switching voltage to 50 V. In this calculation we neglect the influence of the finger tips, the actual driving voltage will therefor even be lower.

The switching time τ is in the order of half the cycle time of a resonant cycle:

$$\tau \cong \frac{1}{2}\frac{1}{f_{res}} \approx \pi\sqrt{\frac{m}{k}} \qquad (4.8)$$

To reduce the switching time the mass of the actuator should be reduced as much as possible. The speed can also be increased by a stiffer suspension, but at the same time the driving voltage is increased according to equation (4.7). In equation

(4.8) the effect of the applied voltage on the speed is not taken into account; actually applying a higher driving voltage also reduces the switching time, because in the push-pull configuration the electrostatic force can be used to act in the same direction as the mechanical spring force. In this configuretion it is prefereble to have very compliant springs and to adjust the switching time be an increased voltage.

4.2.2.2. Transverse stability of comb actuator

In comb drive actuators the driving voltage can not be increased as much as one would like. On the one hand the moveable beam, where the comb fingers are attached, can be bent so much that the comb fingers touch the opposite electrode; this results in a short circuit and in breakdown. On the other hand a mechanical instability may arise in the transverse direction[52]. In the above mechanical description the problem is reduced to a problem of only one dimension. But the suspension springs and also the electrostatic actuator can generate forces also in the transverse y direction. If Δy expresses the transverse displacement of the comb structure out of the center, the electrostatic force in y direction can be expressed by:

$$F_y = \frac{1}{2} n \varepsilon V^2 h (l+x) \left(\frac{1}{(g-y)^2} - \frac{1}{(g+y)^2} \right) \qquad (4.9)$$

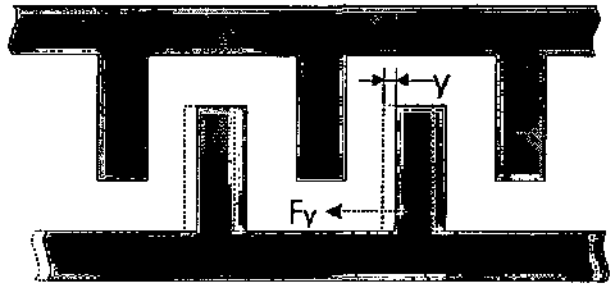

Figure 4.12: A perpendicular force apears if the comb strucure is out of center. This force acts in the same direction as the y-displacement and can result in mechanical instability.

In the center position the forces due to the perpendicular parallel plate capacitors compensate each other. If a small displacement in the y direction is introduced, this

equilibrium is not maintained anymore. A net electrostatic force appears oriented parallel to the displacement. Thus a sort of positive feedback is exerted on every transverse displacement. To ensure mechanical stability the spring force of the suspension beams in the *y* direction has to be larger than this electrostatic force to bring back the comb into its center position, where the transverse electrostatic forces are neutralised. Small displacements in the *y* direction can always occur due to vibrations and air noise. The stability criterion requires that the spring constant in the *y* direction is always larger than the first derivative of the electrostatic force:

$$k_y > \left.\frac{dF_y}{dy}\right|_{y=0} \qquad (4.10)$$

Introducing equation (4.9) yields:

$$k_y > 2\varepsilon n V_{max}^2 \frac{l + x_{max}}{g^3} \qquad (4.11)$$

If we replace V_{max}, the maximum voltage before instability, by the switching voltage of equation (4.7) we obtain the minium value for the ratio between the spring constant in longitudinal and transverse directions:

$$\frac{k_y}{k_x} > 2\frac{x_{max}(l_o + x_{max})}{g^2} \qquad (4.12)$$

The above equation shows that the gap distance *g* has a very strong effect on the necessary ratio of the spring constants and on the stability - it is in the second order in the denominator. Thus very small gaps, although they would reduce the driving voltage, can introduce mechanical instability. But the instability doesn't depend on the number of fingers *n*; the maximum displacement x_{max} also limits strongly the stability. According to the above equation the ratio of the spring constants should be higher than 100 to allow a maximum displacement of 25 µm at a finger sidewall gap of 4 µm. For a maximum displacement of only 10 µm in the push-pull configuration the spring constants ratio must only be higher than 20. The risk of a transverse instability is therefore much lower for comb actuators with reduced course.

To determine the spring constant in the transverse direction no simple analytical expression can be found. Therefore we have used finite element simulation with the Ansys© program to determine the spring constant in the *y* direction. For a beam thickness of 2 µm and a spring length of 450 µm the k_y/k_x ratio was evaluted to be 150, thus higher than the minimum requirement of 100. A stable operation is therefore possible over the hole displacement range of 25 µm.

4.3. Fabrication

Fabrication uses only a single mask and is explained in Figure 4.13. It starts with a photolithography on Silicon-on-Oxide (SOI) wafers to define the structure including mirrors, alignment grooves, actuators and suspension springs. We used conventional positive photoresist with a thickness of 2.2 µm. The height of the device layer has to be chosen in order to satisfy the application requirements, i.e. for single mode fibers a height of 75 µm is sufficient to cover the fiber core well. The spot diameter of single mode fibers is typically 10 µm and is located between 10 µm and 20 µm below the wafer surface. At this depth verticality and surface quality should be best.

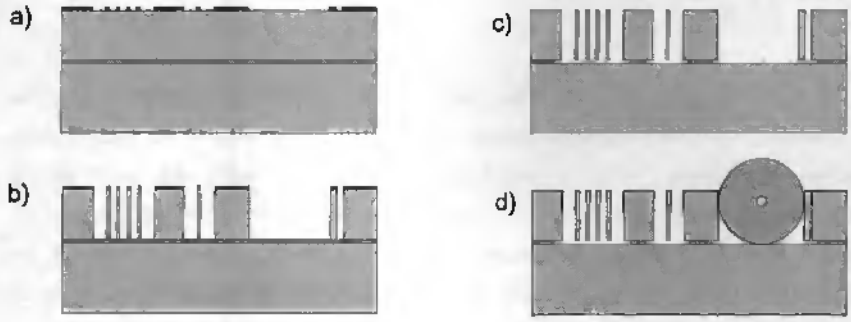

Figure 4.13: Fabrication of vertical mirror by DRIE. a) photolithography b) 75 µm vertical reactive Ion etching c) sacrificial layer etching d) vertical mirror metallisation and assembling of single mode fiber.

The key fabrication step is the vertical deep reactive ion etching (DRIE) of the 75 µm device layer. New developments in deep reactive ion etchers allow to fabricate

vertical structures with an aspect ratio above twenty[53,54]. Our device was etched on a commercial DRIE etcher from STS Ltd., (Gwent, UK) using an inductively coupled plasma (ICP) technology. With an ICP source etching can be done at lower pressures, which allows for an improvement in the profile control. In addition a proprietary sidewall passivation technique is used[53].

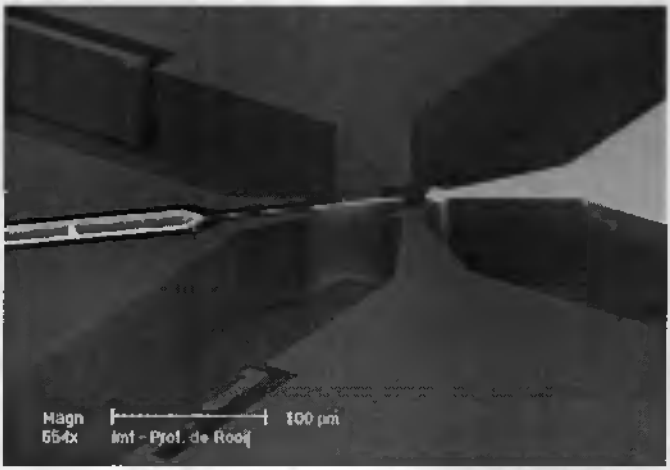

Figure 4.14: Vertical mirror and fiber grooves for tappered fibers fabricated by DRIE.

The etch selectivity between photoresist and silicon is about 1 : 50. Etching is stopped, when the buried oxide is reached. An example of an etched mirror is shown in Figure 4.14.

A critical step during the DRIE etching is when the last silicon above the buried oxide is removed. Due to the so called RIE lag or microloading effect[54] the small trenches are etched slower than larger ones. For our device we have to open 125 µm wide trenches for the optical fiber and at the same time small gaps for the comb drive actuator. While etching is continued to completely open the small trenches, the silicon dioxide layer is already reached in the fiber grooves. In this region the etching chemistry changes, because no more silicon has to be removed; this can lead to degradation of the surface quality of the walls above the buried oxide and cause considerable underetching especially in narrow trenches where the sidewall passivation is weaker. Figure 4.15 shows such a region where the underetching

along the buried oxide has completely freed the microstructures. Whereas the mirror of the wider trench in Figure 4.14 is intact almost down to the buried oxide.

Figure 4.15: Extreme case of overetching at the buried oxide interface.

After the plasma etching the resist is stripped. To free the mechanical structures the 2 µm thick sacrificial silicon dioxide layer is etched in hydrofluoric acid. During the drying after the sacrificial layer etching the movable structure may be pulled down to the substrate due to the capillary forces. Since the surface quality at the oxide interface is optically polished, the moveable structures stay easily bonded to the substrate. This sticking can be prevented as for the polysilicon micromachined structures by special rinsing and drying processes. But it was observed, that when an underetching along the buried oxide is performed by overetching during the plasma etching step, as shown in Figure 4.15, the sticking problem was also eliminated. On the one hand the gap is increased, but on the other hand the surface roughness is so high that no permanent bonding can occur anymore.

Finally to increase the reflectivity of the vertical mirrors, the silicon is aluminium coated. This is done by e-beam evaporation, where the wafers are oriented in an appropriate direction.

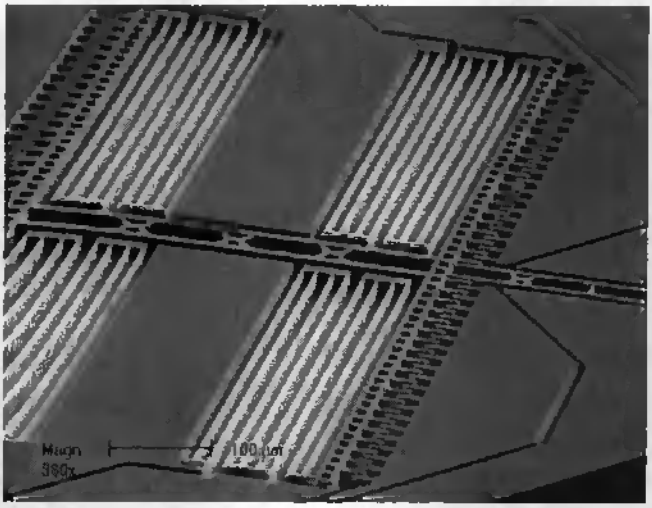

Figure 4.16: The vertical mirror is actuated by electrostatic comb actuators.

Figure 4.16 shows a finished actuator-suspension structure of a push-pull design. The thickness of the spring beams is 2 µm. The minimum gap between the finger sidewalls is 4-5 µm.

4.4. Characterisation

4.4.1. Mirror Characterisation

4.4.1.1. Mirror reflectivity

The reflectivity of the aluminium coated vertical mirrors is measured by placing a single mode fiber into the alignment groove of a shutter structure. The reflected light intensity is measured for different gaps between the fiber end and the mirror (see Figure 4.17 a).

From the reflectivity maxima and minima, which are due to the interference between the reflections at the fiber end and the vertical mirror, an equivalent mirror reflectivity of 76 % can be deduced, which includes the loss due to scattering and the verticality error of the mirror.

a) b)

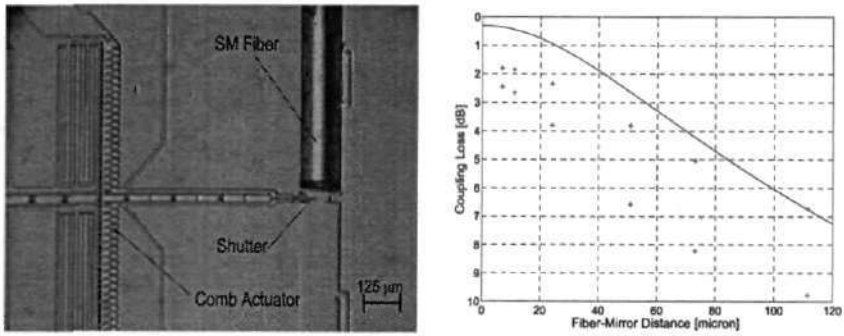

Figure 4.17: a) shutter-type vertical mirror for characterisation of the mirror's reflectivity. b) measured and calculated reflected light intensity as a function of mirror-fiber separation. Crosses show maximum and minimum values due to constructive and destructive interference. Plain line is calculated response for a vertical mirror 0f 100 % reflectivity.

4.4.1.2. Surface roughness

The surface roughness has been evaluated by visual inspection in an optical microscope in phase contrast mode. Figure 4.18 b) shows the etched surface of a 125 µm wide groove. The surface quality is best from the top surface to an etch depth of 30 µm, between 30 and 45 µm etch depth vertical notches are visible, finally between 45 and 75 µm etch depth the surface quality is degraded with a surface roughness up to 500 nm.

To measure precisely the surface roughness in the area around 15 µm etch depth we scanned the surface with an Atomic Force Microscope as shown in Figure 4.18 a). The rms surface roughness is 36 nm rms. According to Equation (1) light loss due to scattering should be lower than 6 %.

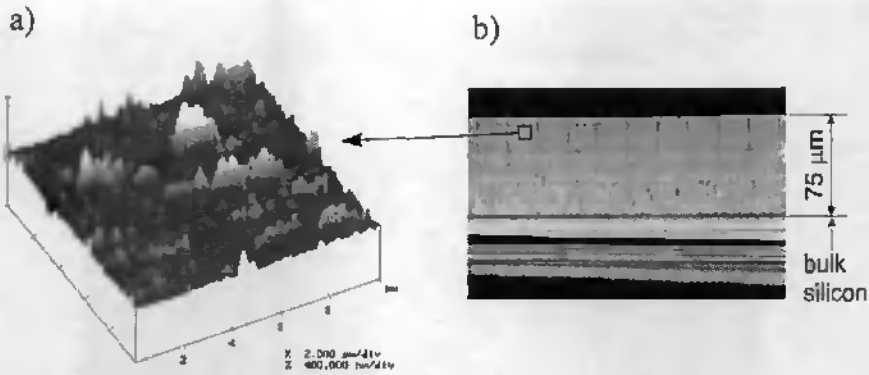

Figure 4.18: a) **AFM measurement and** b) **Optical micrograph in phase-contrast mode of etched surface for inspection of the surface roughness.**

4.4.1.3. Mirror verticality

Figure 4.19 shows a detail view of an etched mirror from which a verticality of the sidewalls of 89.3° can be deduced. The verticality of small trenches is even better. For the 75 µm high mirrors a minimal mirror thickness of 2.3 µm was achieved, which represents an aspect ratio of over 30. The initial line-width of the resist was 3.5 µm, thus the lateral underetching was about 0.6 µm. According to the loss calculation of Figure 4.19 a mirror thickness of 2.3 µm and a verticality error of 0.7° introduce an additional coupling loss close to 2 dB. The DRIE technology would allow to fabricate mirrors with an even better verticality. But due to the RIE lag effect the verticality can depend on the width of the trenches. If the process is optimised to get best verticality for the switching mirror in the large trenches of the fiber alignment groove, the profiles may become too positive in the small trenches of the comb structure resulting in closure of the trenches.

Figure 4.19: Detail showing the verticality of the mirror. Top mirror width is 2.3 µm, sidewall angle is 89.3°.

4.4.2. Actuator Characterisation

Before mounting the fibers into the silicon chip the electrostatic actuator is first tested. This is done under an optical microscope, where the chip can be contacted with prober needles. The test allows to eliminate poor designs and to determine the switching voltages.

a) b)

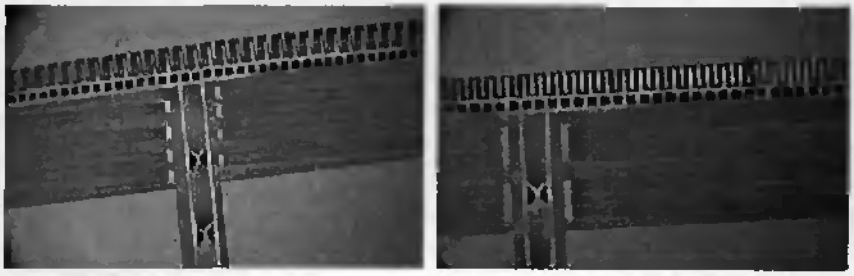

Figure 4.20: measured switching behaviour. A) single beam spring with instability. B) double beam spring with stable switching.

For the Push-Pull design a switching voltage of 30 V was necessary to pull the mirror out until the actuator was stopped by the landing electrodes. In the opposite direction the number of fingers is inferior, and here a operation voltage of 32 V was necessary to move the comb into its maximum position. As shown in Figure 4.20 this test also allows to eliminate design variations, which present a transverse instability. The structure of Figure 4.20 a) doesn't allow an actuation over the hole course because the transverse rigidity of the suspension spring is too weak. Actually the meander shaped suspension with only single beam springs has a k_y/k_x ratio of only 3, whereas with the double beam suspension of Figure 4.20 b) k_y/k_x ratio over 100 are possible[55].

4.4.3. Fiber Optic 2x2 Switch Characterisation

To characterise the switch single mode fibers with tapered ends are placed into the alignment grooves. The ends of the fibers are not lensed. In transverse direction the fibers are aligned by integrated springs, which hold the fibers in the groove. In the longitudinal direction the fiber end is moved as close as possible to the micromechanical mirror. In addition a glass plate is glued on top of the chip to fix the fibers in the vertical direction (see Figure 4.21).

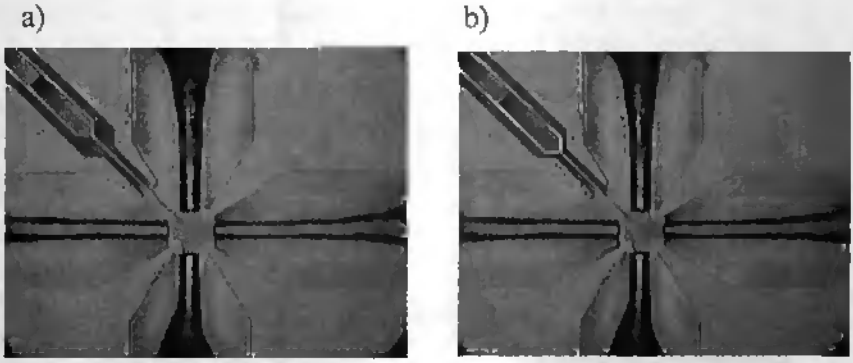

Figure 4.21: Optical micrograph of tapered fibers mounted on the switch. a) mirror in bar state. b) mirror in cross state.

Figure 4.21 shows an optical micrograph of the switch in its bar and cross state and The four single mode fibers have machined ends with a diameter of the end cylinder of 20 - 25 µm. The separation of the fiber ends is 50 µm. We measured an insertion

loss in the bar state between 0.6 and 1.6 dB and in the reflected state between 1.4 - 3.4 dB. These values are close to the theoretical limit, if one admits, that the fiber core may be slightly (< 1 μm) out of center and that the angle of the fiber end face may be not exactly 90°. Thus the alignment grooves align the fibers correctly. To further reduce the insertion loss the fiber ends should be brought even closer together. In addition special grade fibers should be used, which have a better concentricity and a better diameter control. Both a concentricity error and a different cladding diameter may cause a transverse offset. That a part of the loss is due to a transversal offset can be seen form the fact, that in the cross state there is a loss asymmetry; but the vertical mirror is defined be photolithography to be exactly in the center. To reduce the loss due to the Fresnel reflection at the fiber ends, these should be anit-reflective coated. An other possibility would be to fill the switch with a index matching oil. A simulation of the dynamic behaviour showed, that oil filling with a very low viscosity index matching oil would reduce the speed by a factor of 10^{55}.
Figure 4.22 a) shows the dynamic response of the reflected light intensity when the applied voltage isn't high enough to completely switch and the mirror only moves a couple of microns. From the overshoot ringing a resonance frequency of 1.3 kHz and a quality factor of about 4 can be deduced. In Figure 4.22 b) the voltage is increased and the mirror moves over the whole range. Here the light switching is complete. The cross talk attenuation is over 35 dB in the cross state and over 60 dB in the bar state. To further increase the cross talk attenuation the vertical mirror has to be coated with a thicker metal layer. Shortly after the switching small variations of the light intensity can be observed; these are due to vibrations of the mirror.

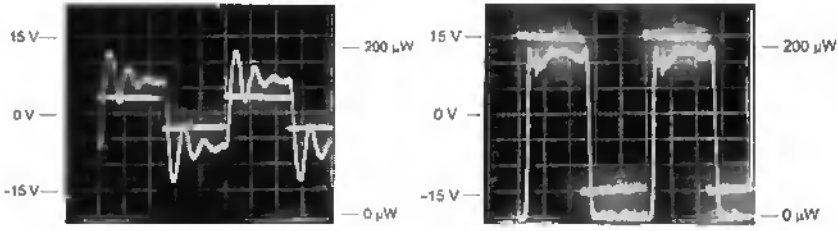

Figure 4.22: Response of reflected light signal to square signal of 200 Hz. a) below switching voltage. b) above switching voltage.

Figure 4.23 a) shows an enlarged view of the step response at the switching voltage of 30 V when switched from the cross into the bar state. The fall time is below 0.2 ms, whereas the 10% - 90 % fall time is only 80 µs. This can be explained by the fact, that the amplitude of the mechanical movement is higher than the spot diameter. Therefore only after 30 % of the mirror displacement the optical spot is reached and already after 70 % of the mirror course the optical spot is completely covered by the mirror. This can also be observed in Figure 4.23 b), which shows the reflected light intensity, when the mirror is moved into the optical path. After 200 µs the optical signal doesn't increase anymore. But only after 300 µs the vibrations due to the shock of the actuator against the landing electrodes are visible. In the time interval between 200 µs and 320 µs after the voltage step the mirror is still in movement before it hits the landing electrode.

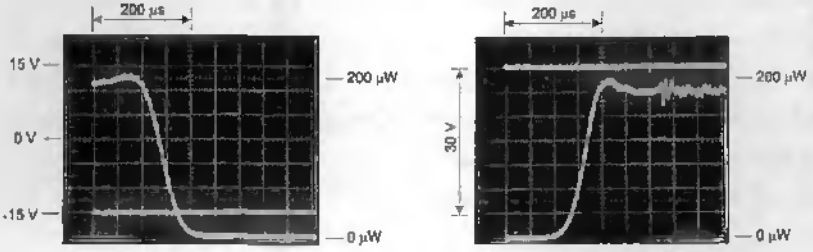

Figure 4.23: Step response of reflected light signal to 30 V steps. a) Switching from bar-to-cross state. b) Switching form cross-to-bar state.

Another factor, which has a positive effect on the switching time is the fact, that not only the suspension spring determines the switching speed; but in the push-pull design the comb actuators can accelerate the mirror structure as well. According to the resonance frequency of 1.3 kHz the half cycle time is 0.4 ms. If the switching speed was only determined by the spring suspensions, the switching time should correspond to this half cycle time. But the combined action of the electrostatic force and the spring force lead to this switching time reduction of about 25 %, i.e. according to Figure 4.23 b) the time the mirror needs to move from one landing electrode to the opposite is 320 µs. Table 4.3 resumes the characteristics of two push-pull type switches.

Table 4.3: Characteristics of two packaged 2x2 switches.

loss in bar state	loss in cross state	voltage bar state	voltage cross state	switching time (total)	10-90 % rise time	cross talk attenuation
0.6-1.6 dB	1.4-3.4 dB	28 V	30 V	0.2 ms	80 µs	> 35 dB

4.5. Conclusions

In this chapter we have reported on a micromechanical fiber optic switch which is based on a linear moveable mirror etched in silicon by deep reactive ion etching. Only one mask is needed to fabricate the silicon motherboard with the integrated mirror, actuator and alignment structures on it.

At the beginning of the chapter alternative solutions are reviewed. Especially the integrated waveguide based thermo-optical switch attracts interest. Fabricated on silicon with polymer waveguides it promises low cost and a reasonable switching speed around 1 millisecond. The micromechanical switch should be competitive compared to such thermo-optical switches.

In the next part of the chapter design considerations are discussed. It can be shown that the distance between the fiber ends has to be smaller than 50 µm to obtain a coupling loss below 1 dB (20 %). To bring the fibers so close together their ends have to be machined to a conical shape. An additional coupling loss is introduced by the mirror, which should present a good verticality, a high reflectivity and a low roughness. A verticality error of 1° introduces an additional loss of 1 dB already. To increase the reflectivity of silicon, it has to be coated with either aluminium or gold. Finally the roughness should remain below 47 nm or 3.6 % of the wavelength to keep the scattering loss below 10 % (0.46 dB). The mirror is actuated by electrostatic comb actuators. The suspension springs and the comb dimensions have to be designed carefully in order to prevent transverse instability of the actuator. A method to calculate the stability of the actuator is presented.

Than the fabrication based on deep reactive ion etching is reviewed. Mirrors 75 µm in height were successfully fabricated. The characteristics are outstanding: a

minimal thickness of 2.3 µm, a verticality better than 89.3° and a rms roughness below 36 nm was obtained.

With such chips first prototypes were assembled. These prototypes showed promising performance: the insertion loss can be reduced below 1 dB in the bar state and below 2 dB in the cross state. The use of micromechanics allows for a considerable increase in the switching speed. The total switching time is a factor of 50 shorter than for conventional mechanical switches and even somewhat faster than thermo-optic switches.

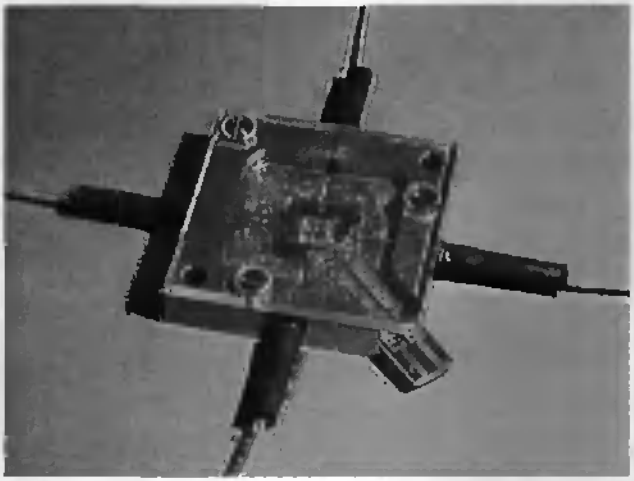

Figure 4.24: Packaged 2x2 fiber optic switch.

Since the alignment grooves, which allow for a passive alignment of the single mode fibers, are already integrated on the silicon chip, the packaging can be very simple. Figure 4.24 shows a fully packaged device, where the silicon chip is placed into a steel package to get a handy and robust device. The size of the base plate is only 3 x 3 cm.

A drawback of the present switches is their high backreflection of 4 %. Conventional mechanical switches use index matching oil to reduce the backreflection. The use of such an oil would decrease the switching time by an order of magnitude approximately. In our switch antireflective coating of the fiber end face is more appropriate.

Future improvements will aim reproduceable low insertion losses and an improved packaging, that includes a driver electronics. To reproduce low losses in a series production special grade fibers have to be used with an excellent core concentricity and constant fiber diameter.

[1] F. J. Leonberger and C. O. Bolzer, "GaAs Directional coupler switch with stepped Δβ Reversal", Applied Physics Letters, vol. 31, no. 3, pp. 223-226 (1977)

[2] Y. Silberberg, P. Perlmutter and J. E. Baran, "Digital Optical Switch", *Applied Physics Letters*, October 1987, vol. 51, no. 16, pp. 1230 - 1232, (1987)

[3] P. Granestrand, B. Stoltz, L. Thylen, K. Bergvall, W. Döldissen, H. Heinrich and D. Hoffmann, "Strictly nonblocking 8 x8 integrated optical switch matrix", *Electronics Letters*, 17th July 1986, Vol. 22, No. 15

[4] J. Schmidtchen, A. Splett, B. Schüppert, G. Burbach and K. Petermann, "Low loss single mode optical waveguides with large cross-section in silicon on insulator", *Electron. Lett.*, vol. 27, No. 16, pp. 1486-1487, (1991)

[5] K. Ishida, H. Nakamura, H. Matsumura, T. Kadoi, and H. Inoue, "InGaAsP/InP Optical Switches Using Carrier Induced Refractive Index Change", *Applied Physics Letters*, January 1987, vol. 50, no. 3, pp. 141-142 (1987)

[6] P. Mottier, "Integrated optics at the laboratoire d'electronique, de technologie et d'instrumentation", *Int. J. Optoelectron*, 1994, 9, (2), pp. 125-134

[7] G. R. Möhlmann, "Polymeric optochips: splitters, switches and modulators", *Synthetic Metals* 67 (1994) pp. 77-78

[8] N. Keil, H. Yao and C. Zawadzki, "Polymer technology for low cost integrated optical waveguide devices", *Proceedings of Micro System Technologies '96*, Ed. Reichl ,Berlin: Springer Verlag, pp. 531 - 538, (1996)

[9] R. Moosburger, G. Fischbeck, C. Kostrzewa, M. Töpper and K. Petermann, "Integrated Thermo-Optical Switch based on Polymer Rib Waveguides", *Proceedings of Micro System Technologies '96*, Ed. Reichl ,Berlin: Springer Verlag, pp. 543 -548, (1996)

[10] M. Hoffmann, E. Voges. *Proceedings of 7th Europ. Conf Integr. Opt. ECIO 1995*, Delft, p. 403-406.

[11] R. Jebens, W. Trimmer and J. Walker, "Microactuators for aligning optical fibers", *Sensors and Actuators 20*, pp 65-73 (1989)

[12] S. Nagaoka, "Micro-magnetic Alloy tubes for switching and Splicing Single-Mode Fibers", *Proc. 4th IEEE Workshop on Micro-Electro-Mechanical Systems (MEMS 91)*, Nara, Japan, Jan. (1991), pp. 86-91

[13] S. Nagaoka, "Optomechanical Switches for Fiber-Optic Communication Systems", *Proc Spie Int. Conf on Optical Fabrication and Testing, Vol 2576*, pp. 383-394, (1995)

[14] S. Nagasawa, H. Furukawa, T. Atake, N. Kashima, "New type of optical switch with a plastic molded ferrule", *Trans. Inst Electron. Inf. Commun. Eng. E70 (8)*, pp. 696-698 (1987)

[15] M. F. Dautartas, A. M. Benzoni, Y. C. Chen, G. E. Blonder, B. H. Johnson, C. R. Paola, E. Rice, Y. H. Wong, "A silicon based Moving Mirror Optical Switch", *Journal of lightwave tech.* 10 (8), 1076-1085 (1992)

[16] H. Gnewuch, R. Ulrich, "Fiber-optic 1x6 switch with smooth transmission spectrum", *Sensors and Actuators, A 45*, (1994), pp. 109 - 114.

[17] Y. Hakamata, T. Yoshizawa and T. Kodaira, "A 1.3 mm Single-Mode 2x2 Liquid Crystal Optical Switch", *IECE Trans. MOMMUN., Vol. E77-B*, No. 10 October 1994

[18] L. A. Field, D. L. Burriesci, P. R. Robrish and R. C. Ruby, "Micromachined 1x2 optical fiber switch", *Tech. Dig. 8th International Conference on Solid-State Sensors and Actuators (Transducers '95)*, Stockholm, Sweden, june 1995, vol. 1, p.344-347.

[19] Y. Kikuya, M. Hirano, K. Koyabu and F. Ohira, "Micro Alignment Machine for Optical Coupling", *IEEE Workshop on Micro Electro Mechanical Systems (MEMS '93)*, Fort Lauderdale, Florida, Feb. 7-10, 1993, pp. 36 - 41

[20] K. Hogari and T. Matsumoto, "Electrostatically driven fiber-optic micromechanical on/off switch and its application to subscriber transmission systems", *J Lightwave Technol.*, vol 8, pp. 722-727, 1990

[21] S. Nagaoka, "Micro-Magnetic Alloy Tubes for Switching and Splicing Single-Mode Fibers", *Proc. 4th IEEE Workshop on Micro-Electro-Mechanical Systems (MEMS 91)*, Nara, Japan, Jan. (1991), pp. 86-91

[22] S. Nagaoka and Y. Suzuki, "Compact Optomechanical Switches and their Applications in Optical Communication and Testing Systems", *Proceedings of 10th IEEE Workshop on Micro-Electro-Mechanical Systems (MEMS 97)*, Nagoya, Japan, January 26-30, pp.366-371 (1997)

[23] E Ollier, P. Labeye, F Revol, "Micro-Opto Mechanical Switch Integrated On Silicon", *Electron. Lett.* 31 (23), pp 2003-2005 (1995)

[24] S S Lee, L Y Lin, M C Wu, "Surface Micromachined Free Space Fiber-Optic Switches", *Elec. Lett.* 31 (17), 1481-1482 (1995)

[25] J. Mohr, M. Koh, and W. Menz, "Micro Optical Switching by Electrostatic Linear Actuators with Large Displacements", *7th Int. Conf. on Solid-State Sensors and Actuators (Transducers '93)*, Jun. 7-10, 1993, pp. 120-123.

[26] H. Toshiyoshi and H. Fujita, "An Electrostatically Operated Torsion Mirror for Optical Switching Device", *Tech. Dig. 8th International Conference on Solid-State Sensors and Actuators (Transducers '95)*, Stockholm, Sweden, june 1995, vol. 1, pp. 297 - 300

[27] J. H. Comtois and V. M. Bright, "Surface Micromachined Polysilcon Thermal Actuator Arrays and Applications", *Proc. 1996 Solid-State Sensor and Actuator Workshop*, Hilton Head Island, SC, 2-6 June, 1996

[28] Y. Uenishi, T. Masahiro and M. Mehregany, "Micro-Opto-Mechanical Devices Fabricated by Anisotropic Etching of (110) Silicon", *J Micromech. Microeng.* 5 (1995) 305-312

[29] L. Rosengren, L. Smith and Y Bäcklund, "Micromachined Optical Planes and Reflectors in Silicon", *Sensors and Actuators A*, 41-42 (1994), 330-333

[30] L. Smith, L. Tenerz and B. Hök, "Silicon Micromachined (2x2) Opto-coupler", *Spie Vol. 1281, optical Interconnections and Networks (1990)*, pp. 91-95

[31] K. Akimoto, Y. Uenishi, K Honma and S. Nagaoka, "Evaluation of Comb-Drive Nickel Micromirror for Fiber Optical Communication", *IEEE International Workshop on Micro Electro Mechanical Systems*, 26 - 30 january 1997, Nagoya, Japan, pp. 67-71

[32] Y. Uenishi, K. Honma and S. Nagaoka, "Tunable Laser Diode Using A Nickel Micromachined Tunable Mirror", *Electron. Lett.*, Vol. 32, No. 13, (1996), pp. 1207 - 1208

[33] J. Mohr, J. Göttert, A .Müller, C. Müller, "Micro-Optical Components and Systems Fabricated by the LIGA Technique", *Proceedings of EOS Engelberg* 1996

[34] A. Müller, J. Göttert and J. Mohr, "LIGA Microstructures On Top Of Micromachined Silicon Wafers Used To Fabricate A Micro-Optical Switch", *J. Micromech. Microeng.* 3 (1993) pp. 158-160

[35] K. S. J. Pister, M. W. Judy, S. R. Burgett and R. S. Feering, "Microfabricated Hinges", *Sensors and Actuators A*, Vol. 33, p. 249-256 (1992)

[36] C. R. King, L. Y. Lin and M. C. Wu, "Out-of-Plane retractile microlens fabricated by surface micromachining", *IEEE Photonics Tech. Lett.*, Vol. 8, no. 10, p. 1349-1351 (1996)

[37] M. C. Wu, L. Y. Lin, S. S. Lee, and K. S. Pister, "Micromechanical Free-Space Integrated Micro-Optics", *Sensors and Actuators* A, Vol. 50, pp.127-134 (1995)

[38] L. Y. Lin, J. L. Shen, S. S. Lee, G. D. Su, and M. C. Wu, "Microactuated Micro-XYZ Stages For Free-Space Micro-Optical Bench", *IEEE International Workshop on Micro Electro Mechanical Systems*, 26 - 30 january 1997, Nagoya, Japan, pp. 43 - 48

[39] M. H. Kiang, O. Solgaard, R. S. Muller and K. Y. Lau, "Micromachined Polysilicon Microscanners For Barcode Readers", *IEEE Photon. Technol. Lett.*, Vol. 8, no. 12, 1996

[40] C. Linder, T. Tschan and N. F. de Rooji, "Deep Dry Etching Techniques As A New IC Compatible Tool For Silicon Micromachining", *Proc. 5th Int. Conf. Solid-State Sensors and Actuators (Transducers '91)*, San Francisco, CA, USA, 24-28 June, 1991, pp. 524-527

[41] E. H. Klaassen, K. Petersen, J. M. Noworolski, J. Logan, N. I. Malu, J. Brown, C. Storment, W. McCulley and G. T. A. Kovacs, "Silicon Fusion Bonding And Deep Reactive Ion Etching: A New Technology For Microstructures", *Sensors and Actuators A* 52 (1996), 132 - 139.

[42] V. P. Jaecklin, C. Linder, N. F. de Rooij and J. M. Moret, "Micromechanical Comb Actuators with Low Driving Voltage", *J. Micromech. Microeng.* 2 (1992) pp. 250 - 255

[43] R. Legtenberg, A. W. Groeneveld and M. Elwenspoek, "Comb-Drive Actuators for Large Displacements", J. Micromech. Microeng. 6 (1996) pp. 320-329

[44] L. Ward , *The Optical Constants Of Bulk Meterials And Films*, IOP Publishing, 1994, Chapter 7

[45] H. A. Macleod, *Thin Film Optical Filters*, Adam Hilger Ltd, 1980, Chapter 2

[46] M. Bass, Editor, *Handbook of Optics*, Vol II, McGrawHill, 1995, Chapter 35

[47] John C. Stover, *Optical scattering Measurement and analysis*, McGraw-Hill, 1990, Chaps. 2-3.

[48] T. V. Vorburger, E. Marx, T. R. Lettieri, "Regimes Of Surface Roughness Measurable With Light Scattering", *Applied Optics*, Vol. 32 No. 19, 1993, pp. 3401-3408

[49] P. Beckmann and A. Spizzichino, *The Scattering of Electromagnetic Waves from Rough Surfaces*, Artech, Norwood, Mass., 1967, Chaps. 3-5

[50] C. M. Miller, *Optical Fiber Splices And Connectors*, Marcel Dekker Inc., 1986, Chapter 4

[51] Raymond J. Roark, Warren C. Young, *Formulas for Stress and Strain*, McGraw-Hill Book Company, Singapore, 1976

[52] T. Hirano, T. Furuhata, K. J. Gabriel, and H. Fujita, "Design, Fabrication and Operation of sub-micron gap electrostatic comb drive actuators", *J. Microelectromech. Syst. 1* (1992), pp. 52-59.

[53] J. K. Bhardwaj, H. Ashraf, "Advanced Silicon Etching Using High Density Plasma", *Spie Vol. 2639, Proceedings of Micromachining and Microfabrication Process Technology*, Oct. 1995, Austin Texas, pp. 224 - 233

[54] H. Jansen, M. de Boer, M. Elwenspoek, "The Black Silicon Method VI, High Aspect Ratio Trench Etching For MEMS Applications", *Proceedings of the IEEE Workshop on Micro Electro Mechanical Systems (MEMS '96)*, San Diego, USA, jan. 1996, pp. 250 - 257

[55] C. Thio, "Opto-Mechanical By-Pass Switch for Optical Single Mode Fibers", Diploma Thesis, University of Neuchatel - EPFL, Neuchatel (1997), Chapter 3

Chapter Five

Reliability Considerations

5.1. Introduction

In view of a commercial application of micromechanical devices the important question of long term stability and reliability has to be addressed. Because there exist almost no electrostatic micromachined actuators on the market, field data, i.e. empirical experience, is not available. On the other hand long test cycles are not conceivable, thus a procedure has to be applied which allows the prediction of the long time stability, within a much shorter time than the final operation time.

In micro-electromechanical systems sizes and forces are reduced to a micron scale; small changes in the material properties, which didn't have an influence on macroscale devices can completely alter the function of microscale devices. In litterature crack growth[1] and in-use sticking[2] have been discussed as potential breakdown mechanisms for micromachined actuators. In this chapter we will discuss possible degradation under mechanical, and electrostatic stress, under different environmental conditions and for mechanical contacting surfaces. The comparison between the material strength with respect to these stresses will allow to give a qualitative figure for the reliability of the reflective modulator and the fiber optic switch. We will concentrate on the failure mechanisms of microactuators;

failures such as breakdown of chip or wire bonds are identical to microelectronic circuits, about which good analyses exist in literature[3].

In the past a good compliance between specifications and performance parameters at the end of the fabrication process was often sufficient to achieve a high quality prototype. In other words development targets seemed to be reached when the item considered was free of systematic failures. The important question of long time behaviour was only rarely addressed systematically. The goal of this chapter is to investigate into the failure mechanisms of two micromachined actuators - the reflective modulator and the fiber optic switch - and to find a qualitative and if possible also a quantitative figure for the failure probability. After a short introduction into some concepts of reliability probabilities and presentation of the analysis procedure, we will discuss potential breakdown mechanisms, i.e. mechanical stress, electrostatic stress, air humidity and mechanical contacts during operation.

5.2. Analysis Procedure

Reliability is a characteristic of an item, generally designated by *R*, and expresses the probability that the item will perform its required function under given conditions for a stated time interval. Considered qualitatively, reliability can also be defined as the ability of an item to remain functional. The *required function* specifies the item's task and figures as the starting point for any reliability analysis, as it defines failures. *Operating conditions* have an important influence upon reliability, and must therefore be specified with care.

The failure rate $\lambda(t)$ of an item expresses the probability per unit time of failure. It can be shown, that the failure rate $\lambda(t)$ fully determines the reliability function $R(t)$:

$$R(t) = e^{\int_0^t -\lambda(\tau)\,d\tau} \qquad (5.1)$$

In many practical applications, the failure rate can be assumed to be constant or nearly so for all $t > 0$.

$$\lambda(t) = \lambda \qquad (5.2)$$

For a constant failure rate equation (5.1) becomes:

$$R(t) = e^{-\lambda t} \qquad (5.3)$$

The failure free operating time τ is in this case *exponentially distributed*. For this, and only for this case the failure rate can be estimated by $\lambda = k / T$, where T is the cumulative operating time and k the total number of failures during T.

The mean of the failure-free operating time (MTTF) is generally expressed as

$$MTTF = E[\tau] = \int_0^t R(x)dx \qquad (5.4)$$

in the case of a constant failure rate, MTTF becomes:

$$MTTF = \frac{1}{\lambda} \qquad (5.5)$$

For semiconductor devices typical figures for λ are 10^{-10} to 10^{-7} h^{-1} for components, and 10^{-7} to 10^{-5} h^{-1} for assemblies[3]. A failure rate of 10^{-5} h^{-1} represents a mean time to failure of 11 years.

Very long test periods cannot be accepted in the development stage. Though techniques have to be applied to accelerate the determination of the failure rate. The determination of the assessed reliability, which is obtained from field data and statistical interpretations, can be accelerated be making the operating conditions in laboratory harsher. This can give useful results as long as the mechanisms of failure are not changed. For example the failure rate of semiconductor components will double for an operating temperature increase of 10 to 20 °C, due to the acceleration of the diffusion processes. But too large an increase of the temperature leads to new failure mechanisms, which don't occur at ambient temperature. At temperatures too high the failure rate can't be extrapolated to room temperature.

For our micromechanical actuators we will use a different way to determine the reliability. The reliability estimation will be based on the comparison of the material strength with the operation stress. The procedure for the quantitative reliability analysis is[3]:

1. Formulation of failure hypotheses.
2. Evaluation of the stresses applied with respect to the critical failure hypotheses.

3. Evaluation of the strength limits. (dynamic and static)
4. Computation of the component reliability.

In a first step failure hypotheses are formulated for a given device. Both the reflective modulator and the fiber optic switch are electrostatic actuators. Possible breakdown mechanisms can arise from the mechanical stress, from the high electric field and from environmental conditions, i.e. air humidity. In the fiber optic switch the mirror movement is limited by landing electrodes. The mechanical contact between two surfaces can present an additional failure mechanism: permanent sticking of two surfaces. This failure only exists for the fiber optic switch. Table 5.1 resumes possible failure mechanisms for our two electrostatic microactuators.

Table 5.1: Stress types present in electrostatic actuators and related potential breakdown mechanisms:

stress type	mechanical	electrostatic	environment	contacts
failure	rupture	arc discharge	corrosion	sticking
hypothesis	fatigue	charge up		
possible in	modulator and switch	modulator and switch	modulator and switch	only switch

In the next step the operational stress and also the strength limit with respect to the failure hypotheses is evaluated. The comparison of the operation stresses with the strength, allows for a qualitative estimation of the reliability.
The following discussion on reliability will be grouped according to the types of failure mechanisms, i.e. in mechanical, electrostatic, environmental and failures related to contacts between moving parts. For every group we will determine the operation stress in the fiber optic switch and in the reflective modulator. Then we will estimate the strength with respect to the failure hypothesis and finally we will discuss the expected reliability by comparing the strength limit with the operation stress.

5.3. Mechanical Reliability

5.3.1. Maximum Stress during Operation

For the fiber optic switch the maximum stress arises in the clamping ends of the suspension springs. Denoting the deformation of the beam end Δx the maximum stress is[4]:

$$\sigma_{max} = \frac{3Et}{l^2}\Delta x \qquad (5.6)$$

, where E is the Young modulus of silicon, t is the thickness of a single suspension beam and l the length of a beam. For the design with the one-directional actuator the displacement of a single suspension beam is Δx = 12.5 µm. The beam thickness is t = 2 µm and length is l = 450 µm. According to the above equation the maximum tensile stress in the fiber optic switch is 63 MPa.

For the reflective modulator the membrane geometry is slightly different, but a similar analytical formula can be derived[4]:

$$\sigma_{max} = \frac{12Et}{l^2}\Delta x \qquad (5.7)$$

For a membrane length l of 50 µm, a *thickness* t = 0.49 µm, and a maximum deflection of 0.3 µm, the forgoing formula yields a maximum stress of 120 MPa, which is twice as high as for the fiber optic switch.

The above formulas don't take into account the stress concentration, that may occur in the clamping end. In addition the deformation introduces a tensile stress in the membrane of the reflective modulator. To evaluate these effects the maximum mechanical stress in the membrane of the reflective modulator was evaluated with the finite element program ANSYS©.

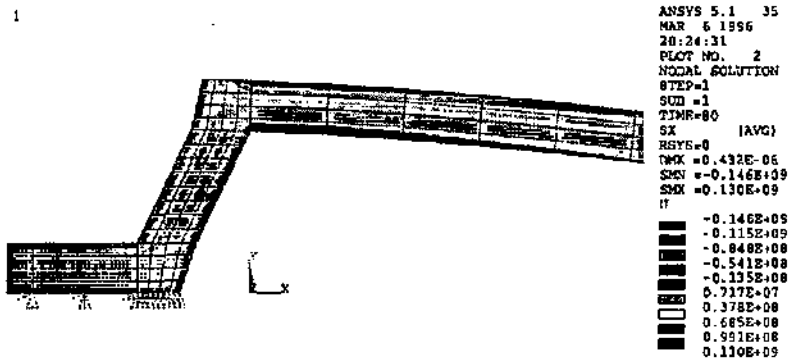

Figure 6.1: Stress in x direction at the clamping end for a displacement of the membrane center of 0.3 µm.

In this simulation we reduced the problem to a 2 dimensional model. The initial air gap is 1.55 µm. Under actuation the membrane has to deform by 0.3 µm to put the modulator in the low reflection state. Figure 5.1 shows the stress distribution in a cross section of the clamping end for a displacement of the membrane center of 0.3 µm. It is seen, that the maximum stress arises in the stress concentration at the clamping end of the structures. For the operational displacement of 0.3 µm the maximum stress intensity is 130 MPa, thus only slightly higher than the analytical calculation.

But during the fabrication process the membrane deformation may be higher. Typically during the rinsing and aluminium evaporation process the free standing membrane is deformed until it touches the underlying substrate. For this occasional deformation the maximum stress intensity is much larger than during operation. Accrding to a FEM ananlysis the maximum tensile stress in the membrane reaches 1.5 GPa for a beam displacement of 1.55 µm. This value is a 240 % higher than what has been expected according the analytical calculation. This increase is due to the non-linear deformation of the membrane.

For an admitted mean time to failure of 20 years, the number of cycles the modulator has to withstand can be calculated assuming a working frequency of 1 MHz. Assuming 20 years of continuous operation this calcualtion yields a number of 6.3e14 cycles, during which the membrane has to withstand stress amplitudes of 120 MPa.

5.3.2.Rupture Strength

Silicon can be regarded as an ideal brittle material with a covalent bonded crystaline structure. At room temperature no plastic strain can be observed prior to fracture. The dislocations, the movement of which is responsible for plastic deformation, are not mobile at room temperature. All the same the velocity of dislocation displacement increases with temperature according to an Arrenius law with an activation energy of 2.2 eV[5]. Only at temperatures over 600 °C plastic strain prior to fracture can be observed. Below that temperature the fracture occurs when a critical stress intensity is reached at a crack tip[5]. Fracture process consists essentially of bond rupture at the tip of a sharp crack, i.e. silicon specimens fail by cleavage with no formation of dislocations[6]. In contrast to this ideally brittle behaviour of silicon, ductility, i.e. non reversible dislocation motion, accompanies fracture in metals.

The tensile fracture strength of a brittle material can be understood in terms of Griffith's equation[7]:

$$\sigma_f = \frac{K_C}{Y\sqrt{a}} \qquad (5.8)$$

where Y is a dimensionless parameter that depends on the geometries of the crack and the specimen. Y is called the finite size correction factor and values have been tabulated for many different geometries[8]. For plane stress in the tensile opening mode the geometrical factor is $Y = \sqrt{\pi}$; a is the crack length and K_C is the stress intensity factor, it is often called the *fracture toughness* of the material. K_C is a material property, which is related in the original theory of Griffith to the surface tension of the material.

Equation (5.8) expresses that the strength of a brittle material depends on a combination of a material property, i.e the fracture toughness K_C, and the flaw size. Using this formalism, if we know the value of K_C for a material then we know the size of flaw it can tolerate at a given stress or if we know the strength and K_C it is possible to calculate the critical size in the specimen.

In literature a value for the fracture toughness of single crystal silicon can be found[5]:

$$K_{IC}^{110} = 0.9\,MPa\sqrt{m} \qquad (5.9)$$

with that value it is possible to estimate the strength for different flaw sizes or as a function of the surface roughness. Numerical calculation of equation (5.8) in Table 5.2 shows, that the rupture strength should lie between 1.5 GPa and 7 GPa, if the maximum crack length is between 100 nm and 5 nm:

Table 5.2: calculated strength of silicon for different crack length (K_{IC} assumed to be 0.9 $MPa\sqrt{m}$)

crack length	100 nm	10 nm	5 nm
strength	1.6 GPa	5 GPa	7 GPa

The defects, that may lead to cracks in silicon can be devided into three principal categories:

surface cracks: roughness due to deposition, plasma etching, sacrificial layer etching, cracks due to large deformation

fabrication flaws: inclusions, crystal imperfections, weak grain boundary (deposition)

environmentally induced flaws: corrosion, slow crack growth during operation

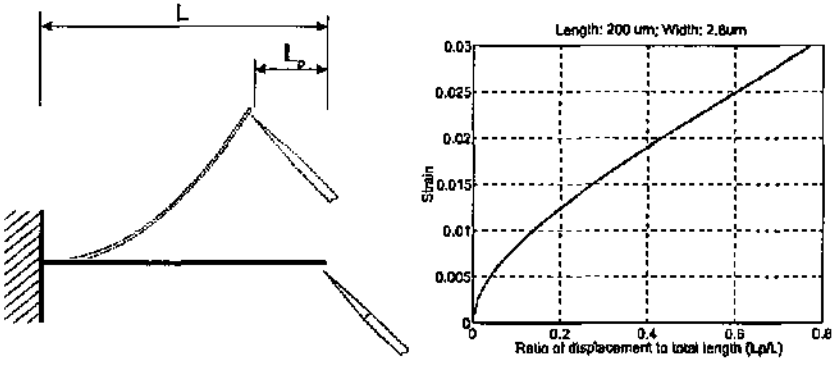

Figure 5.2: Large deformation of a simply clamped beam and the simulated maximum tensile strain as a function of the tip displacement ratio L_p/L. (length: 200 µm; width 2.8 µm)

For an experimental evaluation of the yield strength we have bent microfabricated cantilever structures until rupture. As the operation stress is considerably higher in the reflective modulator we will only consider the rupture strength of polysilicon, which is all the same supposed close to that of single crystal silicon. By using a micoprober needle a cantilever is bent until it yields. The experiment was observed under the light microscope and was recorded on a video tape for later analysis[9]. The maximum tensile strains are calculated by nonlinear beam theory[10]. Figure 5.2 shows the schematics of the experience and the calculated dependence of maximum tensile strain on the projected displacement of the beam end [11].

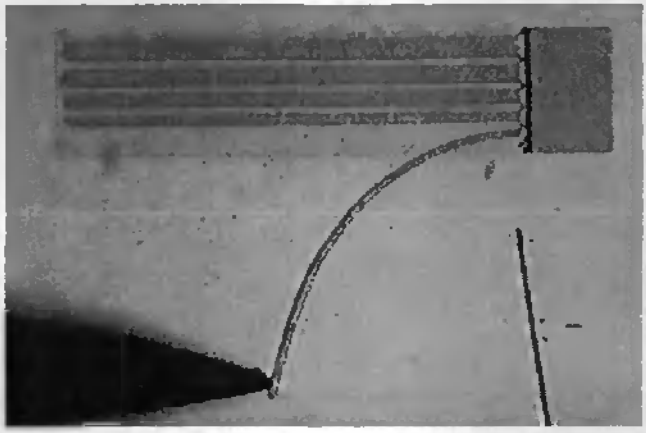

Figure 5.3: Optical micrograph showing maximum lateral bending of a polysilicon cantilever (200 µm long, 2.8 µm wide and 2 µm high) before yielding.

By testing 9 of these structures an average fracture strain of 2.6 % was measured. Assuming a Young modulus of about 160 GPa, the meausured fracture stress of polysilicon is $\bar{\sigma}$=3.89 GPa. The scatter in the strength of polysilicon can be expressed in terms of the variance $\Delta\sigma$ = 0.53 GPa. Prior to fracture no plastic strain could be observed, i.e. after releasing the beams they returned to their initial position.

Strength values for a brittle material generally exhibit a large variation. A mathematical tool, that allows a probabilistic prediction of the strength, is the

distribution function proposed by Weibull[12]. As the thin film actuators are mainly exposed to bending moments, the maximum stress intensities are produced at the surface. Thus it is assumed, that surface flaws control failure. The reliability, in absence of slow crack growth, of a given component to survive a stress σ is:

$$R(\sigma) = e^{-\left(\frac{\sigma}{\sigma_0}\right)^m} \qquad (5.10)$$

, where m is the Weibull modulus, σ_0 is the Weibull scaling constant. In the above experiment the yield strength values in Table 5.3 could be measured. They are ordered in increasing order. A failure probability is associated with every measurement. The failure probailty is calculated in taking the median probability for the i th mesurement, where i is the position of the ordered elements[13]:

$$F(\sigma_i) \approx \frac{i - 0.3}{n + 0.4} \qquad (5.11)$$

, n is the total number of measurements, i.e. 9 in our case.

Table 5.3: measured yield strength [GPa] and corresponding failure probability [%]:

i	1	2	3	4	5	6	7	8	9
σ_i	2.47	2.70	2.80	2.97	3.16	3.18	3.55	4.11	4.39
$F(\sigma_i)$	7.4	18.1	28.7	39.4	50	60.6	71.3	81.9	92.6

These measured failure probabilities are the basis for calculating the parameters of the Weibull distribution. The function

$$F(\sigma) = 1 - R(\sigma) = 1 - e^{-\left(\frac{\sigma}{\sigma_0}\right)^m} \qquad (5.12)$$

has to be fitted to the failure probabilities, i.e. to the 9 measurements of Table 5.3. This is done numerically and Figure 5.4 shows the result. The Weibull parameters of

the fitted curve are: the Weibull scaling constant σ_0 is 4.15 GPa and the Weibull modulus m is 7.64; we admitted that the failure free threshold stress σ_u is zero.

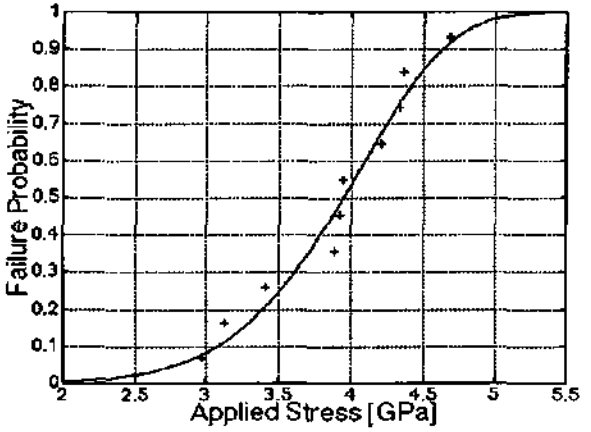

Figure 5.4: Measured rupture strength of polysilicon and fitted Weibull function. Weibull parameters of rupture strength are: σ_0 = 4.15 GPa and m = 7.5.

Assuming the K_C of polysilicon close to that of single crystal silicon the average flaw length a can be calculated for the measured rupture strength. With Kc = 0.9 $MPa\sqrt{m}$, equation (5.8) yields a flaw size of a = 17 nm, which is in the order of magnitude of the surface roughness, but smaller than the grain size of fine grained polysilicon, which is in the order of 100 - 200 nm[14].

5.3.3.Long Cycle Fatigue

In contrast to the fast rupture, which was discussed in the above paragraph, fatigue is described as slow propagation of cracks.

The phenomenon of fatigue is known since the invesligation into steel byAugust Wöhler in the second half of the last century. He showed that cyclic deformation well below the elastic limit can lead to failure after many cycles. This phenomenon is called long cycle fatigue. It can be explained by the formation and propagation of

cracks, which lead to failure, when they reach a critical size. This critical crack size leading to rupture can be related to the applied stress by equation (5.8).

The fatigue process can be subdivided into three stages:

1) initiation of dominant cracks
2) slow growth of the cracks
3) at the critical crack-size: fast propagation of the crack

Initiation of a crack can start from a surface inhomgenity, from inclusions or other material defects. If cracks are already present after the fabrication the crack-initiation stage is not necessary. The fatigue process amounts to slow crack propagation of the existing cracks and rupture.

As opposed to metallic materials dislocations in silicon are not mobile at room temperature. This mobility of dislocations has been regarded for a long time to be a necessary condition for fatigue to occur. This is because fatigue phenomena have first been investigated in metallic materials. Cyclic stress effects in ductile metals are intimately related to the to-and-fro motion of dislocations. These moving dislocations can pile up at the crack tip and lead to crack growth. In silicon dislocations are not mobile at room temperature; one could assume that fatigue cannot occur in silicon. However a broader examination of the requirements for cyclic fracture in both ductile and brittle solids clearly indicates that *kinematically irreversible* microscopic deformation is the precursor to fatigue and that mechanical fatigue phenomena can occur in brittle solids[15] like silicon. That means, that not only dislocation movement, but other irreversible deformation processes can contribute to crack growth. In silicon it is not clear yet, if such kinematically irreversible deformation exists. *Brown et al.* postulated, that slow crack growth in silicon can occur due to the fatigue of the native oxide layer, which is formed immediately when silicon is exposed to oxygen[16]. In their experiments they could measure a dependency of the time necessary for the fracture of dynamically loaded silicon beams on the humidity of the ambient air. Whereas other groups couldn't show any slow crack growth in statically loaded silicon bulk samples, that were wetted with various liquids including distilled water[17]. They concluded that stress corrosion cracking does not occur due to the formation of the protective silica layer[18],[19], this silica layer has been postulated by *Brown et al.* for being the cause of corrosion

fatigue. Thus fatigue of silicon is still a subject of controversy, but if fatigue can occur it will be in the form of corrosion fatigue.

Figure 5.5: SEM micrograph of a precracked polysilicon membrane. Such test-structures are used to measure the crack-growth rate.

In our experiments we have stress cycled precracked modulator membranes at various levels of air humidity. The estimated stress in the crack region was 0.15 GPa. At a relative air humidity of up to 94 % no growth of the crack could be observed. All the same a colour change of the membrane appeared, which was attributed to corrosion.

5.3.4. Computation of Mechanical Reliability

In Table 5.4 the operation stresses and the material strengths are summarized. It can be seen, that for both the fiber optic switch and the reflective modulator the operation stresses are well below the strength limit of silicon. Only during the fabrication process of the reflective modulator the stress may become sufficiently high to break a few membranes. According to the Weibull statistics 0.05 % of the membranes would break during the final rinsing and drying processes.

In dry air long cycle fatigue due to slow crack growth could not be observed at the working stress levels. This may be explained by the convalent crystal structure of silicon in which dislocations are not mobile at room temperature. Fatigue is therefore not expected to occur, except in the form of corrosion fatigue.

Table 5.4: Comparison between mechanical stress and strength for the fiber optic switch and the reflective modualtor

	fiber optic switch	reflective modulator
stress in operation	60 MPa	130 MPa
stress in fabrication	60 MPa	1.5 GPa
rupture strength	3.5 Gpa	3.5 GPa
fatigue resistance	no fatigue in dry air	no fatigue in dry air
breakdown probability	0 %	0.05 %

5.4. Electrical Reliability

To activate the fiber optic switch voltages of typically 30 V are applied. For faster designs the driving voltage may be as high as 60 V. To prevent transverse instability and to relax the verticality requirements for the deep reactive ion etching the air-gap is never smaller than 3 µm. Thus the maximum electric field is smaller than 20 V/µm.

As for the mechanical stress the maximum electric field is much higher in the reflective modulator than in the fiber optic switch. To deform the polysilicon membrane of the reflective modulator voltages up to 90 V have to be applied. For a minimum air gap of 1.2 µm this conducts to a maximum electric field between the plates of electrodes of:

$$E = \frac{90V}{1.2\mu m} = 75\frac{MV}{m} = 75\frac{V}{\mu m} \qquad (5.13)$$

At the edge of the membrane a field concentration occurs. The sharper the edge, the higher the field. It is possible to estimate how much higher the field at the edge E_{edge} is than the homogenous field E: In case the electrode thickness is

larger than half of the air gap h, which is approximately the case for our modulator, then the field at the edge is [20]:

$$E_{edge} = \frac{E}{\sqrt[3]{\frac{3\pi\rho}{h}}} = f_{edge}E \qquad (5.14)$$

where ρ is the radius of the edge. In case of a very sharp edge with a radius of only 1 nm f_{edge}, the field concentration factor, is: f_{edge} = 5. In case of a edge radius of 10 nm f_{edge} is: f_{edge} = 2.4. Thus for a sharp edge with a radius between 1 nm and 10 nm the electric field at the edge is about 2.4 - 5 times larger than the homgenous field between the condensator electrodes.

5.4.1. Electrical Breakdown

If the voltage on the capacitor electrodes attains a certain critical value the insulation property of the filling medium is suddenly lost and an arc short circuits the electrodes. In an air-filled capacitor the Paschen-curve expresses the dependence of the static breakdown voltage as a function of air pressure and distance between the electrodes. According to the Paschen curve the breakdown field depends on the electrode separation. When this separation gets as low as the mean free path of the air molecules, the breakdown field increases. This is due to the fact, that ionised molecules are attracted and stopped on an electrode before they could ionise other molecules and trig an avalanche effect, manifesting itself as an electrical arc. At atmospheric pressure the Paschen curve has a minimum breakdown voltage at a separation of the capacitor plates of 10 µm. The minimium breakdown voltage for the 10 µm plate separation is 400 V. At a plate separation of only 1 µm the breakdown voltage is over 1 kV. But at field strength higher than 500 V/µm emission of field can occur. Electrons are extracted from the surface and a current can establish, this electrons extraction is dependent on the material[21]. In the Paschen-curve of Figure 5.6 the separating medium is air. Changing the filling gas displaces the Paschen-curve to higher or lower breakdown voltages. It is known, that filling the capacitors with electronegative gases like SF_6, or CCl_4 can double the breakdown voltage[21].

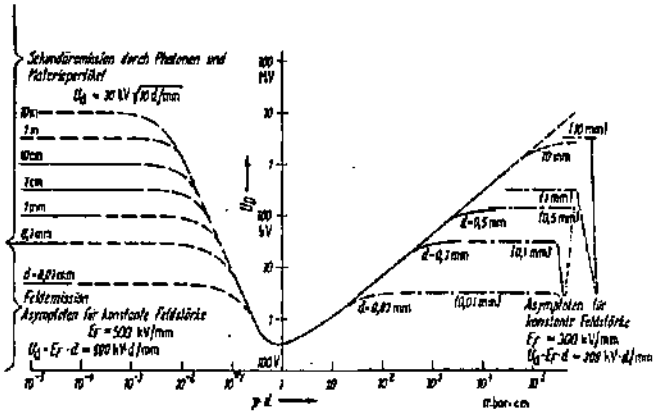

Figure 5.6: "Paschen-curve". Breakdown voltage in air in a homogenous field as a function of the product of air pressure *p* and distance between the electrodes *d*.

The reflective modulator works at a maximum operating voltage of 100 V, thus well below the minimum breakdown voltage of 400 V for an airgap of 10 µm. The emission of field should be of reduced importance as well, because the maximum field supposing a sharp edge of 0.05 µm (equation (5.14)) is below 200 V/µm, which is lower than the 500 V/µm limit.

In the fiber optic switch the electric field is even lower. Thus there is no a risk of electrical discharge neither. All the same it may be interesting to fill the actuator with an index matching oil. In liquids the mean free path is much shorter and there is no effect like the one expressed by the Paschen-curve, where the breakdown field increases for small gaps. In silicone oils the breakdown field is typically 20 - 30 V/µm, thus quite close to the operating fields. Here electrical discharge may play a role.

5.4.2. Permanent Polarisstion of the Capacitor

From a practical point of view there may always be some free charges and surface currents in air filled capacitors; these may accumulate on a non-conductor, as silicon dioxide or silicon nitride or on the native oxide of the silicon electrodes.

Figure 5.7 shows a cross section of a modelised representation of the accumulation of charges on the native oxide of polysilicon. To measure the potential effect of such an accumulation of charges, precise measurement of the resonance frequency can be used. Actually the resonance frequency is a function of the applied bias voltage, because the force exerted by the applied electric field lowers the equivalent spring constant of the resonator. The equivalent spring constant is the sum of the mechanical spring and the space-derivative of the electrostatic force.

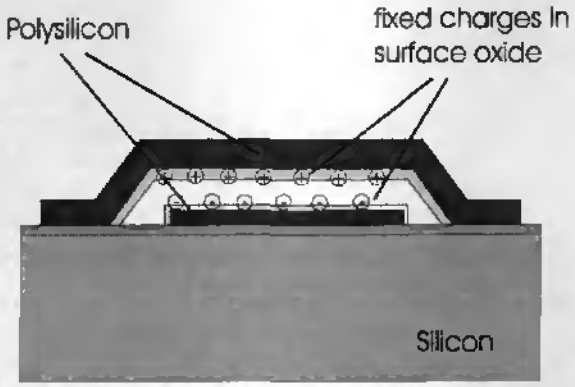

Figure 5.7: Model for permanent polarisation of electrostatic air gap capacitors.

Equation 5.15 gives an analytical expression of the resonance frequency supposing a parallel plate lumped model.

$$f_m = \frac{1}{2\pi}\sqrt{\frac{1}{m}\left(k - \frac{\varepsilon V^2}{(d-x)^3}\right)} \qquad (5.15)$$

,where m is the mass of the oscillator, k the mechanical spring constant of the membrane, ε is the electrical permittivity, V is the applied DC bias voltage, d is the initial airgap and x the membrane deformation under the DC bias voltage V.

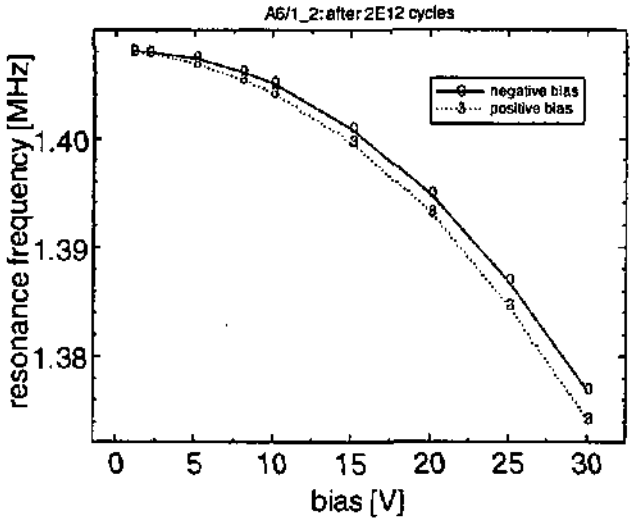

Figure 5.8: Dependency of resonance frequency on the applied bias voltage. The upper curve is for a positive biaa and the lower curve is for a negative bias voltage.

Figure 5.8 shows a measurement of the resonance frequency as a function of applied positive and negative bias voltage. The measurement is done in vacuum to get a high quality factor of the resonator and thus a precise measurement of the resonance frequency. After 8 days of continuous operation the difference between the resonance frequency at positive and negative bias voltage indicates a permanent polarisation not exceeding 0.3 V. For an operation voltage of 80 V this represents a drift of only 0.4 %.

5.4.3. Qualitative Electrical Reliability Assessment

In Table 5.5 the results of the above considerations and experiments are summarised. It can be seen, that for both the fiber optic switch and the reflective modulator the operation fields are well below the breakdown field of air filled capacitors. All the same if an oil filling is applied to the fiber optic switch electric arc discharge may become a problem.

Table 5.5: Comparison between electrical field in operation and field strength and polarisation resistance for the fiber optic switch and the reflective modulator

	fiber optic switch	reflective modulator
electric field in operation	20 V/µm	75 V/µm
breakdown field at min. gap	200 V/µm but 30 V/µm in oil	400 V/µm
permanent polarisation	not measured but expected < 1 %	< 0.5 %
breakdown probability	0 %	0 %

The measured drift of the actuation voltage, which is attributed to a permanent polarisation, was measured by a resonant frequency technique. It is not higher than 0.3 V. This presents less than 0.5% of the bias voltage needed for the device actuation. If the electrostatic actuator is operated in dry air the charge-up phenomenon isn't expected to be a problem either.

5.5. Corrosion

In this paragraph we investigate into the corrosion of electrostatic actuators, when they are operated in humid air. In this study we have concentrated on the modulator device, because the mechanical and also the electrical stress are much larger for the reflective modulator than for the fiber optic switch. In addition the resonance frequency is easier to measure for the surface normal operating modulator than for the switch. Measuring the resonance frequency with a high precision allows to detect even very small changes in the mechanical structure.

5.5.1. Drift of the Resonance Frequency

To characterise the mechanical long term behaviour the resonance frequency is measured in vacuum. A quality factor of about 6500 was obtained. After a first measurement of the resonance frequency the structures are stress cycled at atmospheric pressure under different humidity conditions.

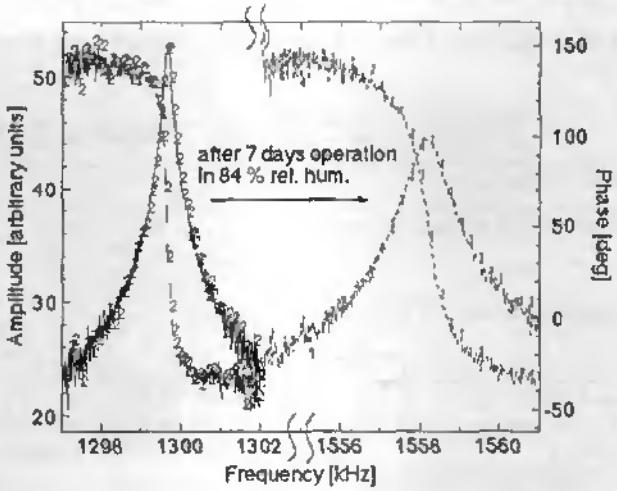

Figure 5.9: Operation in humid air can lead to an increase of the resonance frequency. Operation in dry air doesn't lead to any frequency shift. Note the discontinuous frequency scale.

After stress cycling in relative humidity of 84 % some test structures showed a distinct frequency increase of up to 20 % and a decrease of the quality factor as shown in Figure 5.9.

In addition colour changes of these structures could be observed as shown in Figure 5.10.

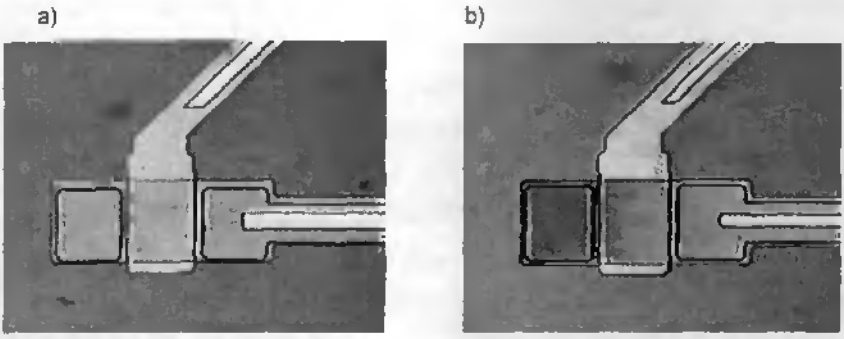

Figure 5.10: Color change after operation in humid air during 7 days at 84 % rel. hum. and 40 V DC. a) Before stress cycling. b) after stress cycling.

This noticeable change in the mechanical properties, which could lead to a failure of the modulator function, can be explained by the formation of a surface oxide under the high humidity and electric field conditions. Internal stress in the oxide stiffens the membrane and leads to the frequency increase. Corrosion resulting in a noticeable increase of the resonance frequency could be observed at an electric field higher than 10 V/μm and at an air humidity above 65 %.

5.5.2. Membrane Rupture and Polysilicon Delamination

If the stress cycling conditions, i.e. air humidity, electrical field and amplitude of mechanical stress cycles are sufficiently high, mechanical fatigue of the free standing membrane could be observed resulting in membrane rupture and delamination of the underlying fixed polysilicon electrode. Figure 5.11 shows a SEM micrograph of a broken membrane. The actuator specimen were not precracked; thus membrane rupture is not necessarily due to slow crack growth but might be due to the high internal stress in the corroded membrane.

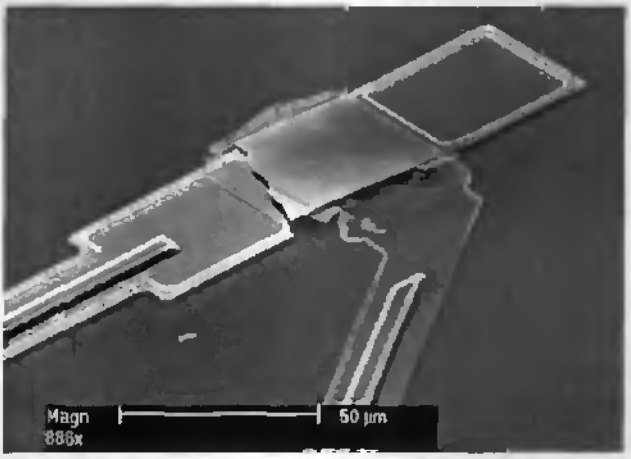

Figure 5.11: Membrane rupture after exposure to humid air and high electric field. It was observed that the cathode corrodes faster.

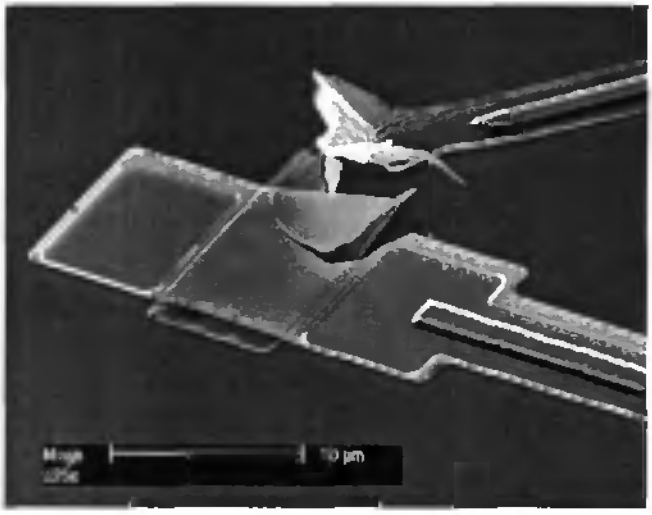

Figure 5.12: Not only rupture of the free standing membrane is observed, but the fixed polysilicon electrode can also show delamination.

To produce membrane rupture within one week's time a field over 50 V/μm, resulting in a maximum mechanical stress of about 100 MPa, and a relative air humidity above 80 % were necessary. A 30 V peak-to-peak AC square signal of 500 kHz was superimposed on a DC bias in order to produce cyclic mechanical loads. As shown in the SEM micrograph of Figure 5.12 not only rupture of the free standing membrane is observed, but the fixed polysilicon electrode can also delaminate during the stress cycling.

5.5.3. Permanent Electrical Polarization

The permanent electrical polarisation after stress cycling in humid air is measured according to the above procedure (equation 5.15). Figure 5.13 shows the resonance frequency as a function of the absolute value of DC bias before and after stress cycling in humid air. It can be seen, that a permanent polarisation of about 2 V is present after the cycling test, i.e. for a given resonance frequency the difference between positive and negative bias DC is 4V. This polarisation can be explained by trapped charges in the surface oxide.

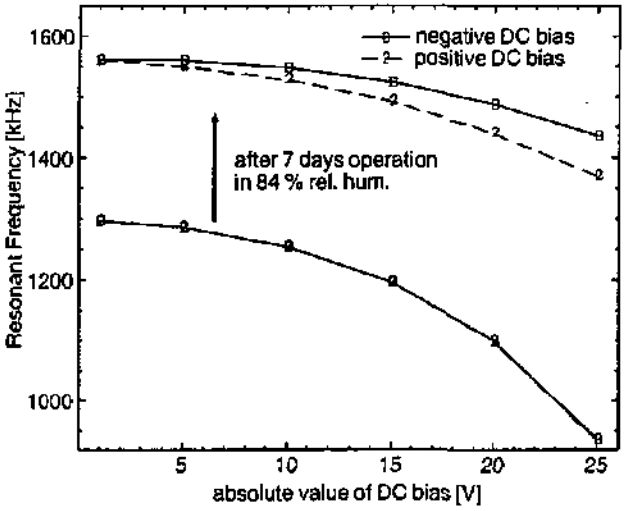

Figure 5.13: Resonance Frequency as a function of DC bias. After cycling the resonance frequency has increased 250 kHz and the capacitor has a built in voltage of 2 V.

5.5.4. Qualitative Evaluetion of the Resietance against Corrosion

The combined action of high electrical field, air humidity and mechanical stress can rapidly destroy the polysilicon micromechanisms. An important drift of the resonance frequency was observed. If the stress cycling test is continued this drift increased until rupture of the membrane occurs. In addition delamination of the fixed polysilicon electrode from the underlying nitride layer could be observed.

From an electrical point of view a permanent polarisation, that was much larger than the polarisation during the operation in dry air, could occasionally be observed.

These observations show, that electrostatic actuators can rapidly be destroyed if they are operated in an air humidity, which must be larger than 70 % relative humidity at ambient temperature. In a long term operation of electrostatic actuators high air humidity should be hindered from reaching the air gap capacitor.

5.6. In Use Stiction

In the fiber optic switch the maximum displacement of the mirror is limited by landing electrodes. These mechanical stoppers prevent a short circuit between the comb electrodes. But when two surfaces enter into mechanical contact they may get bonded to each other. They remain stuck; the spring force, which should pull back the moveable mechanical part is smaller than the adhesion force between the two contacted surfaces. The in-use stiction describes this phenomena when it occurs during operation, thus after a successful release in the fabrication process.

5.6.1.Restoring Spring Force

Single beams guided at both ends are the building base for the suspension springs. Their spring constant is[4]:

$$k_{single} = \frac{12EI}{l^3} = \frac{Eht^3}{l^3} \qquad (16)$$

where E denotes the Young modulus, I the moment of inertia of the beam cross section, h the beam height, t the beam thickness and l the beam length. To increase the transverse stiffness the springs are composed of double beams. To obtain linear springs at least two double beams are connected in series to form a spring meander. Finally the mirror-actuator structure is suspended at 4 points by meander structures composed of beam springs.

The restoring force is the product between the maximum mirror displacement Δx and the total spring constant. For the push-pull design the restoring force in its maximum position is 45 μN (for h=75 μm, t=2 μm, l=380 μm and Δx=12 μm). For the uni-directional design the restoring force in its maximum position is 110 μN (for h=75 μm, t=2 μm, l=450 μm and Δx=25 μm).

5.6.2. Surface Adhesion Force

It has been shown, that the dominant forces acting between surfaces at the microscale are capillary forces due to meniscus formation[22,23,24]. Capillary forces are thought to be present in silicon structures because silicon forms a hydrophilic native oxide in air, which leads to a high surface energy and a hydrophilic surface.

Consequently, this surface attracts water from the ambient air which allows meniscus formation to occur as surfaces come into contact. Additionally, when two surfaces are actually in contact bonding of the hydroxyl groups can take place; this behaviour is exploited in silicon fusion bonding[25]. In short range gaps van der Waals and electrostatic forces also become significant[26]. Capillary, electrostatic, van der Waals forces and covalent bonds may all contribute to the adhesion of the surfaces and to device failure.

Three techniques have been proposed for the reduction of the in-use stiction: surface roughening, surface passivation by coating and increasing the stored mechanical energy by flexible landing electrodes. The roughening method seeks to reduce the contact area by dimples[27],[28] or by an increased surface roughness[29],[30]. A reduction of the adhesion by a factor of 5 has been reported[29],[30] with the roughening technique. On the one hand the surface tension energy at the interface is reduced if the effective contact area is reduced. On the other hand the van der Waals force is very sensitive to the surface roughness. Denoting the surface roughness with r and the distance between the two surfaces with z, the van der Waals force of flat surfaces F_{vdw} is reduced by the roughening to a van der Waals force of[31]:

$$F^{*}_{vdw} \approx \left(\frac{z}{z+\frac{r}{2}}\right)^{2} F_{vdw} \qquad (5.17)$$

For a surface roughness of 50 nm and a contact gap of 0.5 nm the van der Waals force is reduced by a factor of over 2000.

The passivation approach seeks to reduce the surface energy with an appropriate surface coating[32],[33] which reduces the attractive forces between microstructure surfaces. A main function of such coatings is to provide a hydrophobic surface. This will impede the condensation of water on these surfaces, and therefore prevent meniscus formation and the resulting capillary forces. One technique for applying surface passivation coatings is based on self-assembled monolayers (SAMs). Such coatings are frequently used for priming purposes, i.e. to enhance the adhesion of photoresists or glues. These coatings can also be used as lubricant layers[34],[35] and as in our case for an efficient anti-stiction layer. It could be shown, that SAM

coatings can reduce the in-use stiction by several orders of magnitude[32]. The coating can be deposited in gas phase or in a sequence of liquid soaks.

The two first methods tried to reduce the contact forces at the interface, whereas the third method seeks to increase the restoring force. The sticking probability can be reduced by increasing the restoring spring force. The simplest way would be to increase the stiffness of the suspension springs, though with the draw back of an increased driving voltage. To keep the driving voltage low it has been proposed to integrate a spring function in the landing electrodes in order to store a part of the impact energy in these landing springs[36].

To determine the adhesion force at the landing electrode of the deep plasma etched actuators special test structures have been designed. We used 500 µm long and 3 µm thick beams which can be pulled with electrostatic actuation against a stopper electrode. Figure 5.14 shows a top view of the test beams in released and actuated position.

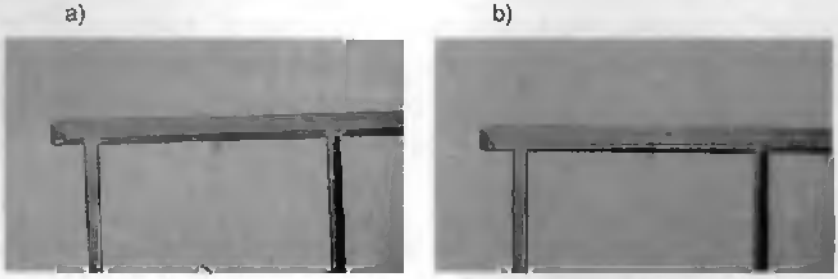

Figure 5.14: Beam for measuring the adhesion force of the contact surface. a) released position. b) Actuated position of the beam.

By increasing the voltage between the beam and the counter electrode the beam is more and more deformed under the electrostatic field. When a certain pull in voltage is reached the beam snaps in and is stopped by the landing electrode, which is at the same potential as the beam. To release the beam from its actuated position the voltage has to be reduced below a certain pull out voltage.

If we admit, that the air humidity is the main factor which affects the adhesion force, it is now possible to measure the change of the adhesion force between the beam

and the landing electrode by recording this pull out voltage for different environments. We made a first measurement of the pull-out voltage in a dry nitrogen atmosphere, i.e. in absence of air humidity. In a second measurement humid air is introduced into the measurement chamber. And after stabilisation of the humidity the pull-out voltage is measured again. In 83 % of the 8 measured structures the voltage for release of the beams in humid air was smaller than the pull out voltage in dry air. It means, that in high air humidity an increase of the adhesion force could be measured. The shift between the pull out voltage in dry and humid air was between 0.2 and 1.2 V for an average pull out voltage of 24.5 V. In average the increase of the air humidity from 0% to 100% resulted in a shift of the pull-out voltage of 0.56 V. With a numerical simulation of the beam deflection under the electrostatic actuation it is possible to calculate the adhesion-force, which corresponds to that pull-out voltage shift[37]. If we assume parallel plate electrodes, a simple analytical expression can be found for the adhesion force increase $\Delta F_{adhesion}$ in humid air:

$$\Delta F_{adhesion} = \left(\frac{1}{2}\frac{\varepsilon w h}{d^2}\right)\left(V^2_{po\_dryair} - V^2_{po\_humidair}\right) \qquad (5.18)$$

where ε is the permittivity of air, w = 210 µm and h = 75 µm are the width and height of the capacitor electrode, d = 2.5 µm is the mean air gap between the electrode and the beam after pull in and V_{po_dryair} = 24.5 V is the pull out voltage in dry air, whereas as $V_{po\_humidair}$ = 23.9 V is the pull out voltage in humid air. Introducing the geometrical dimensions and the average pull out voltages of our 8 measurements we obtain an adhesion force increase of 0.3 µN due to the air humidity. Thus the air humidity introduces an additional adhesion of 0.3 µN. If we suppose this force proportional to the contact surface of 2 µm x 75 µm, we obtain an adhesion strength of 2 kPa. This value has to be compared with bonding strength of a low temperature silicon fusion bond[38],[39] which can easily be over 10 MPa thus more than 5000 times higher than our measurement. This difference is explained by the fact, that the actuator surfaces present a surface roughness much higher than that of polished wafers. In addition in the wafer bonding process the surfaces are specially pre-treated and annealed at a

temperature above 120 °C[40]. All the same we can assume an adhesion strength of 10 MPa as an upper limit. This would yield a adhesion force of 1500 µN per stopper.

5.6.3. Ratio between Restoring and Adhesion Force

In the push-pull design there are two stopping electrodes, thus the typical adhesion force is 0.6 µN. The restoring springs generate a force of over 40 µN, which is over 50 times higher than the adhesion. In the uni-directional design there are 6 stoppers, which can generate an adhesion force of 1.8 µN. The force of the springs is 110 µN, which is also over 50 times higher than the adhesion. Thus the experimental adhesion forces are much lower than the restoring spring force. Nevertheless if we admit an adhesion as high as the silicon fusion bonding strength the springs aren't sufficient anymore to pull back the actuator from the extreme position. Stoppers that would create a fusion bond could generate forces as high as 1500 µN per stopper. Above results are summarised in Table 5.6.

Table 5.6: Measured and theoretical adhesion force compared to the restoring spring force.

	push-pull	uni-directional
measured adhesion force	0.6 µN	1.8 µN
theoretic fusion bond force	3000 µN	9000 µN
restoring spring force	45 µN	110 µN
breakdown probability	0 %	0 %

5.7. Conclusions

In absence of high air humidity the mechanical properties of silicon respectively polysilicon meet the requirements for highly reliable electrostatic actuators, i.e. the fracture strength is well above the operation stress and slow crack growth could not be observed for both the fiber optic switch and the reflective modulator. Due to the absence of dislocation movement slow crack growth is expected to occur only as corrosion fatigue. In dry air no change of the mechanical nor the electrical properties could be observed.

The combination of high electric field with humid air can lead to mechanical breakdown, i.e. membrane rupture. Membrane rupture is preceded by a noticeable increase of the resonance frequency and a permanent electrical polarisation of the air gap capacitor. This is explained by the formation of a surface oxide. In a long term operation of electrostatic actuators, high air humidity should be hindered from reaching the air gap capacitor.

In the fiber optic switch the maximum mirror displacement is limited by landing electrodes. Mechanical contacts are known to stay sticked. To evaluate this sticking probability we have measured the difference in adhesion in dry and humid air between two contacting surfaces. It was found that the measured increase in adhesion in humid air is more than 50 time smaller than the restoring spring force.

[1] S B Brown, G Povirk, J Connally, "Measurment of Slow Crack Growth In Silicon and Nickel Micromechanical Devices", *Proceedings of the IEEE Micro-Electro-Mechanical-Systems Workshop*, ,1993

[2] M R Houston, R Maboudian, R T Howe, "Ammonium Fluoride Anti-Stiction Surface Treatments for Polysilicon Microstructures", *Proceedings of International conference on Solid-State Sensors and Actuators, Transducers '95*, June 25 - 29, 1995, Stockholm, Sweden

[3] A. Birolini. *Quality and Reliability of Technical Systems*. Springer Verlag 1994. Chapter 2-4

[4] W. C. Young. *Roark's Formulas for Stress and Strain*, New York: McGraw-Hill, sixth edition 1989, p. 101

[5] G. Michot, A. George. "Fracture and Crack Tip Plasticity in Silicon and Gallium Arsenide". *Proceedings of the Sixth Int. Symp. on Structure and Properties of Dislocations in Semiconductors*, 1989, Oxford, pp. 385 - 396.

[6] P.B. Hirsch, S.G. Roberts, J. Samuels and P.D. Warren. "Dislocation Dynamics and the Brittle-Ductile Transition in Precracked Silicon". *Proceedings of the Sixth Int. Symp. on Structure and Properties of Dislocations in Semiconductors*, 1989, Oxford, pp. 373 - 384.

[7] D. J. Green. "Fracture Mechanics". in *Introduction to mechanical behaviour of ceramics*. Goffredo de Portu (Editor). CNR IRTEC. 1992. pp. 53 - 67

[8] H. Tada, P. C. Paris and G. R. Irwin, *The Stress Analysis of Cracks Handbook*. Del Research Corporation, 1973.

[9] V.P. Jaecklin, C. Linder, J. Brugger, N.F. de Rooij, J.-M. Moret, R. Vuilleumier. "Mechanical and Optical Properties of Surface Micromachined Torsional Mirrors in Silicon, Polysilicon and Aluminium". *Sensors and Actuators A*, 43, pp. 269-275, 1994

[10] Y. C. Tai and R. S Muller, "Fracture Strain of LPCVD Polysilicon", *In Tech. Dig. IEEE Solold-State Sensor and Actuator Workshop*, 1988, pp. 88-91

[11] V. P. Jaecklin, *Surface Micromachined Electrostatic Actuators*, PhD Thesis, University of Neuchâtel, 1994, pp. 109 - 113

[12] J.E Ritter. "Stength and Reliability of Ceramics". in *Introduction to mechanical behaviour of ceramics*. Ed: Goffredo de Portu. CNR IRTEC. 1992. pp. 105 - 121.

[13] B. Bertsche, G. Lechner, *Zuverlässigkeit im Maschinenbau*, Berlin: Springer Verlag 1990, p.63

[14] P. Krulevitch, G.C. Johnson and R.T. Howe, "Stress and Microstructure in Phosphorus Doped Polycrystalline Silicon", *Mat. Res. Soc. Symp. Proc.*, Vol 276, 1992.

[15] S. Suresh. *Fatigue of Materials*. Cambridge University Press. 1991, p 403,

[16] S. B. Brown, G. Povirk and J. Connally. "Measurement of slow crack growth in silicon and nickel micromechanical devices". *In Proceedings of the IEEE/ASME Workshop on Micro-Electro-Mechanical Systems*, IEEE, Ft. Lauderdale, 1993

[17] T.J. Chen, and W.J. Knapp, "The Fracture of Single Crystal Silicon Wafers under Several Liquid Environments", *Journal of the American Ceramic Society - Discussion and notes*, March-April 1980.

[18] B. Wong, , and R.J. Holbrook, "Microindentation for fracture and stress corrosion cracking in single crystal silicon" *Journal of the Electrochemical Society*, September, 1987

[19] C.P. Chen, and M.H. Leipold, "Crack growth in Single crystal silicon" *NASA Tech Brief*, Vol. 10, No. 3, Item No. 106, May/June 1986.

[20] Zinke, Seitner. *Widerstände, Kondensatoren, Spulen und ihre Werkstoffe*, Berlin: Springer Verlag 1992. p. 117

[21] Zinke, Seither. *Wioerstände, Kondensatoren, Spulen und ihre Werkstoffe*, Berlin: Springer Verlag 1992. p. 150

[22] R. L Alley, P. Mai, K. Komvopoulos and R. T. Howe, "Surface roughness modification of interfacial contacts in polysilicon microstructures", *Proc. of the 7th International Conferance on Solid-State Sensors and Actuators Transducers '93*, Yokohama, Japan, Jun. 1993, p. 288

[23] R. Legtenberg, H. A. C. Tilmans, J. Elders and M. Elwenspoek, *Sensors and Actuators A*, A 43, 230 (1994)

[24] C. H. Mastranggelo and C. H. Hsu, "Mechanical stability and adhesion of microstructures under capillary forces - part I", *J. Microelectromechanical Systems, vol. 2*, No. 1, pp. 33 - 43, Mar. 1993

[25] C. Harendt, B. Hofflinger, H. Graf, E. Penteker, "Silicon direct bonding for sensor applications: characterisation of the bond quality", *Sensors and Actuators A*, vol. A25-27 (1991), pp. 87-92

[26] R. L. Alley, R. T. Howe, and K. Komvopoulos, *Proc. IEEE Solid-State Sensor and Actuator Workshop*, Hilton Head, SC, USA, June 1992, p. 202

[27] T. Abe, W. C. Messner and M. L. Reed, "Effective metnods to prevent stiction during post release etch processing", *Proc. IEEE Micro Electro Mechanical Systems*, Amsterdam, NL, Jan. 1995, pp.94 - 95

[28] W. C. Tang, T.C.H. Nguyen, and R. T. Howe, *Proc. IEEE MEMS Workshop*, Salt Lake City, UT, USA, Feb. 20-22, 1989, p. 53

[29] Y. Yee, K. Chun, J. D. Lee, "Polysilicon Surface Modification Technique fo reduce Sticking of Microstructures", *Proc. of the 8th International Conference on Solid-State Sensors and Actuators and Eurosensors IX (Transducers '95)*, Stockholm, June 25 - 29, 1995, p.206-209

[30] R. L Alley, P. Mai, K. Komvopoulos and R. T. Howe, "Surface roughness modification of interfacial contacts in polysilicon microstructures", *Proc. of the 7th International Conference on Solid-State Sensors and Actuators Transducers '93*, Yokohama, Japan, Jun. 1993, p. 288

[31] F. Arai, D. Andou, T. Fukuda, "Adhesion Force Reduction for Micro Manipulation Based on Micro Physics", *Proc. IEEE Micro Electro Mechanical Systems*, Amsterdem, NL, Jan. 1995, pp. 354-359

[32] M. R. Houston, R. Maboudian and R. T. Howe, "Self-Assembled Monolayer Films as Durable Anti-Stiction Coatings for Polysilicon Microstructures", *Solid-State Sensor and Actuator Workshop*, Hilton Head SC, June 2-6, 1996, pp. 42-47

[33] P. F. Man, B. P. Gogoi and C. H. Mastrangelo, "Elimination of Post-Release Adhesion in Microstructures using Thin Conformal Fluorocarbon Films", *Proc. Of 9th IEEE Workshop on Micro Electro Mechanical Systems*, San Diego, CA, Jan. 1996, pp. 55-60

[34] K. Deng, R. J. Collins, M. Mehregany andC. N. Sukenik, "Performance Impact of Monolayer Coating of Polysilicon Micromotors", *Proc. IEEE Micro Electro Mechanical Systems*, Amsterdam, NL, Jan. 1995, pp. 368-373

[35] H. Camon, V. Conedera, N. Fabre, J. M. Chovelon, C. Martelet and M. Belin, "Non Sticking layer for silicon micromotors", *Proceedings of Micro-Mechanics Europe (MME '96)*, oct. 1996, Barcelona, Spain, pp. 105-108

[36] M. R. Douglass and D. M. Kozuch, "DMD Reliability Assessment for Large-Area Displays", *Society for Information Display International Symposium Digest of Technical Papers*, Vol. 26 (Applications Session A3, pp. 49-52, (May 23-25, 1995)

[37] O. Dumont, "Breakdown Mechanisms of Polysilicon Microactuators", *Semester Work winter 96/97*, Institute of Microtechnology, University of Neuchatel, 1997

[38] B. Mueller, A. Stoffel, "Tensile strength characterisation of low-temperature fusion bonded silicon wafers", *J. Micromech. Microeng.*, 1 1991, pp. 161-166

[39] J. Jiao, D. Lu, B. Xiong, W. Wang, "Low temperature SDB and interface behaviours", *Sensors and Actuators A*, A 50 (1995), 117-120

[40] A. Berthold, P. M. Sarro, P. J. French, M. J. Vellekoop, "IC-Compatible Silicon Fusion Bonding", *Proceedings of Eurosensors X*, Leuven, Belgium, 8-11 September 1996, pp. 489-492

Chapter Six

Final Conclusions

In the present thesis we have investigated into applications of silicon micromechanics for fiber optic communication. Using the microfabrication technologies mechanical systems can be miniaturised to such an extent, that dynamic mechanical devices get a sufficient performance for applications that were dominated by electronics and opto-electronics. Conventional opto-mechanics have a long tradition and offer intrinsic advantages with respect to electro-optical components; in particular polarisation and wavelength insensitivity and a high optical insulation. Nevertheless to be used with fibers conventional mechanics are too bulky and slow. The miniaturisation achieved in micromechanics leads to several improvements. First the high precision needed for fiber optics is readily obtained by the photolithographic fabrication. Second the operation speed of mechanical systems can be increased several orders of magnitude. Finally the fabrication technology is destined for producing large quantities. The telecommunication sector is expected to need large quantities, when the fiber network continues its deployment until the individual household. If micromechanical devices are fabricated at high volume, the cost per device becomes very low. With micromechanics it seems thus possible to combine the performance of conventional high precision opto-mechanics with the advantages of silicon wafer processing.

A first field of interest were passive mechanical structures without moving parts: structures for the passive alignment of fibers with optical components. For the

surface normal alignment we have shown, that a wet anisotropic hole etched in the backside of the wafer allows for an alignment within +/- 5 µm. A tighter tolerance can be achieved by circular holes plasma etched from the top side. For the *surface parallel* alignment usually wet etched V-grooves are used. However these grooves have to be aligned with particular crystal directions, which reduces the geometrical freedom. For more flexibility and a higher precision we have developed a new type of plasma etched grooves. These can be oriented in any direction. Processing variations are cancelled out by integrated clamping springs. Therefore the groove itself doesn't introduce an alignment error and the alignment can be as precise as the fiber dimensions. Self aligned assembly of optical fibers is an essential condition for a large scale production of fiber optic components. The importance of silicon motherboards for hybrid assemblies with photodiodes and laserdiodes will increase in the future. With the extension of single fiber systems to parallel multifiber arrays the passive alignment becomes already essential at the prototype level and is only feasible using microfabrication technologies. Here the high precision silicon micromachining will find many applications.

The second field of interest of the thesis were *reflective modulators* for data communication. Using reflective modulation data communication can be achieved with a minimum of optical components: only one fiber and one light source are necessary for bi-directional communication. The reflective modulator replaces the usual light source at the subscriber terminal and uses part of the incident light to send back information. Based on the well established polysilicon surface micromachining technology we have successfully developed a micromechanical reflective modulator for the 1.3 µm wavelength range. A typical modulation contrast of 10 dB with a maximum modulation rate up to 3 Mbit/s has been achieved. The operation principle is based on interference effects at two polysilicon mirrors and presents the advantage of inherent polarisation insensitivity. By electrostatic actuation the gap between the mirrors can be changed which results in modulation of the reflectivity. For the operation of a 3 Mbit/s device over the wavelength range between 1250 nm to 1350 nm, typical bias voltages between 65 - 95 V are applied; superimposed is a modulation voltage between ±5 V and ±12 V. The voltages depend on the operation wavelength and on the layer thickness precision of the

micromechanical structure. For the downstream data detection and for locking the modulator on the incident wavelength by a feed back control loop, a photodiode is mounted on the silicon chip. Together with the self aligned assembling of a single mode fiber, such a module results in a compact receiver-transmitter microsystem with the potential of very low cost. It is therefore very attractive to be produced in large volumes for applications in Fiber-to-the-Home systems. Another application of reflective modulation are low power applications. For modulation less power is consumed than for generation of light.

The second component developed in this thesis work is a *fiber optic switch* allowing to switch light between two pairs of fibers. The component is intended for by-passing network nodes of high speed data networks to increase their reliability. Critical requirements for the switch are a low insertion loss below 1 dB and a low switching time below 1 ms. Based on the new possibilities of deep reactive ion etching of silicon we have developed a switch that is based on the linear displacement of a vertical mirror. For the fabrication of the silicon motherboard including the actuator structure, the switching mirror and the fiber alignment grooves only one photolithography is necessary. With such a short process prototyping cycles can be kept very short and the product development can be done in a much shorter time than for conventional bulk or surface micromachined structures. The performance of first, fully packaged switches is already very promising: the insertion loss can be reduced below 1 dB in the bar state and below 2 dB in the cross state. The use of micromechanics allows for a considerable increase in the switching speed. The total switching time is a factor of 50 shorter than for conventional mechanical switches and even somewhat faster than for thermo-optic switches. Future developments will aim a further reduction of the light loss and an improvement of the packaging scheme.

The above developments can only be introduced into the market if they are reliable. Micromechanics is still a risky topic and many people are sceptic about their commercial success. To gain this lacking confidence a high reliability is essential. Therefore the last chapter of this thesis was devoted to the *reliability analysis* of the reflective modulator and the fiber switch. Instead of performing long term tests we have investigated into particular failure mechanisms of micromechanics. We determined the material limits under mechanical stress, under electrical field, in a

corrosive environment and finally the adhesion between contacting surfaces. To assess the reliability the material limits are compared with the stress during the operation. It has been shown, that the electrostatic micro-actuators are reliable as long as they are operated in dry air. But the combination of high electric field with humid air can lead to mechanical breakdown, i.e. rupture of the suspension spring. In a long term operation of electrostatic actuators high air humidity should be hindered from reaching the air gap capacitor.

Having developed a MEMS device with high performance and good reliability doesn't mean, that such a device has already all the chances to be industrialised. Besides commercial considerations, another aspect related to MEMS is of particular importance: To be able to produce MEMS devices with good, reproducible quality, the application specific fabrication has either to be very simple or several hundred wafers should be processed every year in the wafer foundry. Large numbers of wafers translate into hundred or thousand times more chips. Especially in the starting phase such high quantities can't be sold. In addition in this early phase of industrialisation development costs can become very high. The risks also are very high in the beginning. Therefore the financial charge should be kept small. One approach is the fabrication of microsensors and actuators with standard CMOS technology and using some postprocessing of the mechanical devices. Multiproject wafer services can be used to divide the financial investment on several customers. But based on standard CMOS the technological possibilities are limited. For the applicetion specific processes such as those developed in this thesis other solutions have to be found. The solution, we have chosen, is to run a prototype production in the fabrication facility of the IMT; for higher volumes the production can be transferred to a wafer foundry specialized in MEMS such as the *Swiss Center for Electronics and Microtechnology (CSEM) Inc.* This flexibility will allow to shorten the time form prototype to product and it permits to keep development costs reasonable.

Acknowledgements

All through the research for the present thesis I was able to count on the generous support of my superiors and colleagues. It is my particular desire to express my gratitude to:

Professor Dr. Nico F. de Rooij for giving me the opportunity to work in his group and to write this thesis, for his generous and enthusiastic support and guidance and for encouraging and enabling me to present the work at any places.

Dr. Paul Vogel of Ascom Tech Inc., Bern, who initiated our collaboration and has supported it very actively especially through the difficult phases.

Marc-Alexis Grétillat, who got me started on the work at IMT. From the beginning he has shared his experience and has contributed with many ideas on the work. His knowledgeable support and advice I acknowledge highly.

Olivier Anthamatten and Dr. Rainer Bättig of Ascom Tech Inc., Bern, for their collaboration. Their ideas were the starting point for the developments in this thesis. All the optical measurements and characterisations were performed in their laboratory, where we have spent some very intense moments. Particularly I remember my stay with Dr. Bättig in Hannover for a rather cold exhibition, that became very supportable with his humour.

Dr. Bernd Valk of Ascom Tech Inc., Bern, for his valuable advice and inspiring discussions.

Dr. Peter van der Waal for his scientific and non-scientific advice and help.

Pierre André Clerc, Sylvain Jeanneret and Sabina Jenny for their excellent technical support in the fabrication of the structures.

Sylviane Pochon for the wire bondings. Daniel Link for the metallisation on vertical mirrors. Dr. Lionel Paratte for many inspiring discussions on the bright future of electrostatics. Pierre François Indermühle for his introduction on FEM modelling with Ansys. Dr. Terunobu Akiyama for the AFM imaging.

all present and past colleagues of the IMT for creating a stimulating research environment.

Professor Dr. Marc Ilegems, Dr. Hans-Peter Herzig, Dr. Peter Vettiger and Dr. Paul Vogel for kindly agreeing to co-examine this thesis.

Birgit Schreier, of course, for her love, friendship and her prayers.

This work was founded by Ascom Tech Inc., Bern, the Swiss Foundation for Research in Microtechnology (FSRM) and the Swiss Priority Programm MINAST.

AVE MARIA, DEO GRATIAS.

Bibliography

Parts of the work presented in this thesis have contributed to the following publications:

Refereed articles:

C. Marxer, M.-A. Gretillat, V.P. Jaecklin, R- Baettig, O. Anthamatten, P. Vogel and N. F. de Rooij, "Megahertz Opto-Mechanical Modulator", *Sensors and Actuators A 52* (1996) pp. 46-50

C. Marxer, M.-A. Gretillat, R. Baettig, O. Anthamatten, B. Valk, P. Vogel and N. F. de Rooij, "Reliability Considerations for Electrostatic Polysilicon Actuators using as an Example the REMO-Component", *Sensors and Actuators A 61 (1997) pp. 449-454*

C. Marxer, C. Thio, M.-A. Gretillat, O. Anthamatten, R. Baettig, B. Valk, P. Vogel and N. F. de Rooij, "Vertical Mirrors Fabricated By Deep Reactive Ion Etching For Fiber Optic Switching Applications", *IEEE J. of Micro Electro Mechanical Systems*, vol. 6, no. 3, September 1997, pp. 277 - 285

Conference Proceedings:

C. Marxer, M.A. Gretillat, V.P. Jaecklin, R. Baettig, O. Anthamatten, P. Vogel and N. F. de Rooij, "MHz Opto-Mechanical Modulator", *Tech. Dig. 8th International Conference on Solid-State Sensors and Actuators (Transducers '95)*, Stockholm, Sweden, june 1995, vol. 1 pp. 289 - 292

R. K. Bättig, O. Anthamatten, J.-Ch. Roulet, M. Fitzpatrick, B. Valk, P. Vogel, C. Marxer, M.-A. Gretillat, N. F. de Rooij, "Design Considerations and Optical Characterization of a Silicon-Micromechanical Light Modulator for Telecommunication Applications", *Proceedings of the Topical Meeting of the European Optical Society (EOS)*, Engelberg, Switzerland April, 1996, pp. 40-41

R. Baettig, O. Anthamatten, B. Valk, C. Marxer, M.-A. Gretillat, N. F. de Rooij, "A reflective Modulator based on Silicon Micromechanics", *Proceedings of the IEE*

Colloquium on Optical and Hybrid access networks, BT Laboratories, Ipswich, Digest No: 1996/052, March 1996, pp.10/1-10/4

O. Anthamatten, R. Bättig, B. Valk, C. Marxer, M.-A. Gretillat, N. F. de Rooij, "Telecommunications technology for telemetry", *Proceedings of the Opto '96 Congress*, Leipzig, Germany, September 1996, pp. 331-336

C. Marxer, M.A. Gretillat, and N. F. de Rooij, "Breakdown Mechanisms of Electrostatic Polysilicon Actuators using as an Exemple the REMO Component", *Digest of IEEE/LEOS 1996 Summer Topical Meeting, Optical MEMS and their Applications*, Keystone Co, USA, August 1996, pp. 15-16

O. Anthamatten, R. Bättig, B. Valk, P. Vogel, C. Marxer, M. A. Gretillat, N. F. de Rooij, "Packaging of a Reflective Optical Duplexer Based on Silicon Micromechanics", *Digest of IEEE/LEOS 1996 Summer Topical Meeting, Optical MEMS and their Applications*, Keystone Co, USA, August 1996, pp. 61-62

Y.-A. Peter, H.-P. Herzig, E. Rochat, R. Dändliker, C. Marxer, N. F. de Rooij, "Q-switched fiber laser using a torsional micro-mirror", *Digest of IEEE/LEOS 1996 Summer Topical Meeting*, Optical MEMS and their Applications, Keystone Co, USA, August 1996, pp. 67-68

C. Marxer, M.-A. Gretillat, R. Baettig, O. Anthamatten, B. Valk, P. Vogel and N. F. de Rooij, "Reliability Considerations for Electrostatic Polysilicon Actuators using as an Example the REMO-Component", *Proceedings of Eurosensors X, The 10th European Conference on Solid-State Transducers*, September 1996, Leuven, Belgium, pp.1117-1121

C. Marxer, M.A Grétillat, O. Anthamatten, R. Baettig, B. Valk, P. Vogel and N. F. de Rooij, "Vertical Mirrors Fabricated By Reactive Ion Etching For Fiber Optical Switching Applications", *IEEE International Workshop on Micro Electro Mechanical Systems*, 26 - 30 january 1997, Nagoya, Japan, pp. 49-56

Patent:

O. Anthamatten, C. Marxer, *"Überbrückungsschalter für faser-optische Netzwerke"* Internationale Patentanmeldung.

Biography

Cornel R. Marxer was born on October 7, 1969, in Grabs, Switzerland. He received his M. Sc. Degree in Microtechnology in 1994 from the Swiss Federal Institute of Technology in Lausanne, Switzerland. During his studies he spent two semesters at the *Ecole Polytechnique in Montreal, Canada. His masters thesis dealt with the* simulation and characterisation of micromirrors for a lithographic printing application. In spring 1994 he joined the group of Prof. N. F. de Rooij at the IMT of the University of Neuchâtel as a research and teaching assistant. He worked there in the field of differential pressure sensors and of fiber optical applications of micromachining. Results of these works are two fiber optic components, one for the modulation and one for the switching of light. The development of these devices is well advanced to a prototype level.